



CIVIL ENGINEERING STUDIES

Illinois Center for Transportation Series No. 23-006

UILU-ENG-2023-2006

ISSN: 0197-9191

Optimized Hot-Mix Asphalt Lift Configuration for Performance

Prepared By

Imad L. Al-Qadi

Aravind Ramakrishnan

Zehui Zhu

Izak Said

Greg Renshaw

University of Illinois Urbana-Champaign

Hasan Ozer

Ramadan Salim

Arizona State University

Research Report No. FHWA-ICT-23-005

A report of the findings of

ICT PROJECT R27-204

Optimized Hot-Mix Asphalt Lift Configuration for Performance

<https://doi.org/10.36501/0197-9191/23-006>

Illinois Center for Transportation

May 2023

TECHNICAL REPORT DOCUMENTATION PAGE

1. Report No. FHWA-ICT-23-005		2. Government Accession No. N/A		3. Recipient's Catalog No. N/A	
4. Title and Subtitle Optimized Hot-Mix Asphalt Lift Configuration for Performance				5. Report Date May 2023	
				6. Performing Organization Code N/A	
7. Authors Imad L. Al-Qadi (https://orcid.org/0000-0002-5824-103X), Aravind Ramakrishnan (https://orcid.org/0000-0003-3269-015X), Zehui Zhu (https://orcid.org/0000-0003-3965-4979), Izak Said (https://orcid.org/0000-0002-1796-0337), Greg Renshaw, Hasan Ozer (https://orcid.org/0000-0003-1526-6840), Ramadan Salim				8. Performing Organization Report No. ICT-23-006 UILU-2023-2006	
9. Performing Organization Name and Address Illinois Center for Transportation Department of Civil and Environmental Engineering University of Illinois at Urbana-Champaign 205 North Mathews Avenue, MC-250 Urbana, IL 61801				10. Work Unit No. N/A	
				11. Contract or Grant No. R27-204	
12. Sponsoring Agency Name and Address Illinois Department of Transportation (SPR) Bureau of Research 126 East Ash Street Springfield, IL 62704				13. Type of Report and Period Covered Final Report 8/16/19–5/31/23	
				14. Sponsoring Agency Code	
15. Supplementary Notes Conducted in cooperation with the U.S. Department of Transportation, Federal Highway Administration. https://doi.org/10.36501/0197-9191/23-006					
16. Abstract Researchers conducted eight large-scale laboratory tests to assess the combined impact of hot-mix asphalt (HMA) overlay mix and thickness on its performance to control reflective cracking. Bonding efficiency, flexibility, and stiffness of the HMA mix as well as overlay thickness significantly affect an overlay's performance against reflective cracking. Researchers developed a generalized 3D finite-element model to predict an overlay's reflective cracking potential and generated a database of 128 cases. They also developed a data-driven surrogate model to predict reflective cracking potential that engineers can easily use. Life-cycle cost analysis of overlay alternatives was performed using Illinois Department of Transportation's unit prices from contracts between 2018 and 2019. The researchers identified optimal overlay configurations to control reflective cracking. An overlay composed of a 1.5 in (38.1 mm) SMA-9.5 or 1.25 in (31.8 mm) IL-9.5FG surface course and a 0.75 in (19.1 mm) IL-4.75 binder course had the lowest annual cost per mile among non-interstate projects. For interstate projects, an overlay composed of a 2 in (50.8 mm) SMA-12.5 surface course and a 2.25 in (57.2 mm) IL-19.0 binder course was the most cost-effective. The study concluded that to control reflective cracking and to reduce life-cycle cost, an overlay composed of an SMA-9.5 surface course and an IL-4.75 binder course is recommended for non-interstate projects. An IL-9.5FG surface course and an IL-4.75 binder course are suggested for low-volume and low-speed roads. For interstate projects, an overlay comprised of an SMA-12.5 surface course and an IL-19.0 binder course is recommended. A data-driven surrogate model may be used to design overlay thicknesses.					
17. Key Words Asphalt Overlay, Reflective Cracking, Large-Scale Testing, Finite Element, Life-Cycle Cost Analysis			18. Distribution Statement No restrictions. This document is available through the National Technical Information Service, Springfield, VA 22161.		
19. Security Classif. (of this report) Unclassified		20. Security Classif. (of this page) Unclassified		21. No. of Pages 90 + appendices	22. Price N/A

ACKNOWLEDGMENT, DISCLAIMER, MANUFACTURERS' NAMES

This publication is based on the results of **ICT-R27-204: Optimized Hot-Mix Asphalt (HMA) Lift Configuration for Performance**. ICT-R27-204 was conducted in cooperation with the Illinois Center for Transportation; the Illinois Department of Transportation; and the U.S. Department of Transportation, Federal Highway Administration.

Members of the Technical Review Panel (TRP) were the following:

- John Senger, TRP Chair, Illinois Department of Transportation
- Laura Heckel, TRP Co-Chair, Illinois Department of Transportation
- William Warfel, Illinois Department of Transportation
- Brian Hill, Illinois Department of Transportation
- Jim Trepanier, Illinois Department of Transportation
- Michael Short, Illinois Department of Transportation
- Ron Wagoner, Illinois Department of Transportation
- Tim Murphy, Murphy Pavement Technology
- LaDonna Rowden, Illinois Department of Transportation
- Ally Kelley, Illinois Department of Transportation
- Dennis Bachman, Federal Highway Administration
- Charles Wienrank, Illinois Department of Transportation
- Kevin Burke, Illinois Asphalt Pavement Association

The contents of this report reflect the view of the authors, who are responsible for the facts and the accuracy of the data presented herein. The contents do not necessarily reflect the official views or policies of the Illinois Center for Transportation, the Illinois Department of Transportation, or the Federal Highway Administration. This report does not constitute a standard, specification, or regulation.

Trademark or manufacturers' names appear in this report only because they are considered essential to the object of this document and do not constitute an endorsement of product by the Federal Highway Administration, the Illinois Department of Transportation, or the Illinois Center for Transportation.

EXECUTIVE SUMMARY

Approximately 61.8% of vehicle miles traveled on the US federal-aid highway system do not meet the established standard of good ride quality, and approximately 17.4% fail to qualify for acceptable ride quality. Resurfacing moderately deteriorated Portland cement concrete (PCC) pavement with hot-mix asphalt (HMA) overlays is an efficient and common rehabilitation practice. The service life of HMA overlays plays a vital role in the pavement network's overall structural and functional health. Reflective cracking is the most common distress observed in HMA overlays. Because of discontinuities (e.g., joints and cracks) in existing PCC pavement, HMA reflective cracks may develop shortly after resurfacing. This project focused on optimizing HMA mix and thickness selection to mitigate reflective cracking of overlays. The outcomes will support the Illinois Department of Transportation (IDOT) in modifying specifications and updating its policies to implement a performance-based approach for HMA overlays and corresponding lift configurations.

Large-scale laboratory tests were conducted to assess the combined impact of HMA overlay mix and thickness on its performance to control reflective cracking. A testing device was designed and built in-house to simulate a real-world truckload using two actuators. Eight tests were conducted to evaluate a wide range of overlay mix and thickness combinations. Each HMA mix was characterized for its cracking potential, rutting susceptibility, and dynamic modulus. Given that average HMA densities were met, bonding efficiency, flexibility, and stiffness of HMA mixes as well as overlay thickness significantly affected an overlay's performance against reflective cracking. To delay failure, interlayer bonding should be properly achieved with existing pavement and between lifts to reduce joint opening and delays in debonding. An overlay comprised of a high modulus and flexible surface course, with a flexible binder course generally has superior performance to control reflective cracking. In addition, the thicker the HMA overlay, the more enhanced the resistance to reflective cracking. The research team identified optimal overlay configurations to control reflective cracking. For non-interstate projects, an overlay composed of an SMA-9.5 surface course and an IL-4.75 binder course are recommended. An IL-9.5FG surface course and an IL-4.75 binder course are recommended for low-volume and low-speed roads. For interstate projects, an overlay composed of an SMA-12.5 surface course and an IL-19.0 binder course is recommended. An SMA-9.5 surface course and an SMA-12.5 binder course are recommended when a thin structure is required.

A generalized 3D finite-element model was developed to predict an overlay's reflective cracking potential. Fracture properties such as stress intensity factor (SIF) and J-integral were modeled and computed. Average Mode I SIF was found to be a valid measure to rank an overlay's cracking potential. A data-driven surrogate model that can predict reflective cracking potential was developed. A database of 128 cases was generated to compute fracture parameters for a combination of inputs. Shapley Additive Explanations analysis confirmed the model's robustness. Engineers can easily use the surrogate model to select materials and design thicknesses.

Life-cycle cost analysis of the overlay alternatives was performed using IDOT's unit prices from contracts between 2018 and 2019. The experimental results were used to estimate the lifetime for each overlay scenario. Service lives of 10, 12, and 14 years were assumed for poor-, moderate-, and good-performance scenarios, respectively. An overlay composed of a 1.5 in (38.1 mm) SMA-9.5 or a

1.25 in (31.8 mm) IL-9.5FG surface course and a 0.75 in (19.1 mm) IL-4.75 binder course had the lowest annual cost per mile among non-interstates projects. For interstate projects, an overlay composed of a 2 in (50.8 mm) SMA-12.5 surface and a 2.25 in (57.2 mm) IL-19.0 binder was the most cost-effective. In addition, a sensitivity analysis was performed. Cut-off lifetimes were identified where the annual cost of the alternative scenario was equal to the cost of the control scenario.

In summary, to control reflective cracking and to reduce life-cycle cost, an overlay composed of an SMA-9.5 surface course and an IL-4.75 binder course were recommended for non-interstate projects. An IL-9.5FG surface course and an IL-4.75 binder course were suggested for low-volume and low-speed roads. For interstate projects, an overlay composed of an SMA-12.5 surface course and an IL-19.0 binder course was recommended. A data-driven surrogate model may be used to design overlay thicknesses.

TABLE OF CONTENTS

CHAPTER 1: INTRODUCTION	1
BACKGROUND.....	1
OBJECTIVE AND SCOPE	2
CHAPTER 2: CURRENT STATE OF KNOWLEDGE.....	3
REFLECTIVE CRACKING MECHANISMS.....	3
LARGE-SCALE TESTING SIMULATING REFLECTIVE CRACKING.....	5
ASPHALT OVERLAY DESIGN METHODS.....	8
MECHANISTIC EVALUATION OF ASPHALT OVERLAYS.....	10
SURVEY RESULTS.....	11
Introduction	11
Structural Design.....	12
Materials	13
Performance.....	14
CHAPTER 3: EXPERIMENTAL PROGRAM	16
HOT-MIX ASPHALT MATERIALS.....	16
MATERIAL CHARACTERIZATION	17
Illinois Flexibility Index Test	17
Hamburg Wheel-Tracking Test	19
Dynamic Modulus Test.....	20
LARGE-SCALE LABORATORY TESTING.....	21
Test Slab	21
Instrumentation	23
Testing.....	25
Results.....	27
DISCUSSION	44
Effect of Joint Opening.....	46
Effect of Debonding	47
Effect of HMA Modulus and Flexibility Index	49

Effect of Overlay Thickness	50
SUMMARY	50
CHAPTER 4: MECHANISTIC ANALYSIS	53
INTRODUCTION.....	53
MODEL DEVELOPMENT	53
Finite-Element Modeling	53
Fracture Modeling.....	56
MODEL RESULTS AND DISCUSSION	58
Crack Mouth Opening Displacement	59
Stress Intensity Factor and J-integral.....	62
MODEL VALIDATION	64
MODEL FOR PREDICTING REFLECTIVE CRACKING POTENTIAL	66
Simulation Matrix.....	66
Surrogate Model	67
SHAP Analysis	69
SUMMARY	70
CHAPTER 5: LIFE-CYCLE COST ANALYSIS.....	72
INTRODUCTION.....	72
HOT-MIX ASPHALT COST ANALYSIS.....	72
Summary Statistics for Overlay Activities	72
Cost Breakdown of Projects Per District.....	72
Mix Usage and Range Prices	73
HMA Unit Price Analysis.....	74
LIFE-CYCLE COST ANALYSIS	75
LCCA Assumptions and Considerations	76
Sensitivity Analysis	80
SUMMARY	83
CHAPTER 6: SUMMARY, FINDINGS, AND RECOMMENDATIONS.....	84
SUMMARY	84
MAJOR FINDINGS.....	85

RECOMMENDATIONS	85
REFERENCES	87
APPENDIX A: SLAB PREPARATION	91
SUBGRADE PREPARATION	91
CONCRETE SLAB PREPARATION	92
Slab Casting.....	92
Concrete Characterization	94
Compressive Strength.....	94
Modulus of Elasticity.....	95
TACK-COAT APPLICATION	96
APPENDIX B: PREDICTION TOOL FOR OVERLAY CRACKING POTENTIAL	97

LIST OF FIGURES

Figure 1. Schematic. Reflective cracking mechanisms caused by temperature variation and traffic loading. 3

Figure 2. Schematic. Fracture modes of reflective cracking. 4

Figure 3. Schematic. Crack patterns: HMA and HMA structure with a glass-grid interlayer. 5

Figure 4. Schematic. Primary and secondary reflective cracking because of interface debonding..... 5

Figure 5. Schematic. Test track and overlay configurations..... 6

Figure 6. Photo. Joint conditions and test section configurations. 7

Figure 7. Diagram. The reflective cracking model is integrated as a subroutine of the MEPDG software. ... 9

Figure 8. Diagram. Reflective cracking-based asphalt overlay thickness design and analysis system. . 10

Figure 9. Map. Neighboring DOTs contacted and responded to the survey..... 11

Figure 10. Chart. Number of survey respondents indicating their use of each overlay thickness. 12

Figure 11. Chart. Typical NMAS of overlay HMA. 13

Figure 12. Chart. Typical service life of non-interstate and interstate overlays. 15

Figure 13. Photo. Filling a front wheel loader with an asphalt mixture at a plant..... 16

Figure 14. Diagram. Example load-displacement curve obtained from I-FIT..... 17

Figure 15. Equation. Flexibility index formula. 17

Figure 16. Chart. I-FIT results..... 18

Figure 17. Chart. Effect of recycler heating on flexibility index. 19

Figure 18. Equation. Sigmoidal model used to fit master curves..... 20

Figure 19. Chart. Dynamic modulus master curve. 21

Figure 20. Diagram. Test slab. 22

Figure 21. Photo. Test slab construction. 23

Figure 22. Photo. Copper wires glued on an HMA surface (CD1–CD4)..... 24

Figure 23. Photo. An iPad taking pictures during a test. 24

Figure 24. Graph. LVDT locations. 25

Figure 25. Photo. Hydraulic loading system. 25

Figure 26. Diagram. Loading plate configuration. 26

Figure 27. Diagram. Steps of load..... 26

Figure 28. Chart. Load pattern.....	26
Figure 29. Chart. Densities of asphalt mixtures on test slabs.	27
Figure 30. Graph. Coring location.....	28
Figure 31. Chart. Vertical deflections of PCC slabs at the start of each test.....	28
Figure 32. Photo. Interstate control scenario: cross-section after testing.	29
Figure 33. Chart. Interstate control scenario: vertical deflections of the PCC slab.	29
Figure 34. Photo. Interstate control scenario: crack development.	30
Figure 35. Photo. Interstate alternative scenario 1: cross-section after testing.....	31
Figure 36. Chart. Interstate alternative scenario 1: vertical deflections of the PCC slab.	31
Figure 37. Photo. Interstate alternative scenario 1: crack development.....	32
Figure 38. Photo. Interstate alternative scenario 2: cross-section after testing.....	33
Figure 39. Chart. Interstate alternative scenario 2: vertical deflections of the PCC slab.	33
Figure 40. Photo. Interstate alternative scenario 2: crack development.....	34
Figure 41. Photo. Interstate alternative scenario 3: cross-section after testing.....	35
Figure 42. Photo. Interstate alternative scenario 3: vertical deflections of the PCC slab.....	35
Figure 43. Photo. Interstate alternative scenario 3: crack development.....	36
Figure 44. Photo. Non-interstate control scenario: cross-section after testing.....	37
Figure 45. Chart. Non-interstate control scenario: vertical deflections of the PCC slab.	37
Figure 46. Photo. Non-Interstate control scenario: crack development.	38
Figure 47. Photo. Non-interstate alternative scenario 1: cross-section after testing.....	38
Figure 48. Chart. Non-interstate alternative scenario 1: vertical deflections of the PCC slab.....	39
Figure 49. Photo. Non-interstate alternative scenario 1: crack development.....	40
Figure 50. Photo. Non-interstate alternative scenario 2: cross-section after testing.....	40
Figure 51. Chart. Non-interstate alternative scenario 2: vertical deflections of the PCC slab.....	41
Figure 52. Photo. Non-interstate alternative scenario 2: crack development.....	42
Figure 53. Photo. Non-interstate alternative scenario 3: cross-section after testing.....	42
Figure 54. Chart. Non-interstate alternative scenario 3: vertical deflections of the PCC slab.....	43
Figure 55. Photo. Non-interstate alternative scenario 3: crack development.....	44
Figure 56. Chart. Number of cycles to failure and ranking of non-interstate scenarios.....	45
Figure 57. Chart. Number of cycles to failure and ranking of interstate scenarios.	46

Figure 58. Chart. Relationship between joint opening and NMAS of binder course. 46

Figure 59. Chart. Relationship between overlay thickness and occurrence of debonding and slab faulting. 47

Figure 60. Chart. Relationship between total overlay thickness and load transfer efficiency. 47

Figure 61. Chart. Relationship between crack initiation and severe debonding in non-interstate scenarios. 48

Figure 62. Chart. Relationship between polymer-modification and debonding at the surface–binder interface. 49

Figure 63. Chart. Effect of FI on overlay performance against reflective cracking. 49

Figure 64. Chart. Effect of HMA modulus on overlay performance against reflective cracking. 50

Figure 65. Illustration. Stick-slip model. 54

Figure 66. Illustration. 3D FE testbed model. 55

Figure 67. Flowchart. Considerations of testbed model. 55

Figure 68. Illustration. Assigned crack front on the FE model (side view). 56

Figure 69. Illustration. Contours around the crack tip. 57

Figure 70. Graph. J-integral values for different contours. 58

Figure 71. Illustration. Cracked FE model for non-interstate control scenario. 59

Figure 72. Illustration. CMOD for two modes of cracking. 60

Figure 73. Plots. Displacement and CMOD for mode I cracking. 61

Figure 74. Plots. Displacement and CMOD for mode II cracking. 62

Figure 75. Plot. 3D plot of SIF versus time and length of the model ($1 \text{ MPa}\cdot\text{mm}^{0.5} = 28.8 \text{ psi}\cdot\text{in}^{0.5}$). 63

Figure 76. Illustration. Tensile strain distribution at the bottom of the binder course. 64

Figure 77. Illustration. PCC under loading (side view). 64

Figure 78. Graphs. Predicted versus actual fracture parameters using regression. 68

Figure 79. Graphs. Predicted versus actual fracture parameters using neural network. 69

Figure 80. Plot. Summary plot of neural network model for K_I using test dataset. 70

Figure 81. Chart. Total overlay HMA thicknesses (overlay projects 2018–2019). 73

Figure 82. Chart. Initial cost of considered provided projects (overlay projects 2018–2019). 73

Figure 83. Chart. Initial cost of considered alternatives and statewide average as well as maximum, average, and minimum initial costs for provided projects. 77

Figure 84. Chart. Annual cost per mile (\$/Yr) for considered overlay alternatives: (a) non-interstate and (b) interstate. 80

Figure 85. Chart. Annual cost per mile for control of interstate and non-interstate (statewide average). .	81
Figure 86. Chart. Hypothetical comparison of overlay alternatives (non-interstate).....	82
Figure 87. Chart. Hypothetical comparison of overlay alternatives (interstate).	82
Figure 88. Chart. Gradation of the subgrade material.	91
Figure 89. Photo. A vibratory compactor compacts the sand layer.....	91
Figure 90. Photo. Wood forms with ferrule loops.....	92
Figure 91. Photo. Curing condition of concrete cylinders.	93
Figure 92. Photo. Concrete casting.....	94
Figure 93. Equation. Compressive strength.	94
Figure 94. Chart. Compressive strength versus age for lab- and field-cured specimens.....	95
Figure 95. Photo. Test setup for the modulus of elasticity measurement.....	95
Figure 96. Equation. Modulus of elasticity.	96
Figure 97. Diagram. Tack coat application rate.....	96
Figure 98. Image. User interface of the tool.	97

LIST OF TABLES

Table 1. Key Findings of Full-Scale Testing (Yin & Barbagallo, 2014)	8
Table 2. Previous Works on Mechanistic Evaluation of Asphalt Overlay against Reflective Cracking... 10	10
Table 3. Design Details for HMA Mixes Used in This Project	17
Table 4. Hamburg Wheel-Tracking Test Results	20
Table 5. Lift Configurations and Testing Details	27
Table 6. Interstate Control Scenario: Results from Crack Detectors.....	30
Table 7. Interstate Alternative Scenario 1: Results from Crack Detectors.....	32
Table 8. Interstate Alternative Scenario 2: Results from Crack Detectors.....	34
Table 9. Interstate Alternative Scenario 3: Results from Crack Detectors.....	35
Table 10. Non-Interstate Control Scenario: Results from Crack Detectors.....	37
Table 11. Non-Interstate Alternative Scenario 1: Results from Crack Detectors.....	39
Table 12. Non-Interstate Alternative Scenario 2: Results from Crack Detectors.....	41
Table 13. Non-Interstate Alternative Scenario 3: Results from Crack Detectors.....	43
Table 14. Summary of Large-Scale Testing Results	45
Table 15. Fracture Parameters for Non-Interstate and Interstate Scenarios	65
Table 16. Ranking of Non-Interstate and Interstate Scenarios Based on Averaged Fracture Parameters (from Best to Worst).....	65
Table 17. Simulation Matrix for Non-Interstate and Interstate Scenarios.....	66
Table 18. Summary of Cost Analysis 2018 to 2019	74
Table 19. Unit Prices of Mixes in Each Overlay Scenario.....	75
Table 20. Three Considered Scenarios for LCCA.....	78
Table 21. Initial and Maintenance Costs Per IDOT’s Chapter 54 Manual and Templates.....	79
Table 22. Annual Cost Per Mile (\$/Yr) for Considered Overlay Alternatives	79
Table 23. Life-Cycle Cost for Control of Interstate and Non-interstate (Statewide Average).....	81
Table 24. Results of LWD Tests.....	92
Table 25. Truck Arrival Time and Fresh Concrete Properties.....	93
Table 26. Specimen Ages and Curing Conditions of Concrete Characterization Tests	94
Table 27. Suggested Range for Inputs in the Tool.....	98

CHAPTER 1: INTRODUCTION

BACKGROUND

Pavement condition impacts mobility, safety, vehicle-operating costs, and transportation infrastructure performance (Keenan et al., 2012). Approximately 61.8% of vehicle miles traveled on the US federal-aid highway system do not meet the established standard of good ride quality and around 17.4% fail to qualify for acceptable ride quality (USDOT, 2021). Hence, rehabilitation is needed to restore the structural and functional capacity of deteriorated pavements. Common rehabilitation methods include reconstruction, resurfacing, and recycling. Resurfacing a moderately deteriorated Portland cement concrete (PCC) pavement with hot-mix asphalt (HMA) layers is considered an efficient and common practice. The service life of HMA overlays plays a vital role in the overall structural and functional health of the pavement network. Factors affecting the service life of HMA overlays include traffic, environmental and climate conditions, existing pavement condition, drainage system, structural design, HMA material properties, and construction quality (Geoffroy, 1998; Dave, 2009; Newcomb, 2009; Watson & Heitzman, 2014).

Layer thickness is considered one of the most critical design parameters and cost considerations for overlays. There is a lack of proper design methods for HMA overlay layer thickness, so thickness is often determined based on mix type and/or past experiences. For example, the Illinois Department of Transportation (IDOT) requires overlay thickness to be at least three times the nominal maximum aggregate size (NMAS) of the HMA mix. However, if the condition requires a thickness more than the minimum, a review of distresses, construction history, and structural analysis will be conducted in a case-by-case manner. Hence, a wide range is expected for overlay service life. Therefore, it is imperative to understand the factors affecting the performance of HMA overlays to improve their design and service life efficiency.

Reflective cracking is the most common distress observed in HMA overlays. Because of discontinuities (e.g., joints and cracks) in existing PCC pavement, reflective cracks may develop shortly after HMA resurfacing. Reflective cracks allow water to penetrate the pavement structure, leading to roughness and spalling (Son & Al-Qadi, 2014). The primary reflective cracking mechanisms are horizontal and differential movements caused by temperature/moisture changes and traffic loads, respectively (Huang, 2004). For example, pavement temperature changes periodically and varies at different depths. Periodic variations induce cyclic contraction and expansion, and contraction leads to relatively uniform tensile stress in the entire HMA overlay. Because of accumulated horizontal movements at the joint, additional tensile stresses may build up in the HMA overlay. In addition to high stresses at the top and bottom of an HMA overlay, the temperature gradient causes warping of concrete slabs and aggravates horizontal movement. Traffic loads may induce both vertical and horizontal movements at the joint. When a tire moves, a series of tensile and shear stresses occur at the bottom of the HMA. The underlying PCC conditions may significantly affect the magnitude of the resulting shear and tensile stresses. Hence, reflective cracking development may be governed by bending stresses, shear stresses, or both. HMA is more brittle and relaxes slower at relatively low temperatures, so the chance of developing reflective cracking increases at lower temperatures.

Significant work has been conducted on reflective cracking mechanisms and potential methods to mitigate reflective cracking. In the field, reflective cracking may be studied once it reaches the overlay surface. This method leads to inconclusive results because of high variability (Maurer & Malasheskie, 1989; Bennert & Maher, 2008; Bennert et al., 2009; Elseifi et al., 2011). Models using layer theory or finite-element (FE) analysis have been developed to simulate reflective cracking mechanisms (Jayawickrama et al., 1987; Elseifi & Al-Qadi, 2004; Minhoto et al., 2008; Baek & Al-Qadi, 2009; Dave & Buttlar, 2010; Lytton et al., 2010; Wang et al., 2018; Xie & Wang, 2022). Compared to the linear elastic theory, FE analysis has the advantage of modeling complicated interlayer system geometry, moving traffic loads, and changing environmental conditions. However, mechanistic models, in addition to computational cost, often need extensive validation and calibration, limiting their abilities to guide HMA overlay design in the field.

Large-scale testing allows researchers to simulate the complex reflective cracking phenomenon realistically under a controlled environment. However, only a few large-scale testing attempts have been made because of the high cost and equipment constraints (Perez et al., 2007; Dave et al., 2010; Yin, 2015). In addition, large-scale testing is time-consuming, and it is difficult to localize measurements of the initiation and propagation of reflective cracks.

OBJECTIVE AND SCOPE

This project focuses on optimizing HMA mix and thickness selection to mitigate reflective cracking of overlays. This project will help IDOT adopt a performance-based approach for HMA mix overlays and lift configurations under their asset management program, as specified in Bureau of Design and Environment (BDE) Manual Chapter 53, by modifying specifications and updating policies. To meet the objective, balanced mix design and performance-based laboratory tests were performed to select HMA mixes. Large-scale laboratory tests were conducted to assess the combined impact of HMA overlay mix and thickness on its performance to control reflective cracking. FE analysis of overlay configurations complemented the laboratory testing. Life-cycle cost analysis (LCCA) was used to quantify the cost-effectiveness of various overlay configurations.

CHAPTER 2: CURRENT STATE OF KNOWLEDGE

This chapter reviews literature on the structural design, materials, and performance of HMA overlays. Outcomes of an online critical survey, where neighboring state departments of transportation (DOTs) shared their experiences concerning HMA overlay policies, are presented. Moreover, three large-scale tests on HMA overlay reflective cracking were reviewed.

REFLECTIVE CRACKING MECHANISMS

Reflective cracking involves the initiation and propagation of a discontinuity (e.g., joint or crack) from an underlying pavement through an HMA overlay. It is primarily observed in HMA overlays placed on existing PCC pavements. Strain concentration in the overlay is the primary mechanism for reflective cracking because of the movement of underlying pavement near joints or cracks. The movement could be induced by bending or shearing resulting from traffic loads and temperature changes, which result in differential and horizontal movements, respectively (Huang, 2004). Figure 1 presents a schematic of reflective cracking mechanisms.

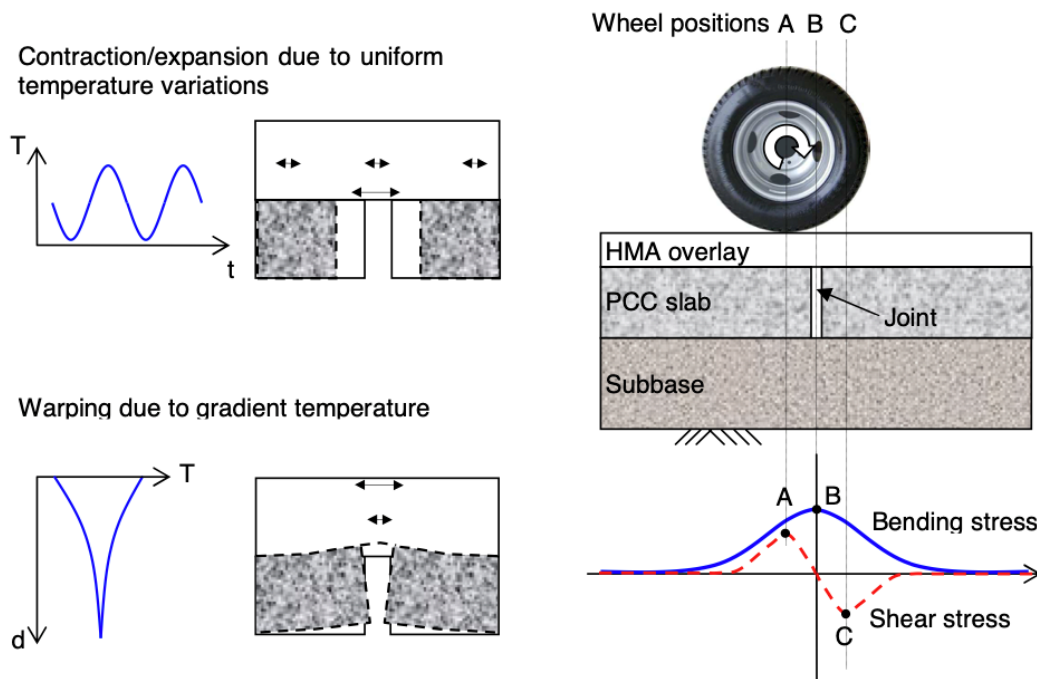


Figure 1. Schematic. Reflective cracking mechanisms caused by temperature variation and traffic loading.

Source: Baek (2010)

As presented in Figure 1, pavement temperature changes periodically and varies at different depths. Periodic variations induce cyclic contraction and expansion. Contraction leads to relatively uniform tensile stress in the entire HMA overlay. Because of accumulated horizontal movements at the joint, additional tensile stresses may add up in the HMA overlay, especially at the bottom of the HMA

overlay close to the joint. The temperature gradient results in higher thermal stresses at the top and bottom of the HMA layer, which is exacerbated by warping of the concrete slabs. Reflective cracking caused by thermal loading may develop at either the bottom or top of the HMA overlay (Dave & Buttlar, 2010).

Traffic loads may induce both vertical and horizontal movements at the joint. As presented in Figure 1, when a tire moves from position A to C, a series of tensile and shear stresses occur at the bottom of the HMA (Baek & Al-Qadi, 2009). The underlying PCC conditions may significantly affect the magnitude of the resulting shear and tensile stresses. Hence, reflective cracking development may be governed by bending or shear stresses, or both. HMA is more brittle and relaxes slower at lower temperatures, so the potential for developing reflective cracking is greater at lower temperatures than higher ones.

Cracks are categorized based on three loading modes. For Mode I (opening), principal loading is generally applied to a crack plane, and cracks grow perpendicular to the crack plane. For Modes II and III, cracks occur in in-plane and out-of-plane shear directions, respectively. Figure 2 presents the three reflective cracking modes for an HMA overlay on a PCC layer.

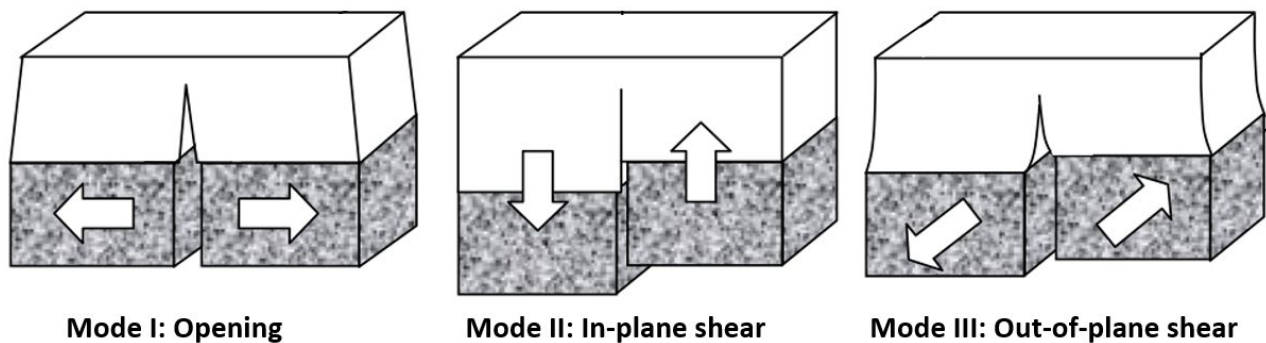


Figure 2. Schematic. Fracture modes of reflective cracking.

Source: De Bondt (2000)

Both temperature variation and traffic loading can result in the Mode I fracture. When temperature variation exists or tires are located directly on top of a joint, PCC slabs move horizontally, which induces horizontal strain accumulation in an HMA overlay. Traffic loading can also induce differential vertical (shear) movements of PCC slabs, resulting in Mode II fracture. Mode III fracture is rarely observed in HMA overlays (Lytton, 1989). Moreover, reflective cracking is typically a result of the combined fracture effects of Modes I and II.

Although reflective cracking is considered a bottom-up phenomenon, other crack patterns have been observed in field investigations, laboratory testing, and numerical simulations. As presented in Figure 3, Jayawickrama et al. (1987) observed three reflective cracking types in laboratory tests where horizontal loading was applied to two HMA layers with a glass-grid interlayer. Type I cracks initiate from the bottom of the overlay and propagate directly upward. Type II cracks initiate from the bottom but redirect at the interface. Type III cracks, in contrast, comprise of two cracks developed simultaneously from the bottom and top of the HMA overlay and head to the interface.

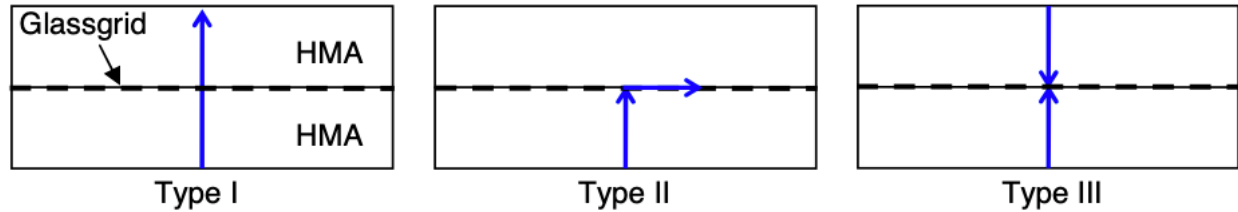


Figure 3. Schematic. Crack patterns: HMA and HMA structure with a glass-grid interlayer.

Source: Jayawickrama et al. (1987)

Sha (1993) found that surface-initiated thermal cracking was the primary source of distress in thick HMA overlays, while bottom-up reflective cracking occurred in thin HMA overlays. Similarly, Kuo et al. (2003) concluded that top-down cracking was more likely to occur in a thick overlay. They also reported that higher load transfer efficiency of the existing PCC layer could decrease the chance of bottom-up cracking, while increasing the potential for top-down cracking, because of lower stress concentration at the joint.

A reflective crack can initiate directly over or offset to a joint in the PCC layer. De Bondt (2000) found a secondary reflective crack initiated away from a joint after a primary reflective crack developed, as presented in Figure 4. Because of the double flexural deformation of the cracked overlay, the interface around the crack tip debonded. The primary reflective crack propagated twice as fast as the secondary crack at low bonding stiffness. As the bonding stiffness increased, the primary reflective crack propagated slower.

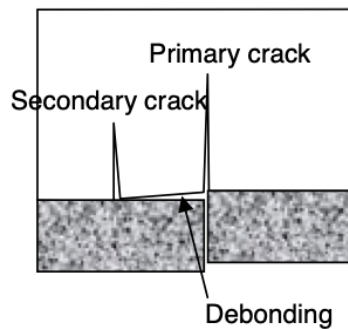


Figure 4. Schematic. Primary and secondary reflective cracking because of interface debonding.

Source: De Bondt (2000)

LARGE-SCALE TESTING SIMULATING REFLECTIVE CRACKING

Perez et al. (2007) conducted accelerated pavement testing (APT) to study traffic-induced reflective cracking in France. The tests were performed on a 98 ft (30 m) long track with eight discontinuities in the base layers, as presented in Figure 5. Three overlay configurations were considered: a 2.36 in (6 cm) regular bituminous (BBC) layer; a 0.79 in (2 cm) sand bituminous (SB) binder layer and a 1.57 in (4 cm) BBC surface layer; and a 0.39 in (1 cm) metallic grid (MG) reinforced binder layer and a 1.97 in (5 cm) BBC surface layer.

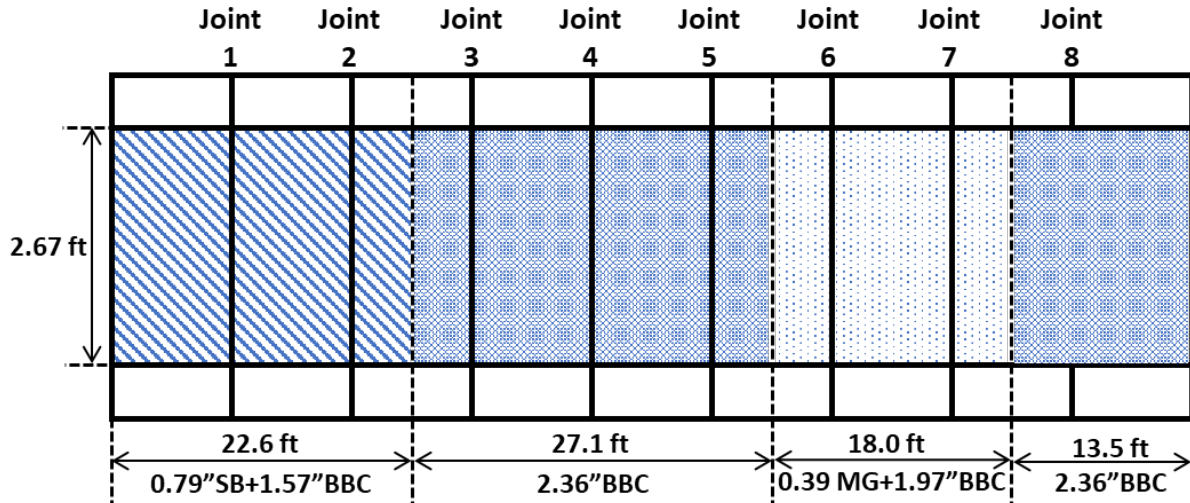


Figure 5. Schematic. Test track and overlay configurations.

Source: Perez et al. (2007)

The twin wheel applied a load of 14.6 kip (65 kN), which was half of the reference load of 14.33 tons (13 metric tons) on one single axle. Each machine had four twin wheels carried by a chain to apply the load within 6.6 ft (2 m) of the test track. To obtain reliable data on the propagation rate of reflective cracking, the track's width was reduced to 2.76 ft (0.84 m), allowing observation of the lateral faces of the track. Four types of sensors were instrumented on the test track: strain gauges, linear variable differential transformers, lateral cracking evolution sensors, and thermal couples.

Three series of tests were performed. Joints three and seven were tested in spring 2005 at an average temperature of 54°F (12°C). Double reflective cracking appeared on the surface after 450,000 passages in both cases. Joints two and six were tested in fall 2005 with an average temperature of 61°F (16°C). The former scenario occurred after one million passages, while the latter showed double reflective cracking after 450,000 passes. Testing on joints one and five started in winter 2006 but was completed in the summer because the APT machine broke. Joint one had neither creep failure nor reflective cracking on the surface, while joint five showed single reflective cracking after 500,000 passes.

Dave et al. (2010) performed testing using the Accelerated Test Loading Assembly (ATLAS) to study the jumping and offsetting mechanisms of reflective cracking. Four 125 ft (38 m) long pavement sections were constructed with the same underlying structure, consisting of a 6 in (152 mm) thick newly jointed plain concrete pavement (joint spacing at 12.5 ft [3.8 m]) on top of a 12 in (304 mm) granular subbase). Figure 6 summarizes the joint conditions and test section configurations. Instrumentation was installed to measure ground moisture levels, temperature profiles, and horizontal and vertical displacements at the PCC joints. They used ATLAS to apply 65,300 passes of varying load levels (5–30 kips [22.24–133.45 kN]) during the winter.

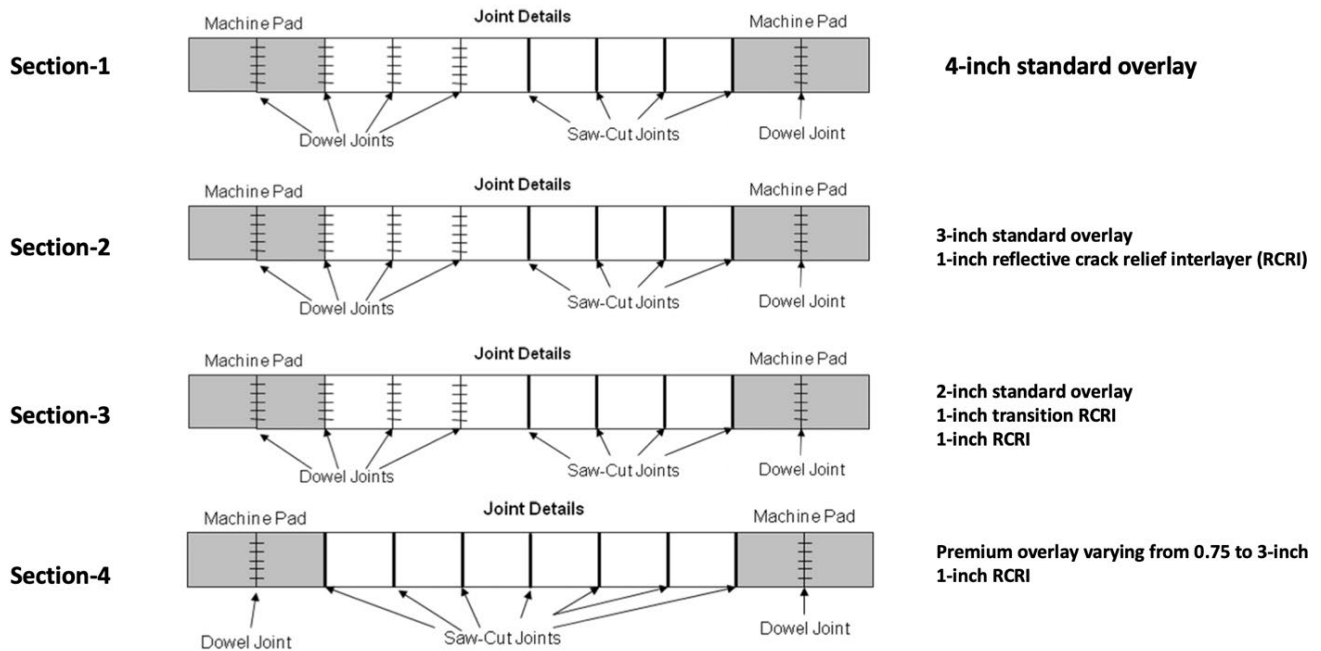


Figure 6. Photo. Joint conditions and test section configurations.

Source: Dave et al. (2010)

The following conclusions were drawn from Dave et al. (2010):

- The interlayer was intact, but hairline cracks had jumped into the bottom of the overlay at several locations.
- A second transitional interlayer above the standard reflective crack relief interlayer could mitigate crack jumping.
- Mixed-mode cracking followed the direction of slab faulting. Cracks propagated upwards first and then deviated diagonally toward the direction of the lower, faulted slab.
- Debonding between PCC and the HMA overlay occurred in all sections. The debonding amount correlated to load transfer efficiency.

The Temperature Effect Simulation System (TESS) was designed to simulate thermal-induced reflective cracking at the Federal Aviation Administration's National Airport Pavement Test Facility (Yin & Barbagallo, 2014; Yin, 2015). Hydraulic units were used to generate forces that can create horizontal displacement to simulate joint opening/closing induced by daily temperature changes.

Finite-element analysis was conducted to calculate the joint opening using pavement temperature predicted from the enhanced integrated climate model. Then, the temperature variation was replaced by mechanical load while the load magnitude was iteratively varied until the joint opening matched. Two phases of full-scale testing with different objectives were conducted; Table 1 summarizes the key findings.

Table 1. Key Findings of Full-Scale Testing (Yin & Barbagallo, 2014)

Phase	Objectives	Pavement Structure	Findings
I	<ul style="list-style-type: none"> Examine applicability of testing system Understand the mechanism of thermal-induced reflective cracking 	<ul style="list-style-type: none"> 5 in P-401 HMA 12 in P-501 PCC 	<ul style="list-style-type: none"> Non-uniform HMA-PCC interface conditions and tack coat application resulted in different hydraulic forces from TESS. A significant joint closing force was generated and accumulated at the bottom of the overlay because of no rest period. Loading rate substantially influenced crack propagation, especially when a crack reached upper portion.
II	<ul style="list-style-type: none"> Assess bottom-up reflective crack propagation rate 	<ul style="list-style-type: none"> 5 in P-401 HMA 12 in P-501 PCC 	<ul style="list-style-type: none"> “1 inch per year” rule of thumb is conservative Inclusion of a rest period at the end of each loading cycle allowed sufficient time for HMA overlay to relax. Once a bottom-up reflective crack reached a critical length, evolution became aggressive.

Yin and Barbagallo used crack detectors and strain gauges to monitor crack propagation. The crack detector was a strand of copper wire. Any erratic change in the output signal indicated a discontinuity. Instrumentation took place during and after the construction of the test section. Before placing the overlay lifts, H-type strain gauges were installed at the bottom of each lift close to the outer and inner edges. Five of the twelve strain gauges were damaged during construction, indicating their sensitivity. Field cores showed that H-type strain gauges interfered with localized strain response and somehow initiated top-down cracks in between. Yin and Barbagallo reported that the pavement surface was the most appropriate location for instrumentation.

ASPHALT OVERLAY DESIGN METHODS

The original *Mechanistic-Empirical Design Guide (MEPDG)* uses a purely empirical model to predict reflective cracks in HMA overlays or HMA surfaces of semi-rigid pavements (NCHRP 1-37A, 2004). The equation predicts the percentage of the area of cracks that propagate through the HMA as a function of time using a sigmoid function.

Lytton et al. (2010) developed a reflective cracking overlay design program. It uses a mechanistic-empirical (ME) model to predict the service life of a specified HMA overlay based on traffic and thermal stresses. A database consisting of stress intensity factors for a wide variety of conditions, pavement structures, and crack lengths was built using 2D FE analysis. Three models, representing different reflective cracking mechanisms (thermal, traffic bending, and traffic shearing), were developed using Artificial Neural Network (ANN) algorithms based on the database. As presented in Figure 7, the reflective cracking model was integrated as a subroutine of the AASHTOWare tool. A

total of 11 sets of calibration coefficients, which could predict the overlay performance for different climate zones, were developed based on more than 400 pavement test sections in 28 states.

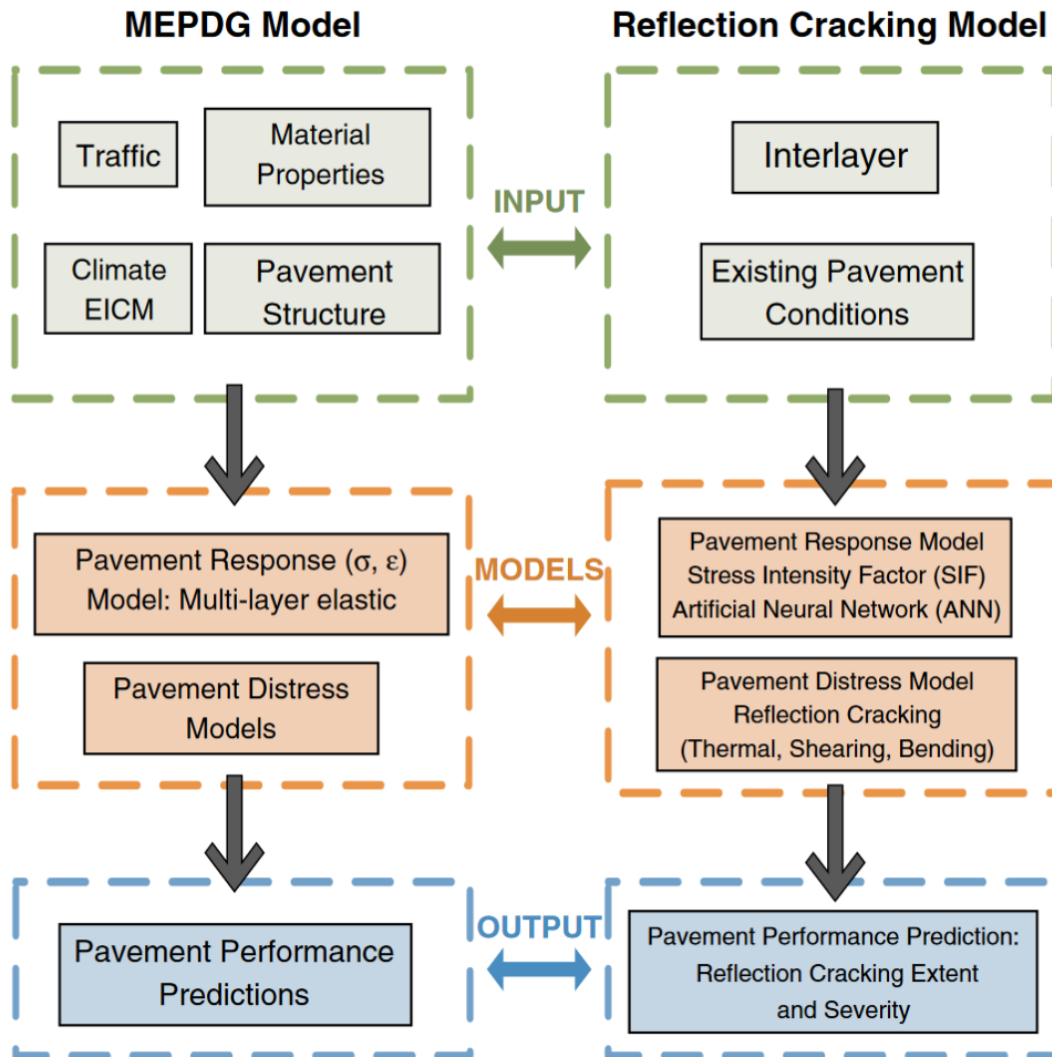


Figure 7. Diagram. The reflective cracking model is integrated as a subroutine of the MEPDG software.

Source: Lytton et al. (2010)

Zhou et al. (2010) developed an ME reflective cracking model, which was then integrated into an HMA overlay thickness design and analysis system, as presented in Figure 8 (Hu et al., 2010). The reflective cracking model was based on Paris' law. It uses the stress intensity factor (SIF) and HMA fracture properties (A and n parameters) obtained from the Texas overlay test. For traffic-induced reflective cracking, 32 regression equations were developed to predict the SIF of HMA overlays with various traffic-loading spectra (bending and shearing) and different load transfer efficiencies. For thermal-induced reflective cracking, the viscoelastic properties of HMA were considered through the thermal stress at the "far field," which was tied with the SIF determined through regression equations.

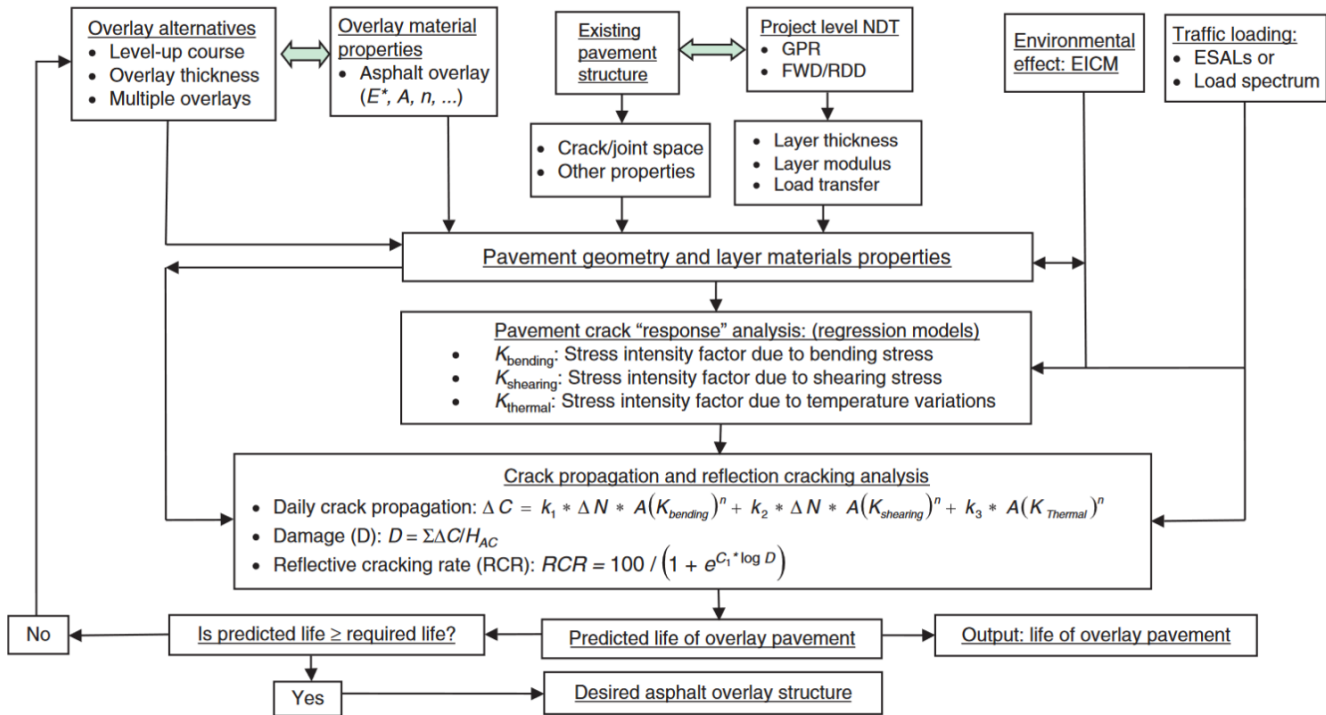


Figure 8. Diagram. Reflective cracking-based asphalt overlay thickness design and analysis system.

Source: Hu et al. (2010)

MECHANISTIC EVALUATION OF ASPHALT OVERLAYS

Scholars have performed extensive research to evaluate the performance of HMA overlays using mechanistic approaches. Table 2 provides a summary of existing work.

Table 2. Previous Works on Mechanistic Evaluation of Asphalt Overlay against Reflective Cracking

Category	Researchers	Objective
Finite element plus fatigue models	Francken & Vanelstraete (1992)	2D FE to study effect of interface systems on overlays
	Sousa et al. (2001)	Mechanistic-empirical-based overlay design method for reflective cracking
	Minhoto et al. (2008)	3D FE to study the effect of temperature variation on reflective cracking
FE plus fracture mechanics	Elseifi & Al-Qadi (2004)	Overlay service-life prediction model against reflective cracking
	Lytton et al. (2010)	Mechanistic-based models to predict the extent and severity of reflective cracking
	Xie & Wang (2022)	3D FE to simulate thermal-induced reflective cracking

Category	Researchers	Objective
Cohesive zone modeling	Baek & Al-Qadi (2006)	Effect of steel reinforcement interlayer on retarding reflective cracking
	Baek et al. (2010)	Effects of interface conditions on reflective cracking development
	Dave & Buttlar (2010)	Simulate thermal reflective cracking
	Baek & Al-Qadi (2011)	Effect of sand mix interlayer on controlling reflective cracking
	Rith & Lee (2022)	Cohesive-zone-based prediction model for reflective cracking
Extended FE method	Wang et al. (2018)	Simulate reflective cracking under cyclic temperature
	Ling et al. (2018)	Investigate the influences of geotextiles on reducing thermal reflective cracking
	Wang & Zhong (2019)	Investigate the influence of a tack coat on reflective cracking propagation

SURVEY RESULTS

Introduction

The research team contacted Illinois' neighboring DOTs to document their experiences with HMA overlay policies. They divided the states into two groups based on proximity to Illinois (Figure 9). States in group one (colored in red) have comparable climates to Illinois and extensive HMA overlay experiences. States in group two (colored in purple) have either similar climates or considerable experiences. The researchers received 10 responses, which are marked with dark green stars.

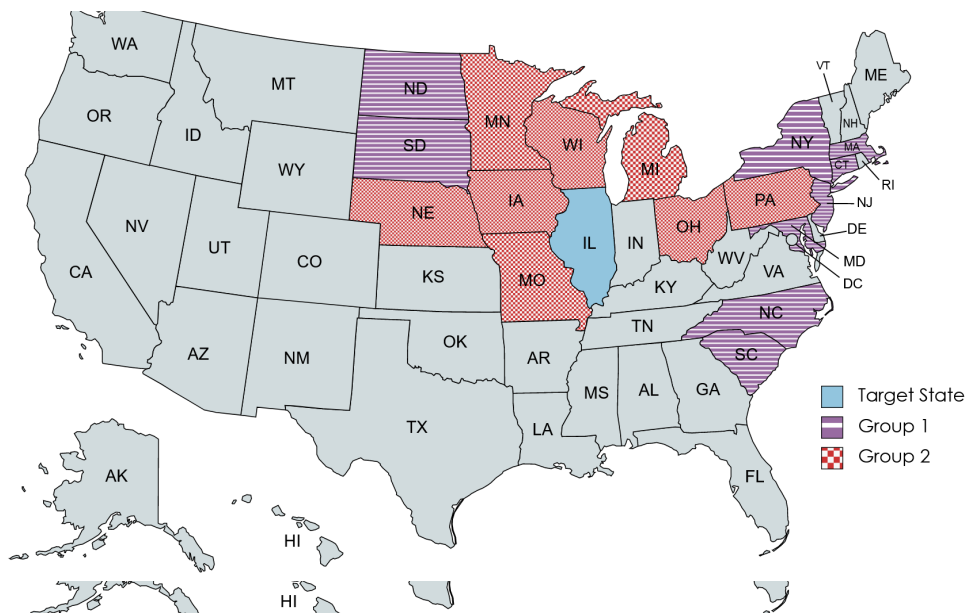
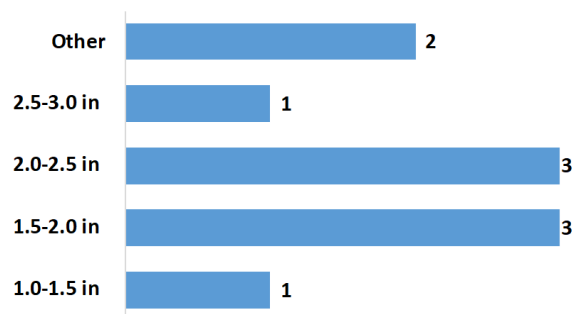


Figure 9. Map. Neighboring DOTs contacted and responded to the survey.

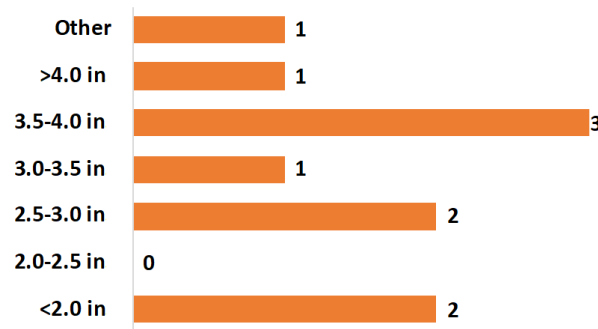
Structural Design

State DOTs were asked to list standard overlay configurations. A non-interstate overlay typically consists of one (single surface course) or two (thick/leveling binder course and wearing surface course) lifts, depending on total thickness, traffic, and existing pavement condition. Meanwhile, an interstate overlay often consists of one (single surface course), two (thick binder course and wearing surface course), or three (leveling binder course, binder course, and wearing surface course) lifts.

Overlay thickness is one of the most critical design parameters and cost considerations for HMA overlays. Figure 10-A presents the typical overlay thickness used on non-interstate projects. The most commonly used overlay thickness ranges from 1.5 to 2.5 in (38 to 64 mm). Figure 10-B illustrates the typical overlay thickness used on interstates. The most often employed thickness on interstate projects is between 2.5 to 4.0 in (64 to 102 mm).



A. Typical overlay thickness for non-interstate projects



B. Typical overlay thickness for interstate projects

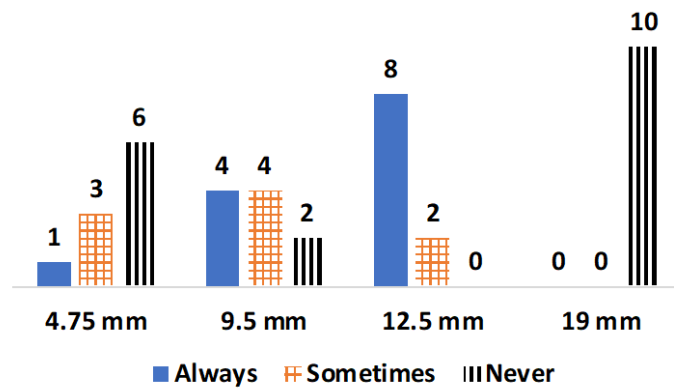
Figure 10. Chart. Number of survey respondents indicating their use of each overlay thickness.

To select the appropriate thickness for overlays, the traffic, existing pavement condition, environmental effects, road classification, cost, public policy, and ease of implementation must be considered. The most practical design strategy is to correlate with past experiences and develop a policy to determine the thickness that works best in the considered region and update it periodically. DOTs often specify a minimum thickness based on NMAAS. For example, 7 of the 10 surveyed states (including Illinois) require the layer thickness to be at least three times the NMAAS, while the remaining surveyed states specify at least four times the NMAAS.

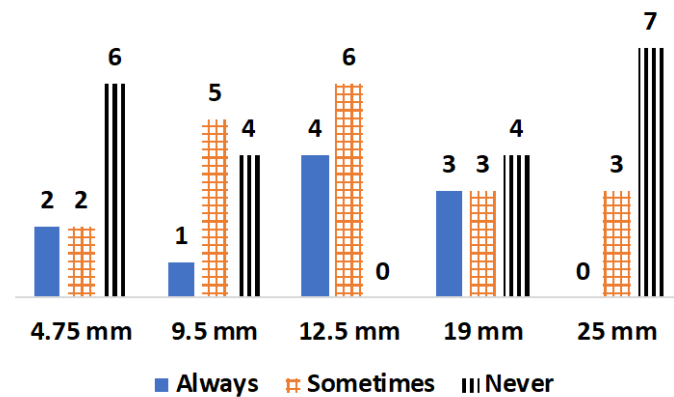
A design method can be used to determine the thickness when the pavement condition requires an overlay thicker than the minimum. The 1993 AASHTO method is the most used structural design approach by responding state DOTs, followed by the AASHTOWare tool and an agency-specified ME model.

Materials

The mixture type and quality of HMA substantially affect the reflective cracking potential of an overlay (Baek & Al-Qadi, 2011; Son et al., 2016; Watson & Heitzman, 2014). Figure 11 presents the typical NMAS used for surface and binder course mixtures for an HMA overlay. As demonstrated, 0.5 in (12.5 mm) is the most widely used NMAS for the surface layer, followed by 0.375 in (9.5 mm). None of the respondents used 0.75 in (19.0 mm) NMAS for the surface course. Because HMA mixes with a smaller NMAS tend to be easier to compact, they are more likely to perform better in the field than HMA mixes with a larger NMAS (Bonaquist, 2011). It is worth noting that the reduced NMAS in asphalt mixtures can result in decreased interconnectivity of void space, which in turn can lead to a lower level of permeability. Moreover, reducing the NMAS could lower the minimum required layer thickness and corresponding construction costs.



A. Number of states surveyed indicating their use of each NMAS for surface course mixtures



B. Number of states surveyed indicating their use of each NMAS for binder course mixtures

Figure 11. Chart. Typical NMAS of overlay HMA.

Meanwhile, HMA mixtures with a NMAS of 0.5 in (12.5 mm) and 0.75 in (19 mm) are often used for binder courses, followed by 0.375 in (9.5 mm) and 0.188 in (4.75 mm). The 1 in (25 mm) NMAS HMA mixture is rarely adopted. A leveling or binder course is often placed on the milled pavement and below the surface course. It provides a construction platform over the milled surface to allow a smooth surface course to be placed. Leveling courses are typically 0.188 in (4.75 mm) or 0.375 in (9.5 mm) fine-graded HMA mixes, constructed as a relatively thin lift. In contrast, when a binder course is used as a structural layer, a larger NMAS HMA mix is preferred. A 0.75 in (19 mm) coarse-graded mix is commonly used as a binder course for Illinois interstates. However, because of segregation and compaction issues caused by large aggregate particles, states such as Wisconsin and Ohio use 0.5 in (12.5 mm) and 0.375 in (9.5 mm) dense-graded mixes.

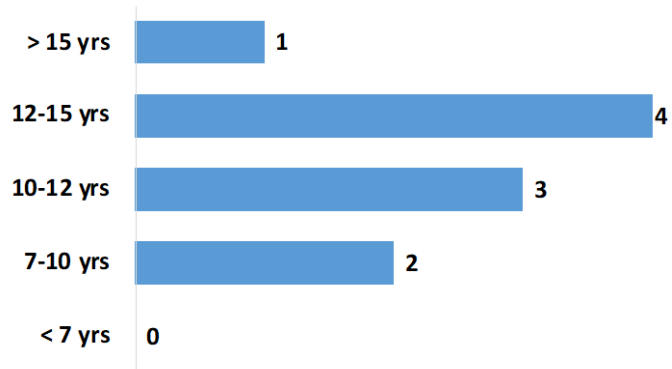
Stone-matrix asphalt (SMA) is widely considered a premium surface or binder course option. However, SMA may be a cost-effective alternative when life-cycle cost is considered (Newcomb, 2009; Son et al. 2016). Several DOTs reported that SMA could deliver superior performance to conventional dense-graded mixes, especially on high-traffic roads. A 0.5 in (12.5 mm) NMAS SMA has been used as a surface mix since its introduction in the US; some agencies also use 0.375 in (9.5 mm) NMAS SMA in overlay surface course construction.

For non-interstate projects, a fine-graded 0.375 in (9.5 mm) NMAS HMA is becoming a popular surface course for low- to medium-speed overlays by many state DOTs. It is preferred because it is more workable, less permeable, less likely to segregate, and more economical. The fine-graded HMA mix was initially eliminated from the recommended gradation bands of the SuperPave specifications. It was re-added because of the need for small-sized aggregate mixtures (West et al., 2006). However, because of its inadequate friction, especially under wet conditions, its use on surface courses is limited to low-volume and low-speed roads (Rahman et al., 2011). However, IDOT has successfully used fine-graded HMA mixes on the surface.

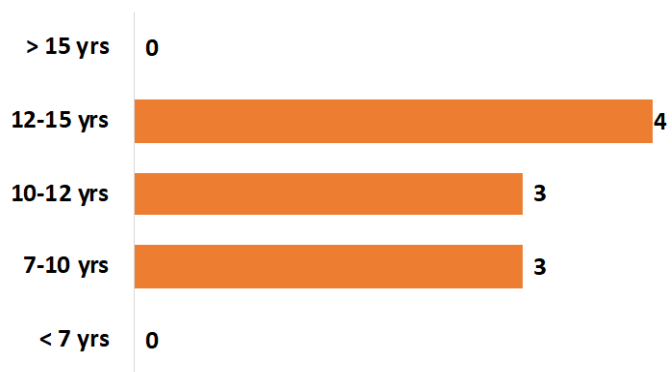
Eight out of ten states responded that polymer-modified binders are always used in their interstate HMA overlay mixtures, while the remaining states use them infrequently. However, only two states always use polymer-modified binders in non-interstate overlays, and the remaining states sometimes use them. To determine when to use modified binders, state DOTs usually decide based on traffic, condition of existing pavement, and climate. South Dakota reported that polymer-modified binders are used in all their overlay mixes, while Wisconsin employs them in all SMA binders. When asked about binder adjustment policies, New Jersey decided on binder adjustments based on balanced mix design results. Wisconsin reported that a low-temperature performance grade of -29.2°F (-34°C) is always required for the upper layer in the state's northern half.

Performance

State DOTs were asked to rank the types of distresses most often observed in HMA overlays. The top three distresses include reflective cracking, transverse thermal cracking, and centerline joint deterioration. Both rutting and fatigue cracking were rarely noted, according to the responses. Figure 12 illustrates the typical service life of HMA overlays. As presented, non-interstate and interstate HMA overlays usually have service lives of 7 to 15 years.



A. Typical service life of non-interstates overlays



B. Typical service life of interstate overlays

Figure 12. Chart. Typical service life of non-interstate and interstate overlays.

CHAPTER 3: EXPERIMENTAL PROGRAM

Large-scale laboratory tests were conducted to assess the combined impact of HMA overlay mix and thickness on its performance to control reflective cracking. The testing device was designed and built in-house to simulate a real-world truckload using two actuators. Eight tests were conducted to evaluate a wide range of HMA mix and thickness combinations. The Illinois Flexibility Index Test (I-FIT), Hamburg wheel-tracking test (HWTT), and dynamic modulus test (E^*) were performed to characterize each HMA mix for cracking potential, rutting potential, and its dynamic modulus, respectively. By analyzing instrumentation data and correlating large- and small-scale tests, factors that significantly affect an overlay's performance against reflective cracking were identified and optimal overlay configurations were proposed.

HOT-MIX ASPHALT MATERIALS

HMA mixes in this project covered a broad spectrum of types commonly used in Illinois for overlay paving. Six HMA mixtures were collected from various plants during 2020–2022. The sampling procedure is summarized as follows. A front wheel loader was filled with approximately 1.1 US tons (1 ton) of HMA mixture directly from the plant silo, as presented in Figure 13. Around 45 five-gallon (19 L) metal buckets were lined up on the ground. They were filled by scooping and dumping the HMA material. The buckets were sealed, loaded into a trailer, and transported to the University of Illinois Urbana-Champaign's Illinois Center for Transportation (ICT). Sampled HMA mixtures were stored in climate-controlled storage at 50°F (10°C) before testing, eliminating the shelf-aging effect (Al-Qadi et al., 2019). Table 3 summarizes the HMA mix designs.



Figure 13. Photo. Filling a front wheel loader with an asphalt mixture at a plant.

Table 3. Design Details for HMA Mixes Used in This Project

ID	Mix Type	N-Design	NMAS	Asphalt Binder %	Virgin Binder Grade	ABR %
IL-4.75	Dense Graded	50	4.75	8.2	SBS PG 70-22	10.0
IL-9.5	Dense Graded	70	9.5	6.1	PG 58-28	29.3
IL-9.5FG	Dense Graded	90	9.5	5.9	SBS PG 70-22	0.0
IL-19.0	Dense Graded	70	19.0	5.3	PG 58-28	20.0
SMA-9.5*	SMA	80	9.5	6.6	SBS PG 76-22	9.8
SMA-12.5	SMA	80	12.5	6.3	SBS PG 76-28	14.7

* SMA-9.5 composites Illinois local gravels only.

MATERIAL CHARACTERIZATION

The I-FIT, HWTT, and E* tests were performed to characterize each HMA mix for cracking potential, rutting potential, and its dynamic modulus, respectively. Note that the materials were sampled and compacted at the time of overlay placement.

Illinois Flexibility Index Test

The I-FIT was used to investigate HMA cracking potential. The flexibility index (FI) parameter is based on fracture mechanics and is used as a parameter to screen HMA mixes for cracking potential. Details about I-FIT may be found elsewhere (Al-Qadi et al., 2015; Ozer et al., 2016a; Ozer et al., 2016b).

Figure 14 presents the main output of the test.

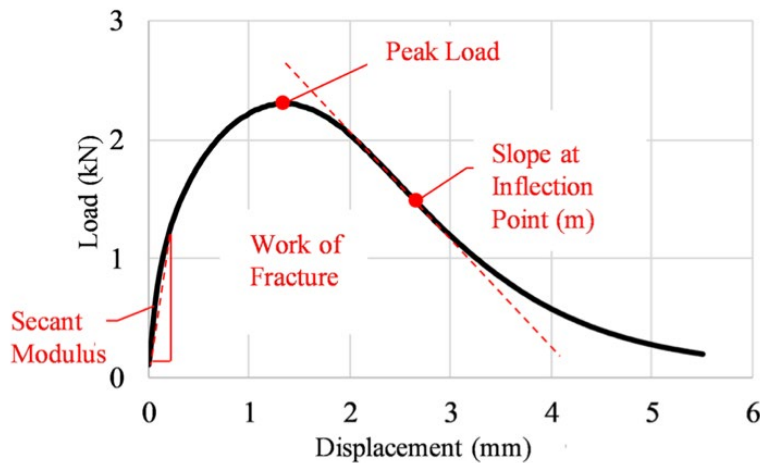


Figure 14. Diagram. Example load-displacement curve obtained from I-FIT.

Source: Ozer et al. (2016a)

The FI is obtained using Figure 15. Higher values of FI indicate greater resistance to cracking:

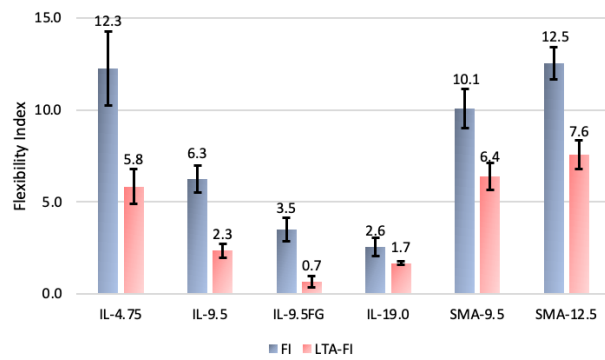
$$FI = A * \frac{G_f}{abs(m)}$$

Figure 15. Equation. Flexibility index formula.

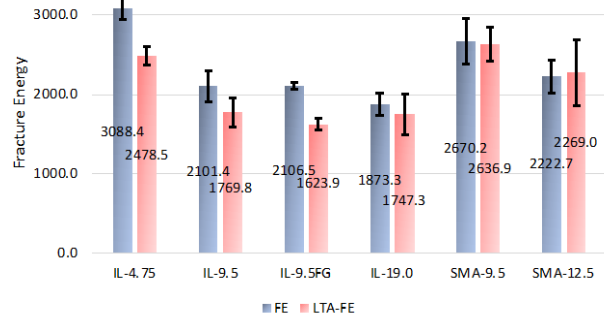
where G_f is the apparent fracture energy, defined as the area under the load-displacement curve divided by fractured area (area defined by ligament length and specimen thickness); J/m^2 ; m is the post-peak slope at the inflection point, kN/mm ; and A is a scaling coefficient taken as 0.01.

I-FIT was conducted on materials sampled when compacting test slabs. HMA mixtures were preheated in five-gallon metal buckets to a loose state in forced-draft ovens for about three hours at 311°F (155°C). The HMA materials were loaded into the mixing chamber of a recycler mixer using its conveyor. They were mixed and heated at 400°F (204°C) for 30 to 40 minutes before discharging from the recycler for compaction. Both unaged and long-term aged specimens were considered. Four replicates were tested for each HMA mix at each aging condition. The FI value farthest from the average of the four test specimens was discarded for reporting purposes in accordance with Illinois Modified AASHTO T 393 (2022). Figure 16-A, Figure 16-B, Figure 16-C, and Figure 16-D compare the FI, G_f , $|m|$, and strength, respectively, of the six HMA mixes.

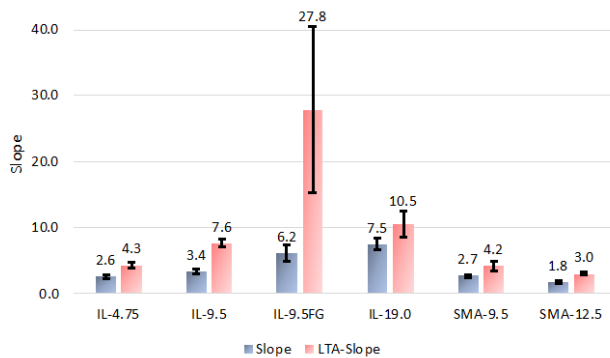
IL-4.75, SMA-9.5, and SMA-12.5 had relatively higher FI, indicating greater cracking resistance. In contrast, IL-9.5, IL-9.5FG, and IL-19.0 had relatively lower FI, suggesting they are possibly prone to cracking.



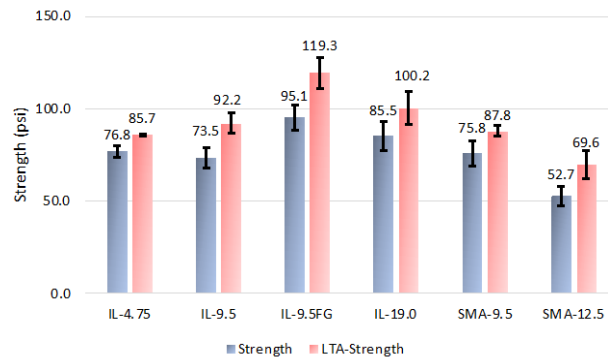
A. Flexibility Index



B. Fracture Energy



C. Slope at Inflection Point



D. Strength

Figure 16. Chart. I-FIT results.

The HMA mixes had considerably low FI. To investigate whether the re-heating process significantly lowered the flexibility index, the I-FIT test was repeated using four HMA mixtures with material remaining at the end of the project. The four mixes were not heated in the recycler. Mixtures in five-gallon metal buckets were preheated in forced-draft ovens for about three hours at 311°F (155°C). The materials were blended and split. The objective of splitting was to homogenize the sampled material and prepare batches containing the required materials necessary for compaction (14.3 lb [6.5 kg]). The final material batches were poured into paper buckets. Next, the batched samples were conditioned for two hours at 311°F (155°C) to achieve compaction temperature.

Figure 17 compares the FI obtained from specimens produced from the two heating procedures. Although the relative ranking remains the same, recycler heating significantly reduced FI. This finding is due to the high heating temperature (400°F [204°C]), as the heating duration was shorter than oven heating. The differences were more obvious for IL-19.0 and SMA-12.5 because of the longer recycler-heating duration, which is required for larger quantities. Moreover, the differences became less obvious for long-term aged samples.

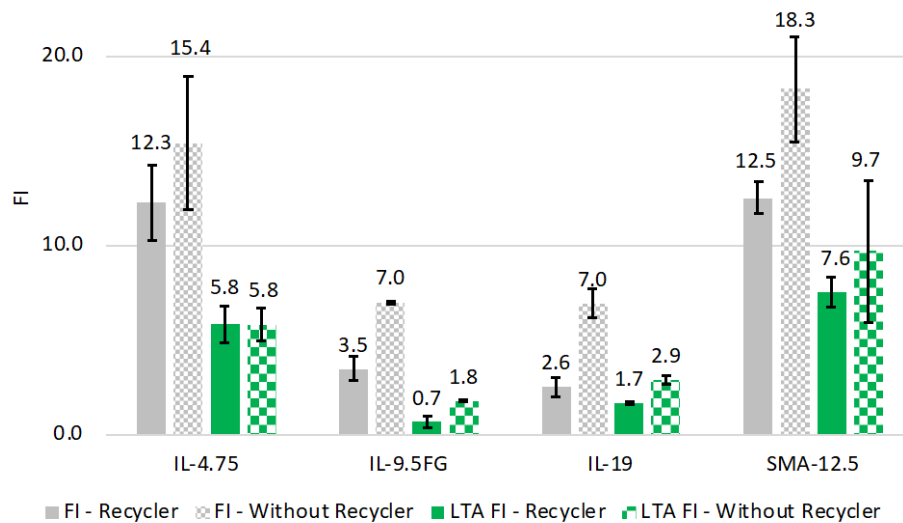


Figure 17. Chart. Effect of recycler heating on flexibility index.

Hamburg Wheel-Tracking Test

HWTT evaluates HMA’s susceptibility to permanent deformation. The testing procedures specified in AASHTO T 324 (2019) were followed in this study. Each of the two sets used in the machine comprises two cylindrical specimens with a 5.9 in (150 mm) diameter and a 2.4 in (62 mm) height. Each specimen was placed in a mounting tray, submerged in a warm water bath at 122°F (50°C), and subjected to repetitive steel-wheel sinusoidal loading. The steel wheel weighs 158 lb (71.67 kg) and applies 52 passes per minute across each set. Table 4 summarizes the testing results. All HMA mixes passed IDOT’s rut depth requirement of 0.5 in (12.5 mm) at the specified number of wheel passes.

Table 4. Hamburg Wheel-Tracking Test Results

ID	No. Passes Threshold	Rut Depth (mm)
IL-4.75	10,000	5.6
IL-9.5	7,500	7.2
IL-9.5FG	15,000	7.5
IL-19.0	7,500	6.1
SMA-9.5	20,000	5.3
SMA-12.5	20,000	4.4

Dynamic Modulus Test

The main purpose of the dynamic modulus test is to determine the viscoelastic behavior of HMA under repeated loading by assessing the stress-to-strain relationship of the material subjected to continuous sinusoidal loading. The main output of the test is the dynamic modulus ($|E^*|$). The test was performed in accordance with AASHTO T 342 (2011), in which cylindrical specimens of 3.9 in (100 mm) diameter and 5.9 in (150 mm) height were cored from gyratory-compacted specimens and tested at five temperatures—14°F (−10°C), 39.9°F (4.4°C), 70°F (21.1°C), 100°F (37.8°C), and 129.2°F (54°C)—and under six loading frequencies—0.1, 0.5, 1, 5, 10, and 25 Hz. Four replicates were tested for each HMA mix. The $|E^*|$ values of each mix were taken as the average of the four replicates.

A master curve for complex modulus was constructed for each HMA mix at a reference temperature of 70°F (21°C), following the time-temperature superposition principles. A sigmoidal model was fitted for the modulus master curves following Figure 18.

$$\log E^* = \delta + \frac{\alpha}{1 + e^{\beta + \gamma \cdot \log f_r}}$$

Figure 18. Equation. Sigmoidal model used to fit master curves.

where, δ is minimum E^* value, α is span of E^* values, β and γ are shape parameters of function, and f_r is reduced frequency.

Figure 19 presents the dynamic modulus master curves for all HMA mixes. SMA-9.5 and IL-9.5FG had similar moduli across the frequency range and showed relatively high moduli. Meanwhile, SMA-12.5 and IL-4.75 demonstrated relatively low modulus. They had similar moduli at low frequencies, while the IL-4.75 modulus surpassed SMA-12.5 at high frequencies. IL-9.5 and IL-19.0 had lower moduli at low frequencies than those of SMA-9.5 and IL-9.5FG. However, the four mixes tend to converge at high frequencies, indicating that they had similar elastic behavior at low temperatures.

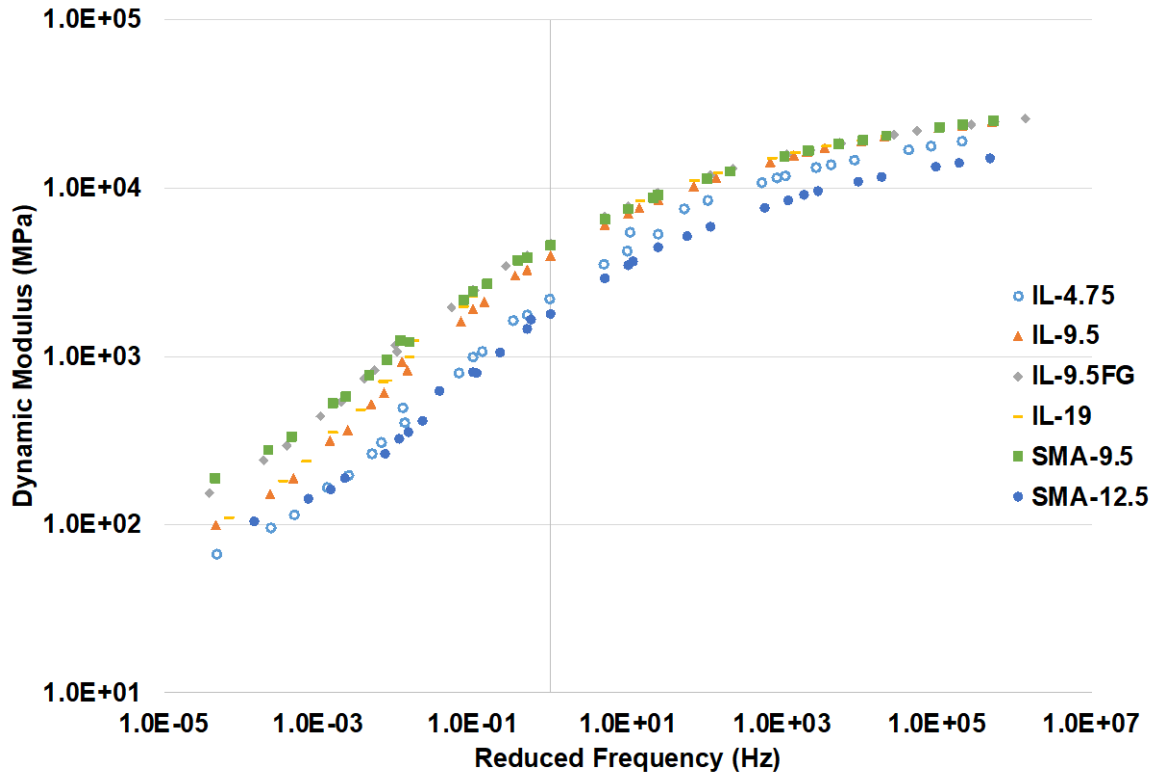


Figure 19. Chart. Dynamic modulus master curve.

The dynamic modulus was decomposed into storage and loss parts using a Fourier transformation. Then, both components determined the Prony series parameters, including instantaneous modulus, through the nonlinear least square fit. The linear viscoelastic model expressed by the Prony series was used to represent the time-temperature-dependent behavior of HMA in the FE analysis presented in Chapter 4.

LARGE-SCALE LABORATORY TESTING

Test Slab

A 12 in (305 mm) sand layer was placed in a 10 × 6 ft (3 × 1.8 m) testbed and compacted by a vibratory compactor. Detailed procedures and subgrade characterization can be found in Appendix A. Four 6 × 3 ft (1.8 × 0.9 m) neoprene rubber sheets with a total thickness of 3.75 in (95.25 mm) were placed in an excavated area on the subgrade to accelerate the testing and simulate subgrade deterioration near the concrete joint. Concrete slabs were cast, each measuring 6 × 6 ft (1.8 × 1.8 m) square and 7 in (177.8 mm) thick. Detailed steps and concrete characterization can be found in Appendix A.

As presented in Figure 20, each test slab had four layers: a 12 in (305 mm) fine sand subgrade, a 7 in (178 mm) PCC slab, a binder course, and a wearing surface. Each test slab had a similar PCC slab and the same subgrade to ensure a fair comparison between HMA overlays.

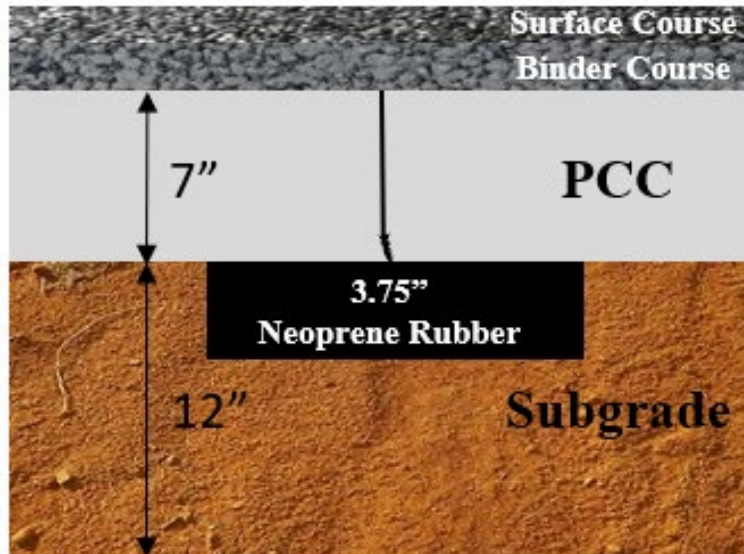


Figure 20. Diagram. Test slab.

As presented in Figure 21, constructing a test slab involves the following steps:

1. **Concrete slab placement.** The concrete slabs were stored outside after casting. In preparation for testing, a slab was saw cut to around 6 in (152.4 mm) depth. The joint measured 0.31 in (8 mm) wide. It was then brought indoors. A crane was used to lift the slab onto the test bed and situated on the subgrade. The center 3 ft (0.9 m) of the concrete slab was in direct contact with the neoprene rubber sheet, while the rest was in direct contact with the sand subgrade.
2. **Tack coat application.** A tack coat was applied to the PCC surface two hours before HMA placement. An application rate of 0.05 lb/ft² (0.244 kg/m²) was used. To accelerate debonding between PCC and binder course in the potential crack zone (i.e., center 2 feet), the application rate was reduced by 50%. Detailed procedures can be found in Appendix A.
3. **Preheating.** HMA mixtures were preheated to a loose state in forced-draft ovens for about three hours at 311°F (155°C).
4. **Remixing.** The HMA materials were loaded into the mixing chamber of a recycler mixer using its conveyor. They were mixed and heated at 400°F (204°C) for 30 to 40 minutes before discharging from the mixer.
5. **Discharging.** The produced materials were discharged from the back of the recycler mixer and loaded into the steel bucket of a Bobcat skid-steer loader. The temperature of the discharged HMA mix was carefully monitored throughout the production process. The mixing time was adjusted to ensure the discharge temperatures were close to 315°F (157°C) for unmodified mixes and 325°F (163°C) for polymer-modified mixes.

6. **Laydown.** The HMA mixture was dumped into the testbed, spread uniformly over the entire PCC slab, and leveled to approximately 1.25 times the target lift thickness.
7. **Compaction.** A single-drum vibratory roller compactor was used to compact the lift. The vibration was turned off when compacting the IL-4.75 mix.
8. **Surface course construction.** The following day, steps 2 to 7 were repeated to construct the surface course. The only difference was the tack coat application rate, where 0.025 lb/ft² (0.122 kg/m²) was used for the entire area.
9. **Saw cutting.** A 1 ft (30 cm) edge of the test slab was cut and removed to create a smooth and clean cross-section to observe and measure reflective crack propagation.

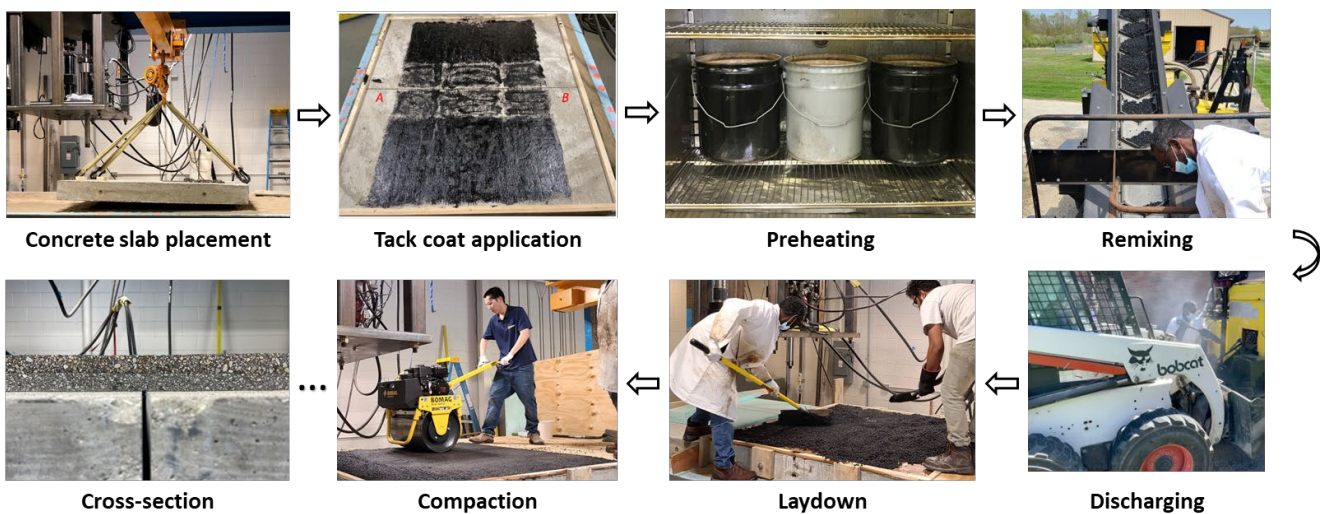


Figure 21. Photo. Test slab construction.

Instrumentation

The main goal for slab instrumentation was to monitor reflective crack initiation and propagation. Moreover, measuring PCC slab movement was vital to better understanding reflective cracking mechanisms.

Crack Detector

The crack detector (CD) is a single strand of copper wire. Any erratic change in the recorded voltage indicates a discontinuity, meaning a crack propagates through. Multiple copper wires were glued on the clean and smooth surface of the potential crack zone, as presented in Figure 22. A thin layer of adhesive coating was applied afterward for protection. The copper wires were connected to a laboratory power supply. A data acquisition system was used to record output signals throughout a test.



Figure 22. Photo. Copper wires glued on an HMA surface (CD1–CD4).

Digital Camera

A crack detector provides localized information and may not describe the complex cracking phenomenon. To overcome this limitation, an iPad was used to take pictures of potential crack zones every 100 loading cycles (i.e., 70 sec) during the testing, as presented in Figure 23.



Figure 23. Photo. An iPad taking pictures during a test.

Linear Variable Differential Transformer

Two linear variable differential transformers (LVDTs) were used to measure the vertical movement of the PCC slab, as presented in Figure 24. LVDTs were placed at locations L and R to measure vertical deflections of the PCC slab on both sides of the joint.

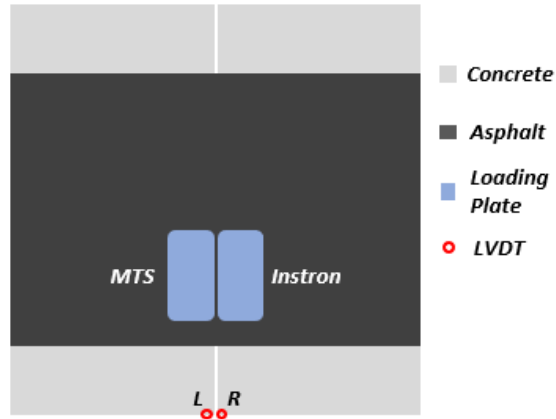


Figure 24. Graph. LVDT locations.

Testing

Loading System

The loading system simulates a unidirectional truck traveling at approximately 10 mph (16 km/h). As presented in Figure 25, two rectangular loading plates measuring 15 × 7 in (381 × 177.8 mm) were connected to two actuators (MTS and Instron) through rods and positioned on the HMA overlay surface. Each loading plate simulates a dual-tire assembly contact area. The loading plates were 1 in (25 mm) apart, as presented in Figure 26. The distance between the HMA overlay edge and loading plates was 6 in (152.4 mm). The PCC joint was underneath the center of the gap between two loading plates. Each loading plate was associated with a load cell, which enabled the actuator to move the rod precisely to reach a desired load. A pivot system was required to ensure a vertical load was applied on the HMA overlay. Both actuators were connected to the same hydraulic pump and received commands from the same controller system.



Figure 25. Photo. Hydraulic loading system.

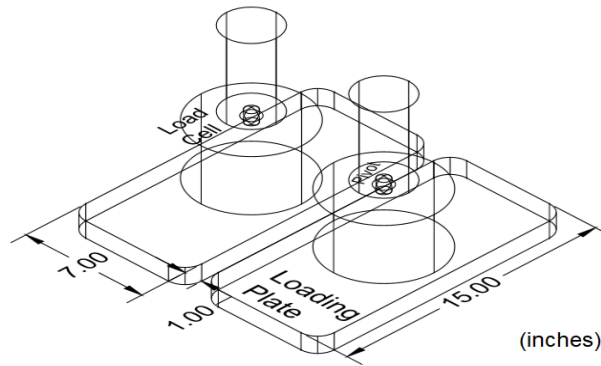


Figure 26. Diagram. Loading plate configuration.

Load Pattern

Both Mode I (opening) and Mode II (in-plane shear) fracture modes are important in reflective crack development. Thus, designing a load pattern that considers both fracture modes is imperative. As presented in Figure 27, a load cycle consists of three steps. In step 1, only the MTS actuator applied loads; in step 2, both MTS and Instron actuators applied loads; and in step 3, only the Instron actuator applied loads. Steps 1 and 3 primarily induced Mode II (in-plane shear) fracture, while step 2 primarily leads to Mode I (opening) fracture. A complete load cycle took 0.42 seconds, followed by a 0.28 second rest period until the next cycle started. Figure 28 presents an example of two continuous load cycles.

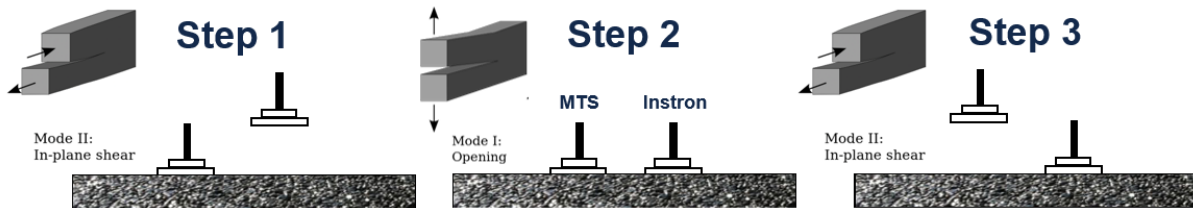


Figure 27. Diagram. Steps of load.

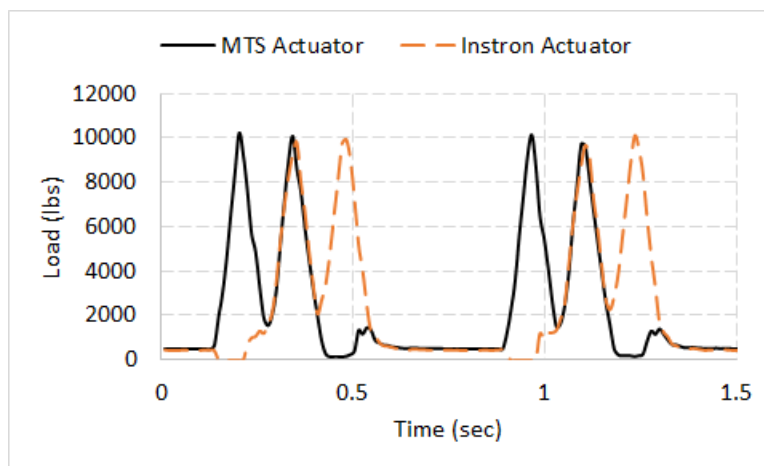


Figure 28. Chart. Load pattern.

Results

Eight slab configurations were tested, and Table 5 summarizes their lift configurations and testing temperature.

Table 5. Lift Configurations and Testing Details

Id	Surface Course	Binder Course	Testing Temperature
Non-Interstate Control	1.5" IL-9.5	0.75" IL-4.75	75.4°F (24.1°C)
Non-Interstate Alt 1	1.5" IL-9.5	1.25" IL-9.5FG	77.0°F (25.0°C)
Non-Interstate Alt 2	1.5" SMA-9.5	0.75" IL-4.75	78.1°F (25.6°C)
Non-Interstate Alt 3	1.25" IL-9.5FG	0.75" IL-4.75	79.2°F (26.2°C)
Interstate Control	1.5" IL-9.5	2.25" IL-19.0	84.0°F (28.9°C)
Interstate Alt 1	1.5" SMA-9.5	2.0" SMA-12.5	82.9°F (28.3°C)
Interstate Alt 2	2.0" SMA-12.5	2.25" IL-19.0	76.5°F (24.7°C)
Interstate Alt 3	1.5" SMA-9.5	1.5" IL-9.5	78.8°F (26.0°C)

Figure 29 compares the HMA densities for the eight slab configurations. They were measured from two cores taken close to the loading area after testing, as presented in Figure 30. All layers met IDOT's density acceptable limits requirements, except the IL-4.75 binder courses, which were lower than the control limit. Note that the IL-19.0 binder courses had significantly higher densities than other mixes.

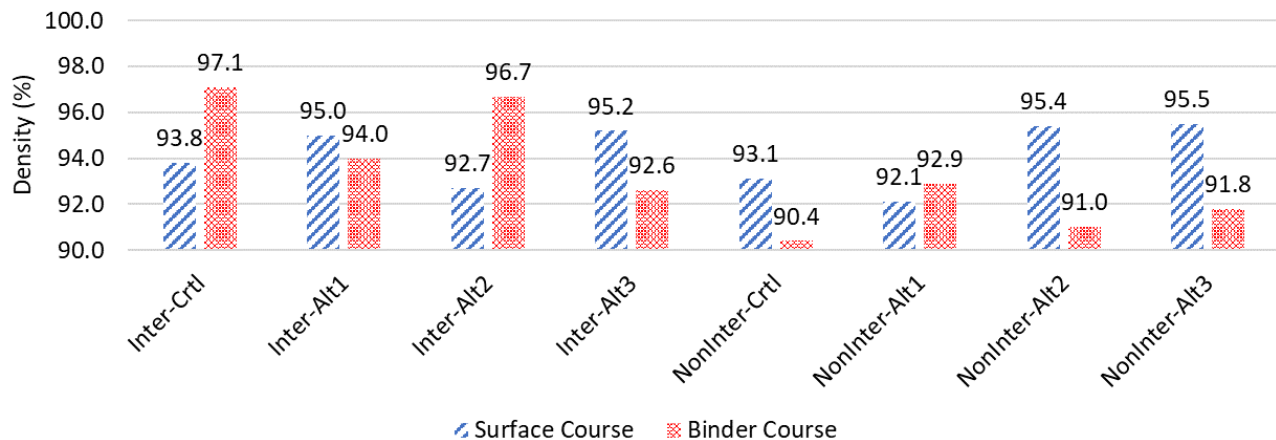


Figure 29. Chart. Densities of asphalt mixtures on test slabs.

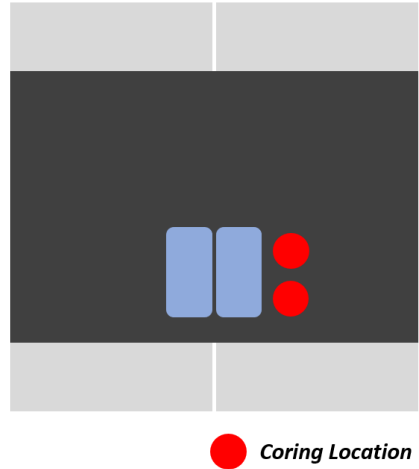


Figure 30. Graph. Coring location.

The movement of the PCC slab at the joint significantly impacts HMA overlay reflective cracking. Figure 31 compares the vertical deflections of the PCC slabs under step 2 loading (i.e., both actuators applied loads) at the start (i.e., the 1000th loading cycle) of each test. Most scenarios had similar PCC deflections, indicating that the underlying conditions of the HMA overlays were similar. Hence, differences in HMA reflective cracking behavior could be attributed primarily to HMA overlay configurations.

However, non-interstate alternative 3 had notably smaller PCC deflections, especially its left half. Also, the left and right halves of the PCC slab did not always have identical movement. The above observations were primarily because of the difference between the bottoms of the PCC slabs. Wood forms were used to cast over 3,000 lb (1,360 kg) of concrete, causing distortions in the wood that resulted in non-flat PCC bottoms. It is a reasonable assumption that under the same loading, smaller vertical movement resulted when less void existed beneath the PCC slab (i.e., better PCC–subgrade contact).

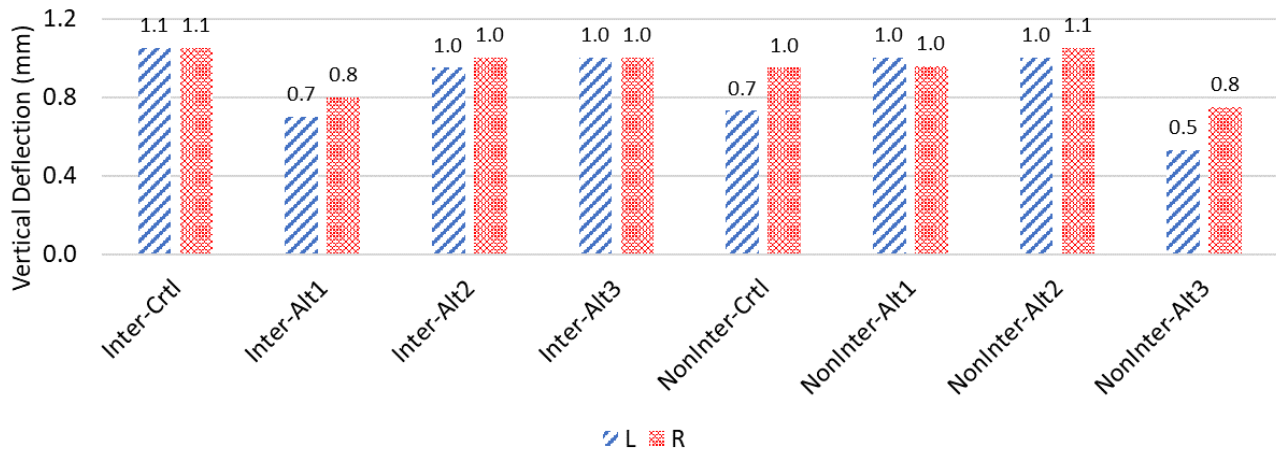


Figure 31. Chart. Vertical deflections of PCC slabs at the start of each test.

The key findings of each test slab are presented below.

Interstate Scenarios

Control

The test section consisted of a 1.5 in (38 mm) thick IL-9.5 surface course and a 2.25 in (58 mm) thick IL-19.0 binder course. As presented in Figure 32, multiple cracks were observed, and the crack paths were not well defined.



Figure 32. Photo. Interstate control scenario: cross-section after testing.

Figure 33 presents the vertical deflections observed in one loading cycle for both the left and right halves of the PCC slab at the start and end (i.e., all crack detectors broke) of the test. Because of the thick design, a relatively high load transfer efficiency was observed. Load transfer efficiency slightly decreased with crack development.

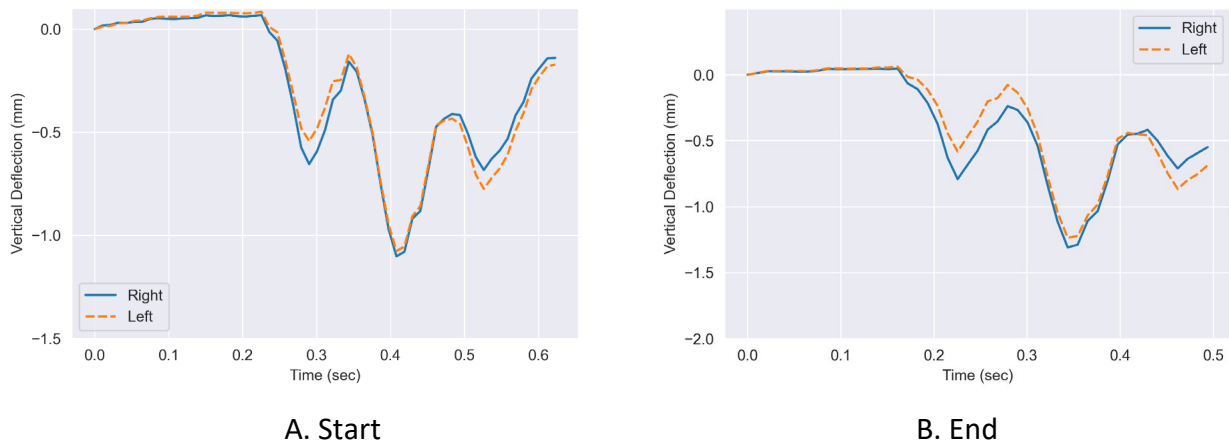


Figure 33. Chart. Interstate control scenario: vertical deflections of the PCC slab.

Four crack detectors were glued on the cross-section. Table 6 summarizes when the crack detectors broke because a crack propagated through them.

Table 6. Interstate Control Scenario: Results from Crack Detectors

Id	Distance from Bottom	Broke At (# Cycle)
CD1	3.62 in (92 mm)	5,400 th
CD2	2.60 in (66 mm)	7,000 th
CD3	1.38 in (35 mm)	9,700 th
CD4	0.63 in (16 mm)	2,900 th

Because of cyclic loading, the joint opened significantly (0.36 in [9 mm]). Because of excessive tension, as presented in Figure 34, multiple reflective cracks initiated at the bottom of the overlay and propagated upwards, and multiple cracks initiated near the surface and propagated downwards before the cracks reached CD3. With more loading, cracks started to connect, forming full-depth cracks. After the test slab was fully cracked, mild debonding was observed between the binder course and the left half of the PCC slab. No slab faulting was observed. The slab was the worst-performing scenario among all interstate cases. *The poor performance is likely due to the HMA layer's relatively low FI and comparably low surface course modulus, despite the relatively thick overlay.* It is noteworthy that the utilization of non-polymer modified surface in this specific configuration is uncommon on interstates situated in Illinois. Polymer-modified constitutes the prevailing composition of interstate surface mixtures.

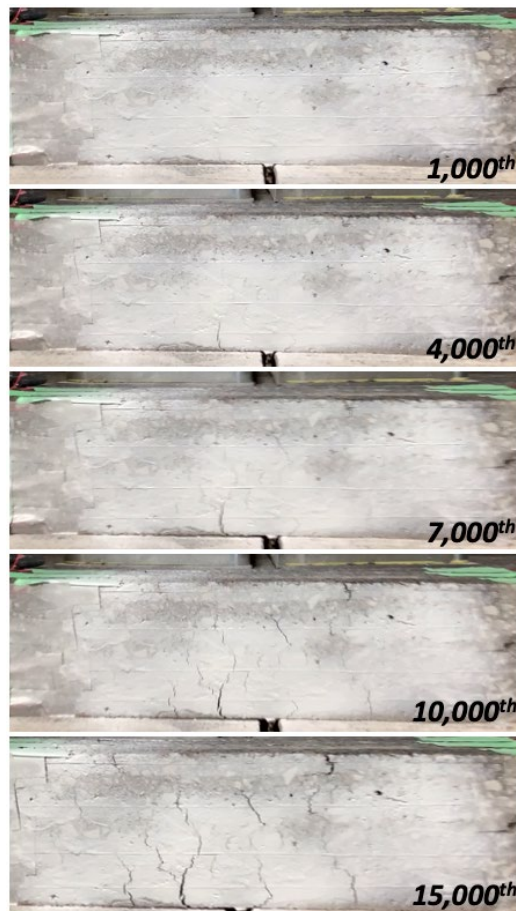


Figure 34. Photo. Interstate control scenario: crack development.

Alternative 1

The test section consisted of a 1.5 in (38 mm) thick SMA-9.5 surface course and a 2 in (51 mm) thick SMA-12.5 binder course. As presented in Figure 35, multiple cracks were observed, and the crack paths were not well defined.



Figure 35. Photo. Interstate alternative scenario 1: cross-section after testing.

Figure 36 presents the vertical deflections of the left and right halves of the PCC slab at the start and end of the test. Compared to other interstate scenarios, the slab had less vertical movement. This was likely because of a flatter PCC bottom, resulting in better PCC–subgrade contact and less void space beneath the PCC slab. The load transfer efficiency was notably smaller than in other interstate scenarios. Load transfer efficiency decreased with crack development.

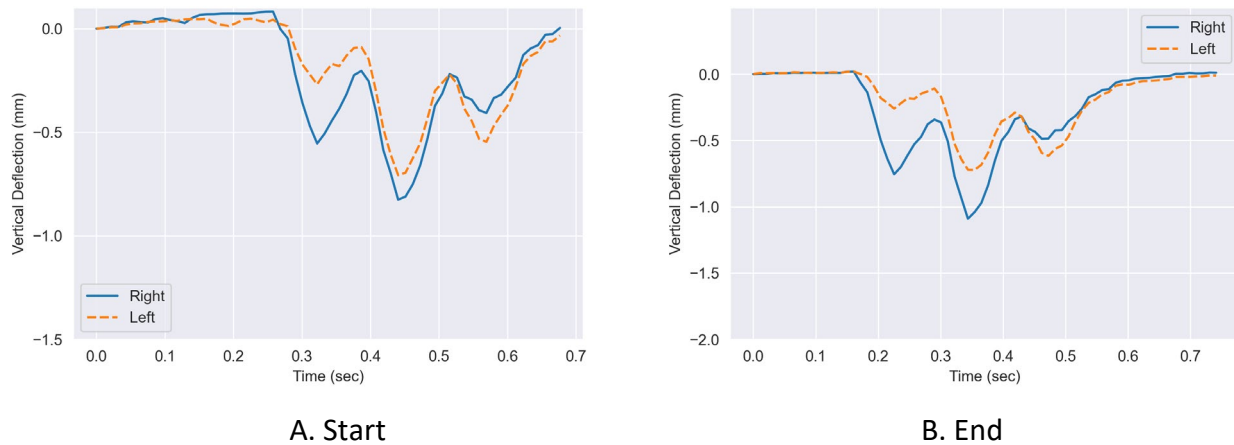


Figure 36. Chart. Interstate alternative scenario 1: vertical deflections of the PCC slab.

Four crack detectors were glued on the cross-section. Table 7 summarizes when the crack detectors broke because a crack propagated through them.

Table 7. Interstate Alternative Scenario 1: Results from Crack Detectors

Id	Distance from Bottom	Broke At (# Cycle)
CD1	3.35 in (85 mm)	14,500 th
CD2	2.64 in (67 mm)	16,200 th
CD3	1.81 in (46 mm)	13,500 th
CD4	1.18 in (30 mm)	9,500 th

Like the interstate control scenario, a significant joint opening of 0.36 in (9 mm) was observed. Because of the excessive tension, as presented in Figure 37, multiple reflective cracks initiated at the bottom of the overlay and propagated upwards. Before they reached CD2, multiple cracks initiated within the layers. Afterward, the cracks started to connect, forming full-depth cracks. No slab faulting was observed. Although the slab was 0.25 in (6.5 mm) thinner than the control scenario, it performed significantly better against reflective cracking. *The relatively good performance is likely due to the SMA's relatively high FI and the comparably high surface course modulus.*

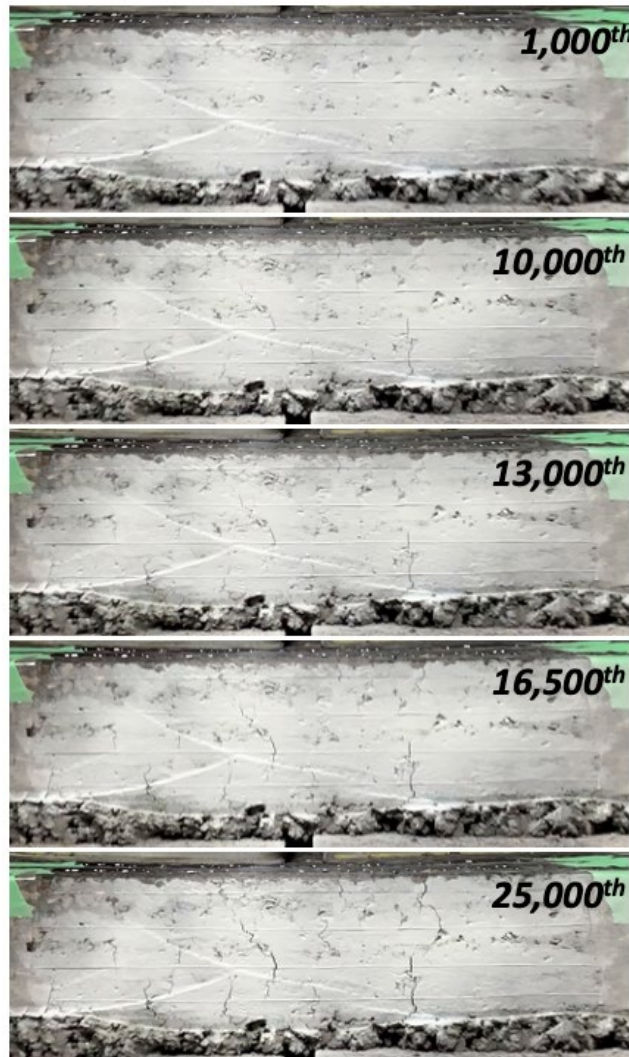


Figure 37. Photo. Interstate alternative scenario 1: crack development.

Alternative 2

The test section consisted of a 2 in (51 mm) thick SMA-12.5 surface course and a 2.25 in (58 mm) thick IL-19.0 binder course. It was the thickest overlay scenario among all slabs. It differed from the control scenario by surface course only. A well-defined reflective crack was observed, as presented in Figure 38.



Figure 38. Photo. Interstate alternative scenario 2: cross-section after testing.

Figure 39 presents the vertical deflections of the left and right halves of the PCC slab at the start and end of the test. Because of the relatively thick overlay design, high load transfer efficiency was observed. Load transfer efficiency decreased with crack development. Compared to other tests, significantly more deflections were seen at the end of the test than at the start. This could be due to the wide crack.

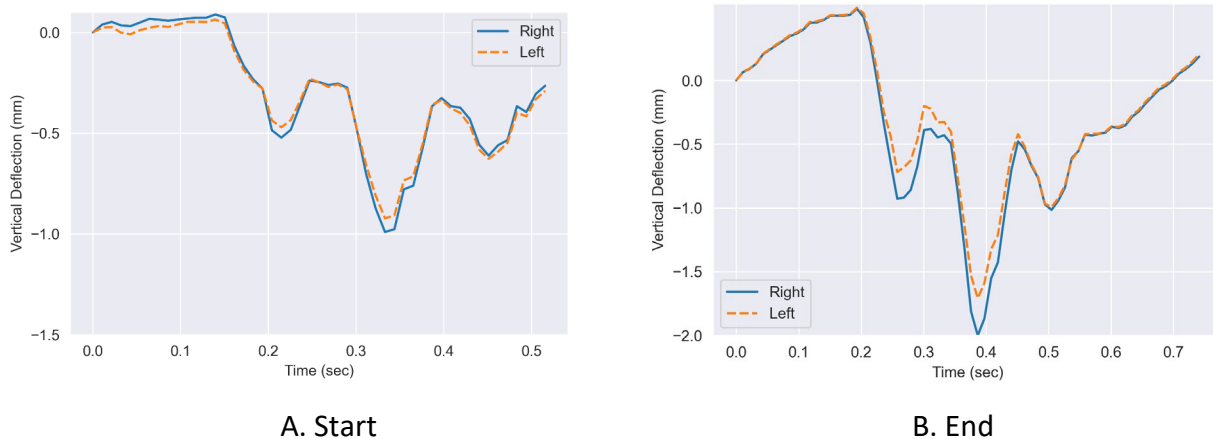


Figure 39. Chart. Interstate alternative scenario 2: vertical deflections of the PCC slab.

Five crack detectors were glued on the cross-section. Table 8 summarizes when the crack detectors broke because a crack propagated through them.

Table 8. Interstate Alternative Scenario 2: Results from Crack Detectors

Id	Distance from Bottom	Broke At (# Cycle)
CD1	3.66 in (93 mm)	23,700 th
CD2	2.95 in (75 mm)	23,100 th
CD3	2.24 in (57 mm)	22,500 th
CD4	1.26 in (32 mm)	22,200 th
CD5	0.39 in (10 mm)	18,300 th

Although the joint opened significantly (0.36 in [10 mm]), unlike other interstate scenarios, a primary reflective crack initiated at the bottom of the overlay and propagated upwards (Figure 40). The crack initiated about 1.3 in (32 mm) right of the joint. The crack path did not follow a vertical trajectory, indicating mixed-mode fracture. Significant debonding occurred when the crack reached the surface–binder interface and stopped propagating. Shortly after, multiple hairline cracks were observed within the surface layer, causing CD1 and CD2 to break. The primary crack started to propagate upwards again after another few thousand loading cycles. A slight offset toward the right was observed at the surface–binder interface. No slab faulting was observed. *The test slab was the best-performing scenario among interstate cases. The overlay thickness and high FI SMA surface contributed to its superior performance against reflective cracking.*

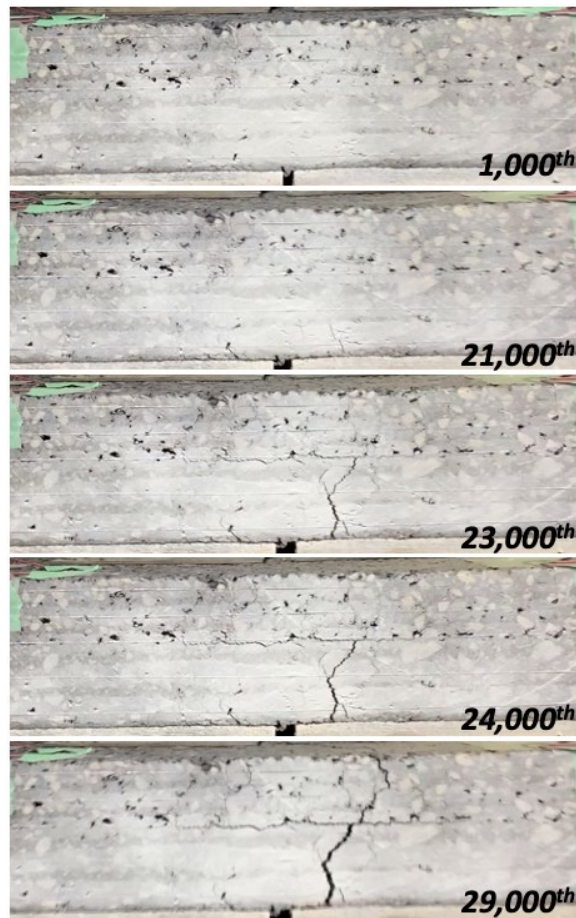


Figure 40. Photo. Interstate alternative scenario 2: crack development.

Alternative 3

The test section consisted of a 1.5 in (38 mm) thick SMA-9.5 surface course and a 1.5 in (38 mm) thick IL-9.5 binder course. It was the thinnest interstate scenario. As presented in Figure 41, multiple cracks were observed, and the crack paths were not well defined.



Figure 41. Photo. Interstate alternative scenario 3: cross-section after testing.

Figure 42 presents the vertical deflections of the left and right halves of the PCC slab at the start and end of the test. Because it was the thinnest design among all interstate scenarios, the load transfer efficiency was notably smaller than others. Load transfer efficiency further decreased with crack development. Significantly more deflection was noted at the end of the test than at the start.

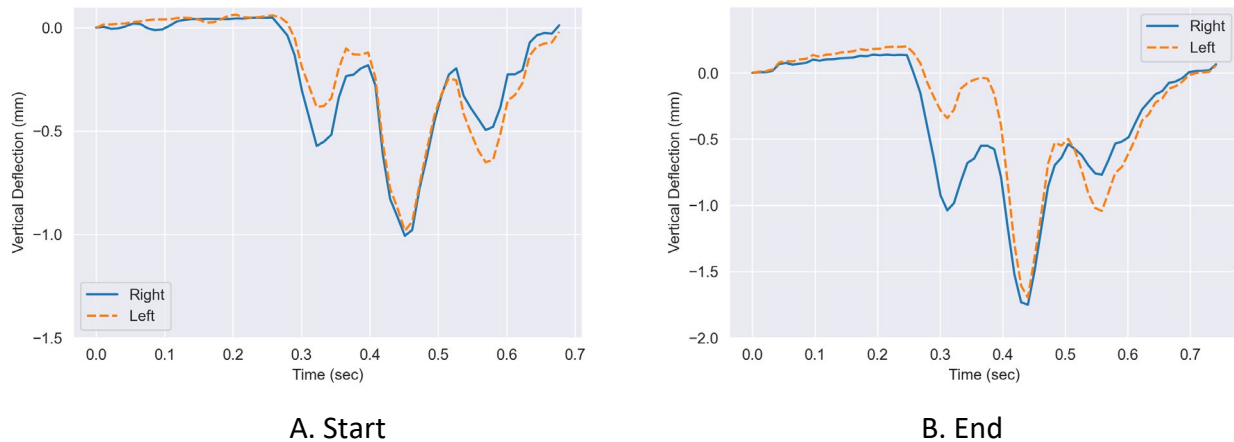


Figure 42. Photo. Interstate alternative scenario 3: vertical deflections of the PCC slab.

Four crack detectors were glued on the cross-section. Table 9 summarizes when the crack detectors broke because a crack propagated through them.

Table 9. Interstate Alternative Scenario 3: Results from Crack Detectors

Id	Distance from Bottom	Broke At (# Cycle)
CD1	2.68 in (68 mm)	9,600 th
CD2	2.05 in (52 mm)	9,200 th
CD3	1.50 in (38 mm)	9,900 th
CD4	0.79 in (20 mm)	10,200 th

The joint opened significantly (0.32 in [8 mm]). Because of the excessive tension, as presented in Figure 43, multiple cracks formed within the overlay. Moderate debonding was observed between the binder course and the left part of the PCC slab. Moreover, significant debonding occurred when the cracks reached the surface–binder interface and stopped propagating. *Because it was the thinnest design among all interstate scenarios and had a low FI binder course, the test slab showed poor performance against reflective cracking. However, note that although the test slab was 0.5 in (12.7 mm) thinner than the control scenario, the high FI SMA surface course made the test slab slightly outperform the control.*

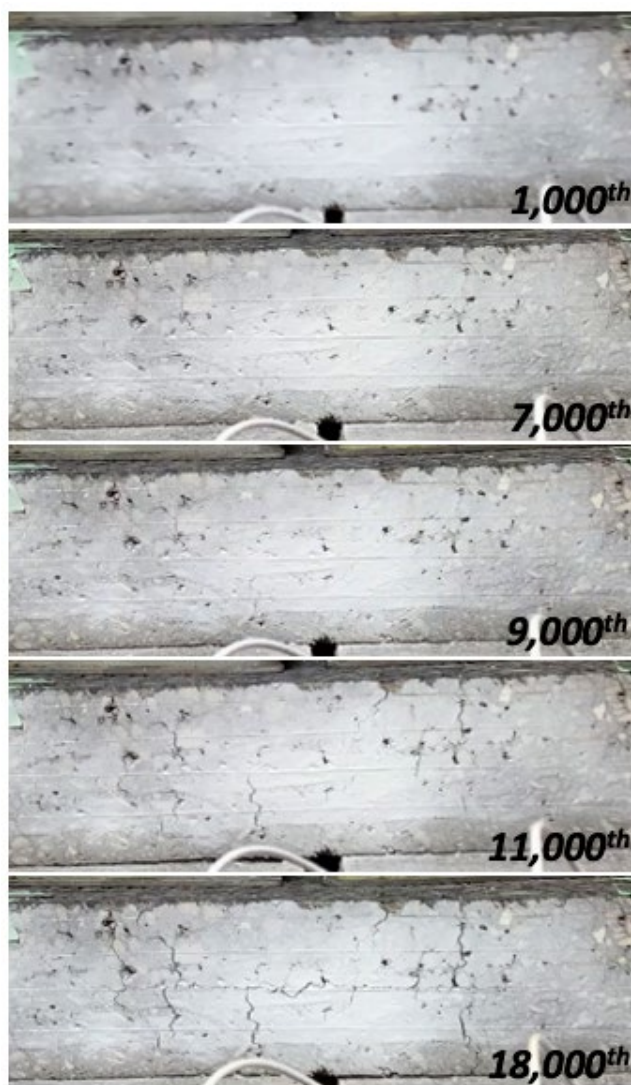


Figure 43. Photo. Interstate alternative scenario 3: crack development.

Non-Interstate Scenarios

Control

The test section consisted of a 1.5 in (38 mm) thick IL-9.5 surface course and a 0.75 in (19 mm) thick IL-4.75 binder course. A well-defined reflective crack was observed, as presented in Figure 44.



Figure 44. Photo. Non-interstate control scenario: cross-section after testing.

Figure 45 presents the vertical deflections of the left and right halves of the PCC slab at the start and end of the test. Compared to other tests, the left half of the PCC slab had less vertical movement. This was likely because of a flatter PCC bottom, resulting in better PCC–subgrade contact and less void space beneath the concrete slab. Because of the thinner structure, load transfer efficiency was notably smaller than in interstate scenarios. Load transfer efficiency further decreased with crack development.

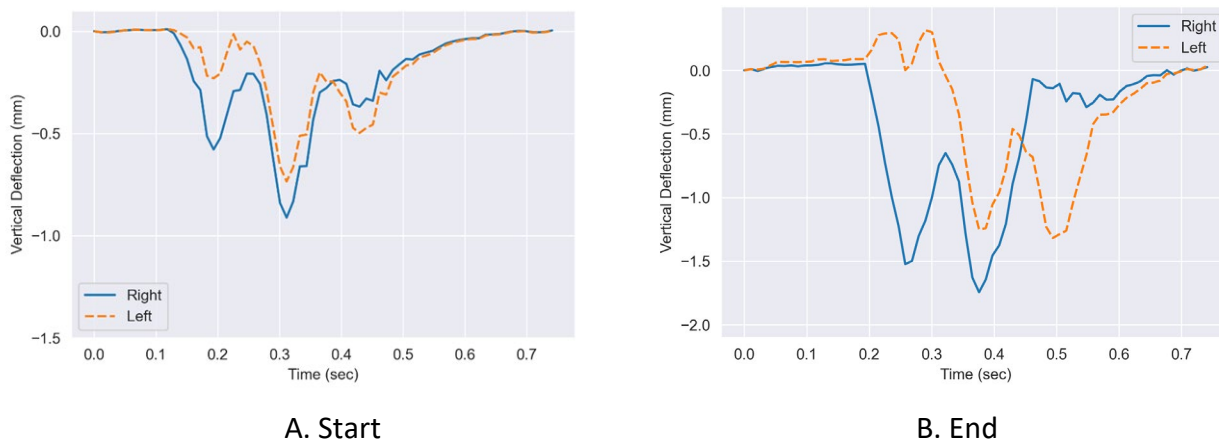


Figure 45. Chart. Non-interstate control scenario: vertical deflections of the PCC slab.

Four crack detectors were glued on the cross-section. Table 10 summarizes when the crack detectors broke because of crack propagation.

Table 10. Non-Interstate Control Scenario: Results from Crack Detectors

Id	Distance from Bottom	Broke At (# Cycle)
CD1	1.85 in (47 mm)	14,600 th
CD2	1.26 in (32 mm)	14,500 th
CD3	0.75 in (19 mm)	13,900 th
CD4	0.43 in (11 mm)	10,700 th

Figure 46 presents images of the overlay cross-section at various loading cycles. Unfortunately, the green tape used to protect the crack detector wires blocked the camera from recording the crack

development. The crack's path was much further from the joint than in other scenarios. However, the images are valuable in visualizing the debonding phenomenon and material separation due to crack development.

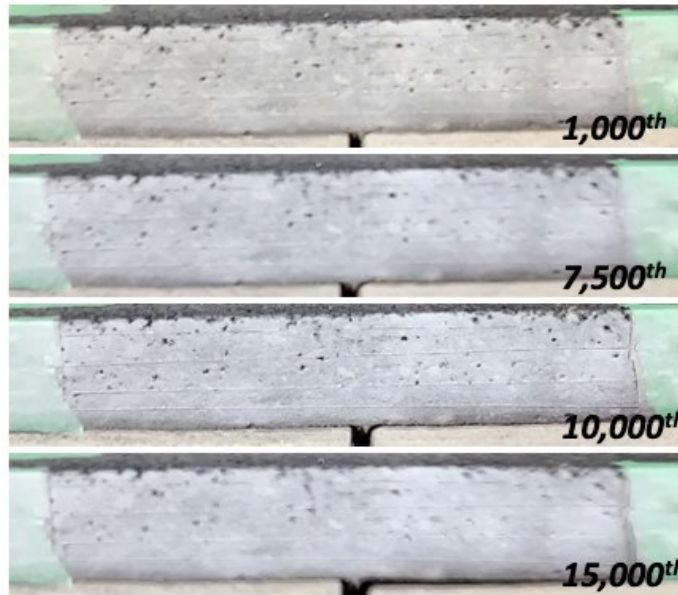


Figure 46. Photo. Non-Interstate control scenario: crack development.

The reflective crack initiated at the bottom of the overlay and propagated upwards. It followed a roughly vertical trajectory. After roughly 8,000 loading cycles, significant debonding occurred between the binder course and the right half of the PCC slab. Shortly after significant debonding occurred, the crack initiated near the end of the debonding area (i.e., about 5.5 in [140 mm] right of the joint). The crack propagated on average 1.57 in (40 mm) per 1,000 loading cycles in the surface course, while the propagation rate in the binder course was 0.15 in (3.8 mm) per 1,000 loading cycles. A less significant joint opening (0.24 in [6 mm]) was observed. Significant slab faulting was seen on the same side of the crack. *Because the surface course had relatively low modulus and low FI, the test slab was the worst-performing scenario among all non-interstate scenarios.*

Alternative 1

The test section consisted of a 1.5 in (38 mm) thick IL-9.5 surface course and a 1.25 in (38 mm) thick IL-9.5FG binder course. It differed from the control scenario by binder course only. Multiple well-defined reflective cracks were observed, as presented in Figure 47.



Figure 47. Photo. Non-interstate alternative scenario 1: cross-section after testing.

Figure 48 presents the vertical deflections of the left and right halves of the PCC slab at the start and end of the test. Because the test section was 0.5 in (12.7 mm) thicker than the non-interstate control scenario, the load transfer efficiency was slightly higher at the start of the test. Load transfer efficiency decreased substantially with crack development.

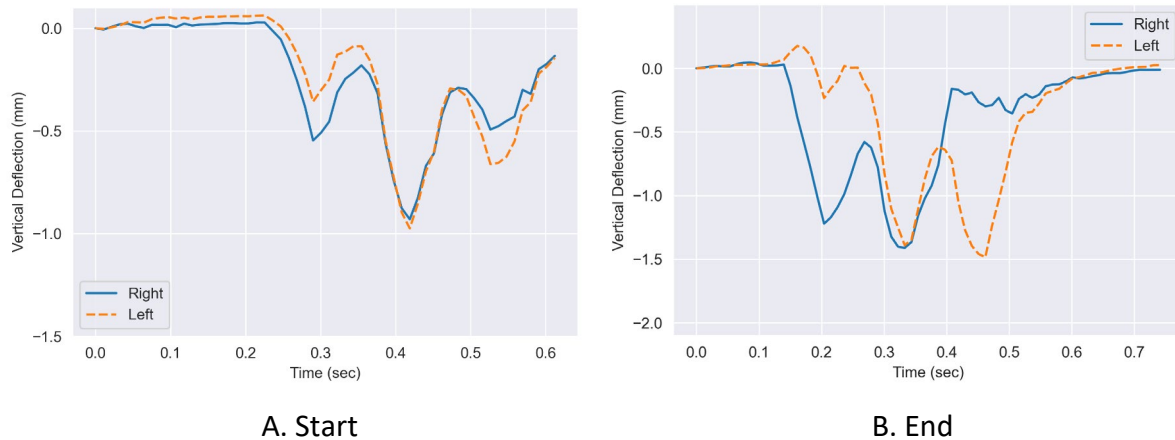


Figure 48. Chart. Non-interstate alternative scenario 1: vertical deflections of the PCC slab.

Four crack detectors were glued on the cross-section. Table 11 summarizes when the crack detectors broke because of crack propagation.

Table 11. Non-Interstate Alternative Scenario 1: Results from Crack Detectors

Id	Distance from Bottom	Broke At (# Cycle)
CD1	2.36 in (60 mm)	7,100 th
CD2	1.73 in (44 mm)	6,000 th
CD3	1.19 in (30 mm)	14,600 th
CD4	0.31 in (8 mm)	9,900 th

After roughly 6,000 loading cycles, significant debonding occurred between the binder course and the right half of the PCC slab. Significant slab faulting was also noted. Shortly after, as presented in Figure 49, two reflective cracks initiated near the surface and propagated downwards. Significant debonding occurred when the cracks reached the surface–binder interface, and the crack stopped propagating. Then, multiple cracks initiated at the bottom of the overlay near the end of the debonding area and propagated upwards. Most cracks stopped propagating near the surface–binder interface except for one crack, the farthest from the joint. After testing, a moderate joint opening of 0.2 in (5 mm) was observed. Although the binder course of the test slab was 0.5 in (12.7 mm) thicker than the control scenario, its relatively low asphalt content and low FI resulted in lower performance. Despite a relatively thicker structure, the test slab had a similar number of cycles to failure as the control scenario. *This observation suggested that the IL-4.75 sand mix, as a stress-absorbing material, efficiently enhanced the overlay’s resistance against reflective cracking.*

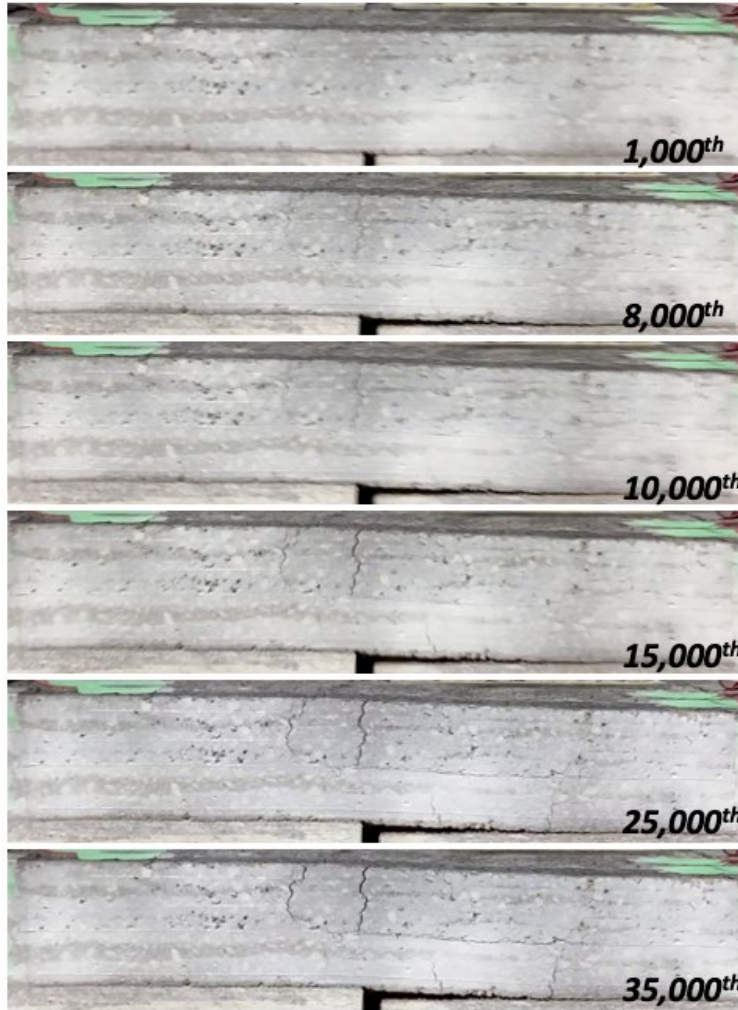


Figure 49. Photo. Non-interstate alternative scenario 1: crack development.

Alternative 2

The test section consisted of a 1.5 in (38 mm) thick SMA-9.5 surface course and a 0.75 in (19 mm) thick IL-4.75 binder course. It differed from the control by surface course only. A well-defined reflective crack was observed, as presented in Figure 50.



Figure 50. Photo. Non-interstate alternative scenario 2: cross-section after testing.

Figure 51 presents the vertical deflections of the left and right halves of the PCC slab at the start and end of the test. Because of their similar thicknesses, the load transfer efficiency of the test slab was close to other non-interstate scenarios. Load transfer efficiency reduced substantially with crack development.

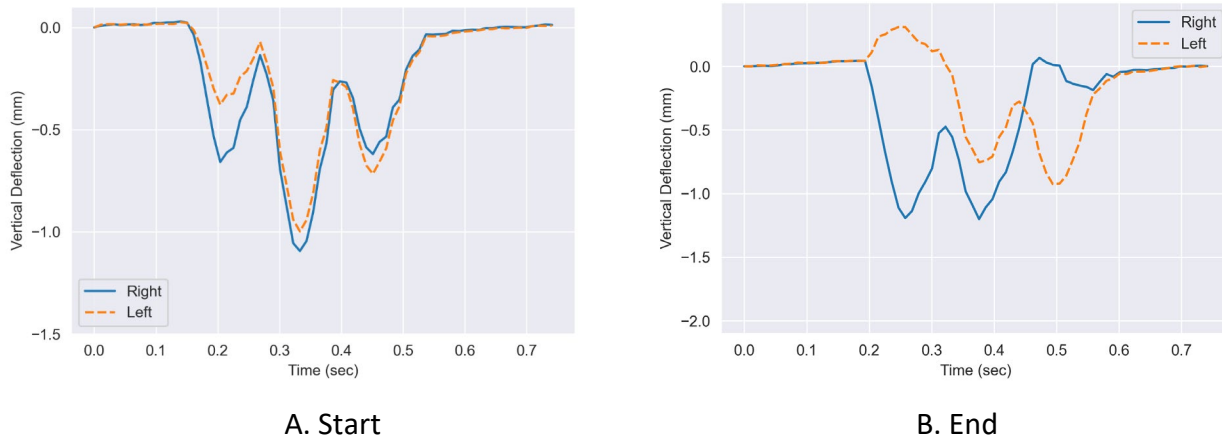


Figure 51. Chart. Non-interstate alternative scenario 2: vertical deflections of the PCC slab.

Four crack detectors were glued on the cross-section. Table 12 summarizes when the crack detectors broke because a crack propagated through them.

Table 12. Non-Interstate Alternative Scenario 2: Results from Crack Detectors

Id	Distance from Bottom	Broke At (# Cycle)
CD1	1.97 in (50 mm)	19,950 th
CD2	1.42 in (36 mm)	61,650 th
CD3	0.75 in (19 mm)	67,100 th
CD4	0.39 in (10 mm)	69,850 th

After roughly 17,000 loading cycles, significant debonding occurred between the binder course and the right half of the PCC slab. Shortly after, as presented in Figure 52, the reflective crack initiated near the surface and propagated downwards. The crack propagated at an angle tilted away from a purely vertical trajectory, indicating mixed-mode fracture. The crack did not initiate directly on top of the joint. Instead, it initiated about 1.5 in (38 mm) left of the joint and, as expected, propagated toward the joint. The crack propagated on average 0.25 in (6.4 mm) per 1,000 loading cycles in the surface course, while the crack propagation rate in the binder course was 0.12 in (3 mm) per 1,000 loading cycles. A moderate joint opening of 0.2 in (5 mm) was observed. The test slab performed well against reflective cracking because of the reflective-controlling IL-4.75 sand mix binder course and the high FI, high modulus SMA surface course. *Although the test slab had the same thickness and binder course as the control scenario, the premium SMA-9.5 surface course significantly boosted the performance against reflective cracking.*

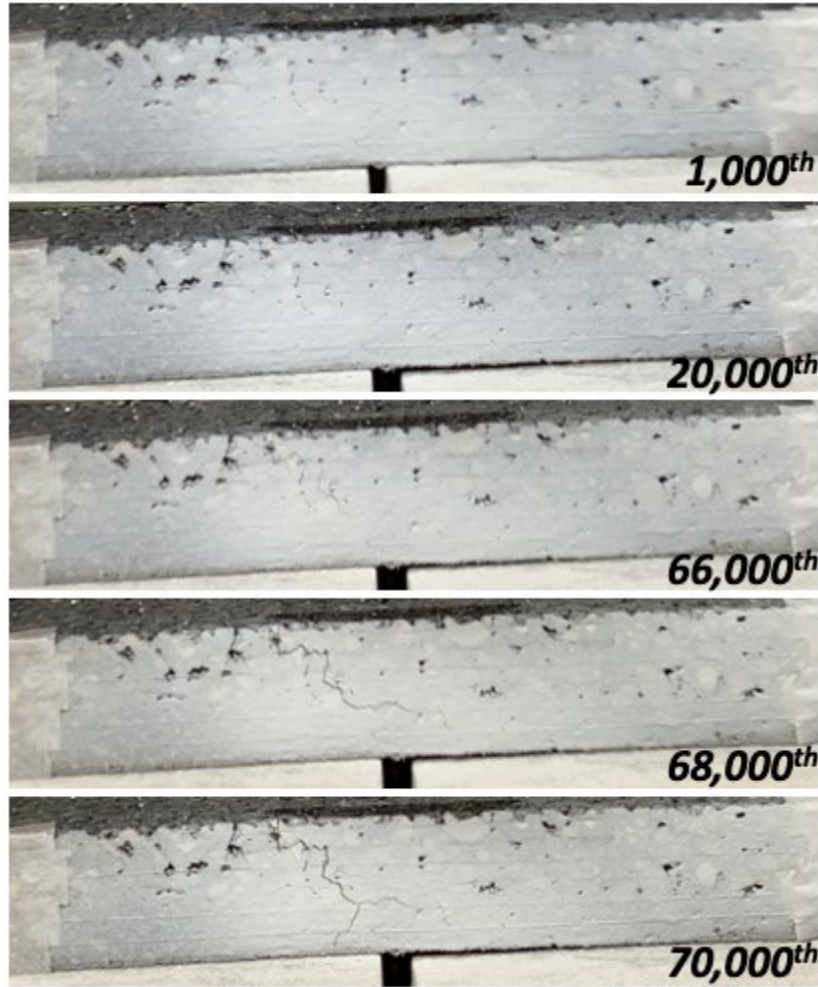


Figure 52. Photo. Non-interstate alternative scenario 2: crack development.

Alternative 3

The test section consisted of a 1.25 in (33 mm) thick IL-9.5FG surface course and a 0.75 in (19 mm) thick IL-4.75 binder course. It was the thinnest scenario among all slabs. In addition, it differed from the control and alternative 2 by surface course only. A well-defined reflective crack was observed, as presented in Figure 53.



Figure 53. Photo. Non-interstate alternative scenario 3: cross-section after testing.

Figure 54 presents the vertical deflections of the left and right halves of the PCC slab at the start and end of the test. Compared to other non-interstate scenarios, the slab had notably smaller vertical movement, especially for the left half. This was likely because of a flatter PCC bottom, resulting in better PCC–subgrade contact and fewer voids beneath the concrete slab. Because it was the thinnest design among all non-interstate scenarios, the load transfer efficiency was smaller than the others. Load transfer efficiency further decreased with crack development.

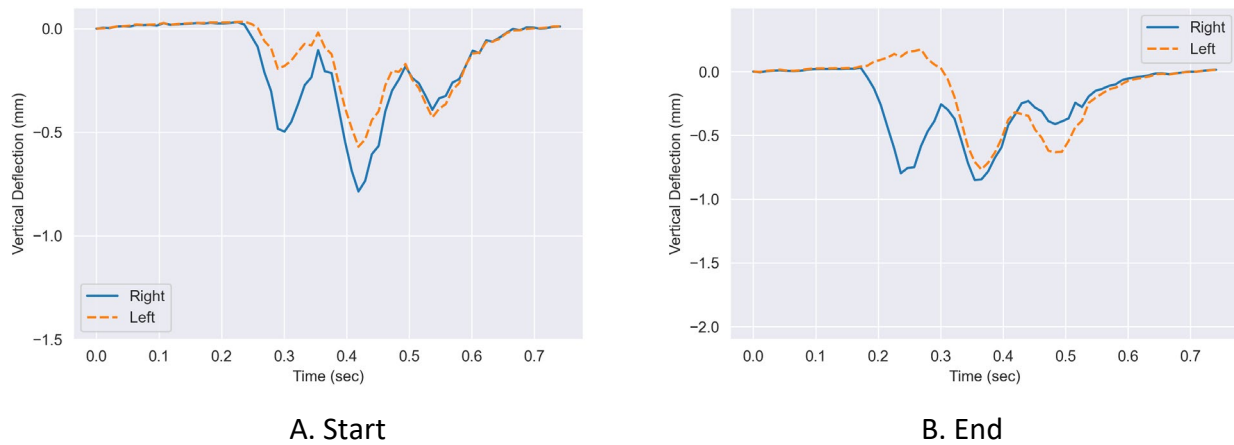


Figure 54. Chart. Non-interstate alternative scenario 3: vertical deflections of the PCC slab.

Four crack detectors were glued on the cross-section. Table 13 summarizes when the crack detectors broke because a crack propagated through. CD1 broke earlier than CD2 because of a hairline crack, which initiated near the surface on the left of the joint.

Table 13. Non-Interstate Alternative Scenario 3: Results from Crack Detectors

ID	Distance from Bottom	Broke At (# Cycle)
CD1	1.81 in (46 mm)	103,100 th
CD2	1.22 in (31 mm)	111,500 th
CD3	0.83 in (21 mm)	92,600 th
CD4	0.47 in (12 mm)	62,500 th

As presented in Figure 55, the reflective crack initiated at the bottom of the overlay and propagated upwards. Moderate debonding between the binder course and the left half of the PCC slab was seen at the time of crack initiation. The crack initiated about 2.2 in (55 mm) right of the joint, on the opposite side of the debonding area. The debonding became more severe with more loading cycles. Meanwhile, the crack propagated slowly until significant debonding was observed. After testing, a moderate joint opening of 0.24 in (6 mm) was observed. Significant slab faulting was also noted. Although the test slab was the thinnest among all scenarios, it had the highest number of cycles to failure. It took over 60,000 loading cycles to initiate the crack, while the crack propagation speed in the surface course was relatively fast because of its low FI. *Besides the stress-absorbing sand mix*

binder course and the high modulus surface course, the superior performance was also due to the significantly smaller vertical movement of the PCC slab, leading to the delayed occurrence of debonding.

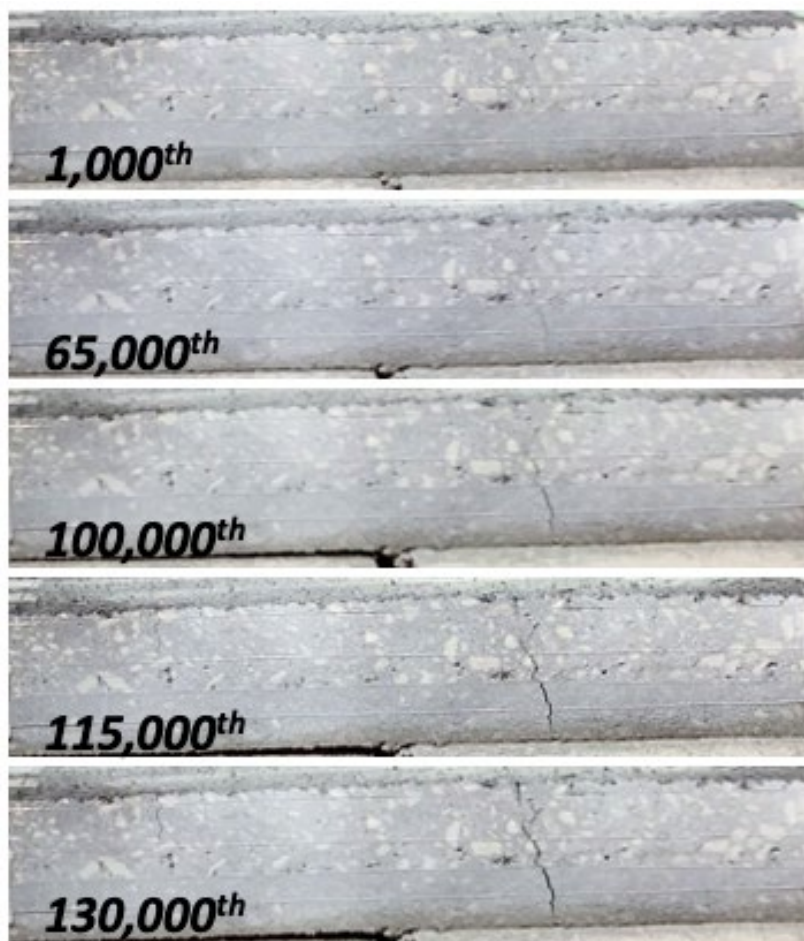


Figure 55. Photo. Non-interstate alternative scenario 3: crack development.

DISCUSSION

Testing results were analyzed to identify the factors that significantly affect the HMA overlay's performance to abate reflective cracking. As shown in Table 14, because non-interstate and interstate scenarios had different cracking mechanisms, they were evaluated separately to ensure meaningful comparison.

Figure 56 provides a ranking of non-interstate scenarios based on their number of cycles to failure. Alternatives 2 and 3 were considered the top performers (colored in blue). They both had two polymer-modified asphalt layers, a stress-absorbing, high asphalt content, high FI IL-4.75 binder course, and a high modulus surface course. Note that although alternative 3 had the largest number of cycles to failure, it cannot be concluded as the best-performing scenario because of its significantly smaller PCC vertical movement, leading to the delayed occurrence of debonding. Control and

alternative 1 were the worst-performing non-interstate scenarios (colored in red), resulting from the low FI and low modulus surface course.

Table 14. Summary of Large-Scale Testing Results

ID	Primary Mechanism	Cracking Pattern	# Cycles to Failure
Non-Interstate Ctrl	Significant debonding and slab faulting	Single bottom-up crack	14,600
Non-Interstate Alt 1		Top-down cracks in surface course and bottom-up cracks in binder course	14,600
Non-Interstate Alt 2		Single top-down crack	69,850
Non-Interstate Alt 3		Single bottom-up crack	111,500
Interstate Ctrl	Excessive joint opening	Multiple non-well-defined cracks	9,700
Interstate Alt 1		Multiple non-well-defined cracks	16,200
Interstate Alt 2		A primary bottom-up crack and multiple non-well-defined cracks	23,700
Interstate Alt 3		Multiple non-well-defined cracks	10,200

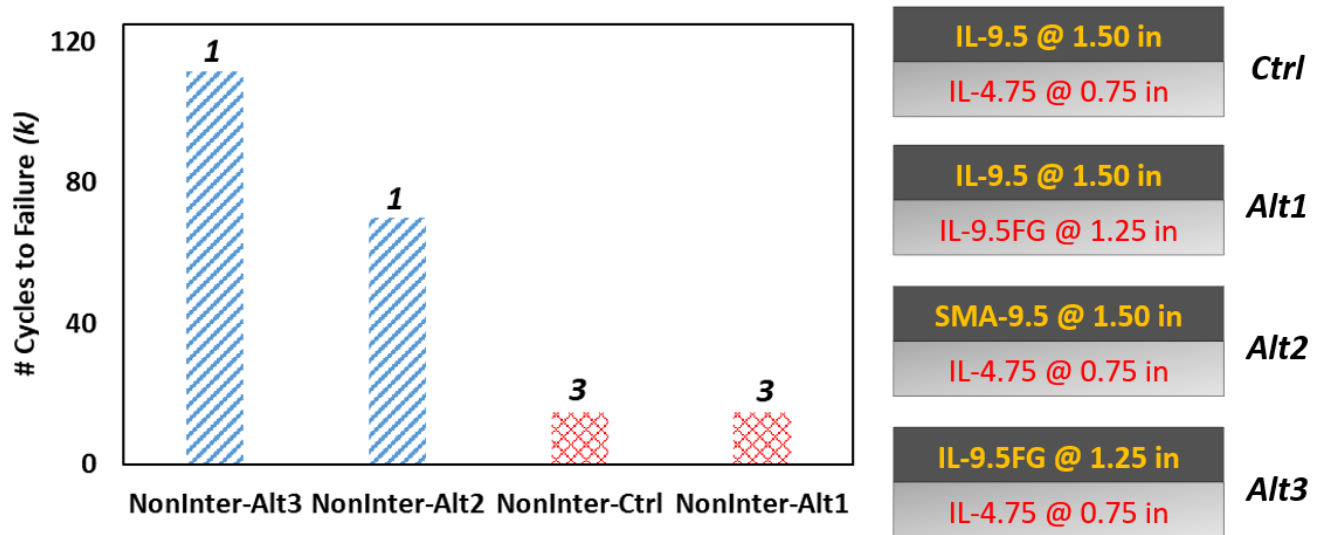


Figure 56. Chart. Number of cycles to failure and ranking of non-interstate scenarios.

Figure 57 presents the ranking of interstate scenarios. Alternative 2, which had the thickest structure and a high FI SMA surface course, was the best-performing overlay configuration. Alternative 1, which was 0.75 in (19 mm) thinner than alternative 2 and had two high FI SMA courses, was ranked second. The control and alternative 3 were the worst-performing interstate scenarios, resulting from the low FI mixes and having the thinnest design, respectively.

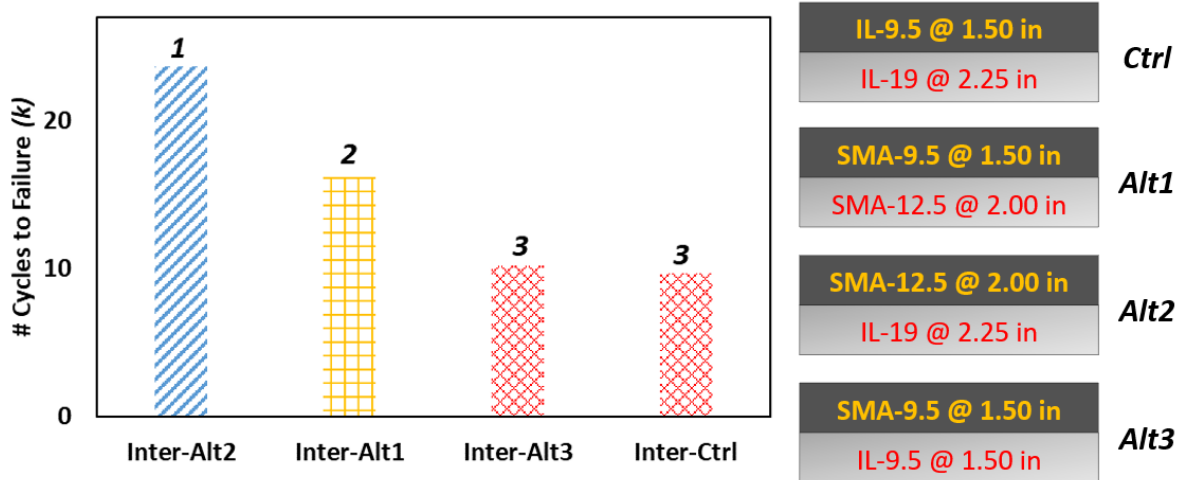


Figure 57. Chart. Number of cycles to failure and ranking of interstate scenarios.

The following sections discuss the factors that affect an overlay's reflective cracking behavior.

Effect of Joint Opening

Interstate scenarios had 54% wider PCC joint openings during testing than non-interstate scenarios. Hence, excessive tension-induced cracks appeared within the overlays in the early stages, making interstate scenarios fail relatively quickly despite their thick structures. As presented in Figure 58, a larger NMAS of binder courses in interstate scenarios strongly correlates with more joint openings. A possible explanation is that a larger NMAS (i.e., coarser aggregates) led to less HMA–PCC contact area. Under the same tack-coat application rate, the bonding efficiencies were smaller for binder courses with a larger NMAS. Note that a fine-graded 3/8 in (9.5 mm) mix substantially improved the bonding efficiency compared to a coarse-graded mix.

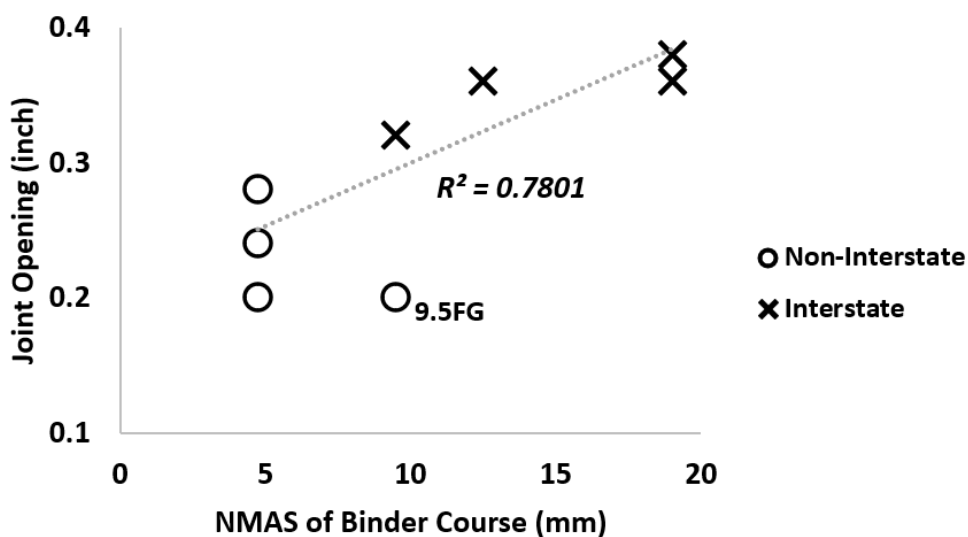


Figure 58. Chart. Relationship between joint opening and NMAS of binder course.

Effect of Debonding

Debonding at the Binder–PCC Interface

Debonding had a significant impact on reflective cracking behavior. Figure 59 demonstrates that thicker overlays (i.e., interstate scenarios) were less likely to experience severe debonding at the binder–PCC interface. This is because a thicker HMA overlay provides better bridging to accommodate the PCC slabs' movement across the joint, resulting in a higher load transfer efficiency (Figure 60). Moreover, severe debonding was mainly associated with significant slab faulting, which was more likely to occur in thinner overlays.

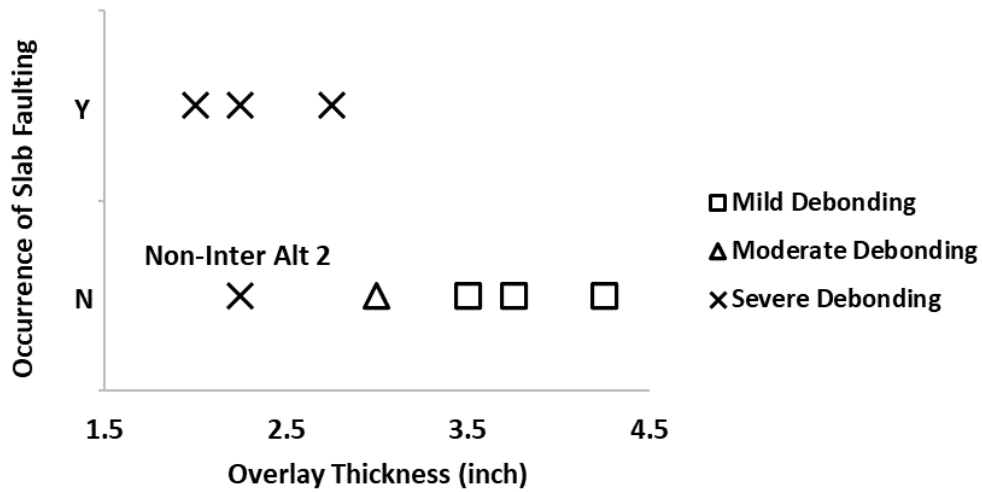


Figure 59. Chart. Relationship between overlay thickness and occurrence of debonding and slab faulting.

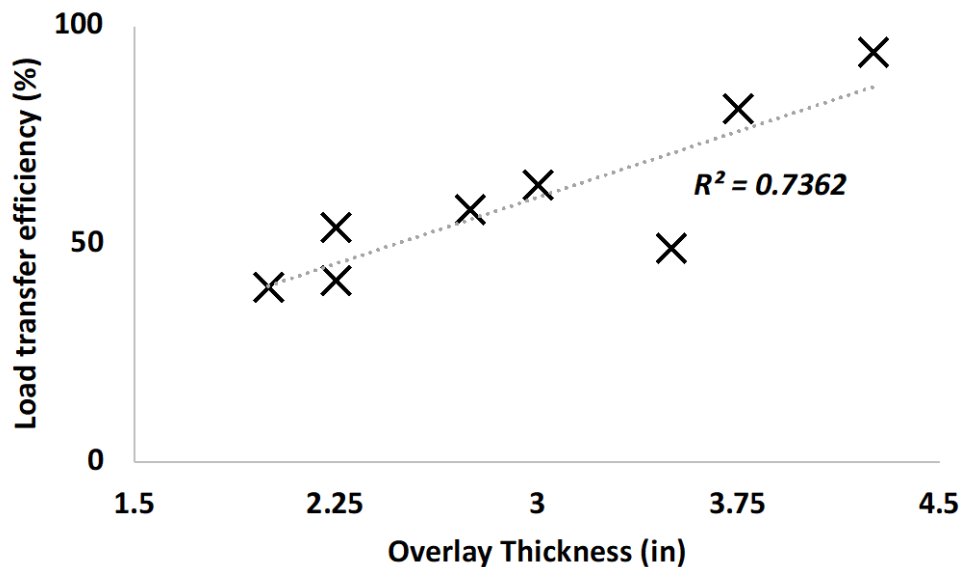


Figure 60. Chart. Relationship between total overlay thickness and load transfer efficiency.

Figure 61 illustrates that debonding strongly correlated with reflective crack initiation in non-interstate scenarios. As seen in the non-interstate control and alternatives 1 and 2, a bottom-up reflective crack often initiated near the end of the debonding area, where bending stress is intensified the most. In contrast, because of a cantilever-beam-like mechanism, a top-down crack was often initiated on the opposite side of the debonding region with respect to the joint. However, in non-interstate alternative 3, the bottom-up reflective crack initiated on the right of the joint while significant debonding occurred on the left. A possible explanation is that the left slab had a significantly smaller deflection than the right one and other non-interstate scenarios (Figure 31), leading to insufficient stress intensity to initiate a crack in the debonding area. Note that although the crack initiated when moderate debonding occurred, it propagated at a low rate until significant debonding was observed.

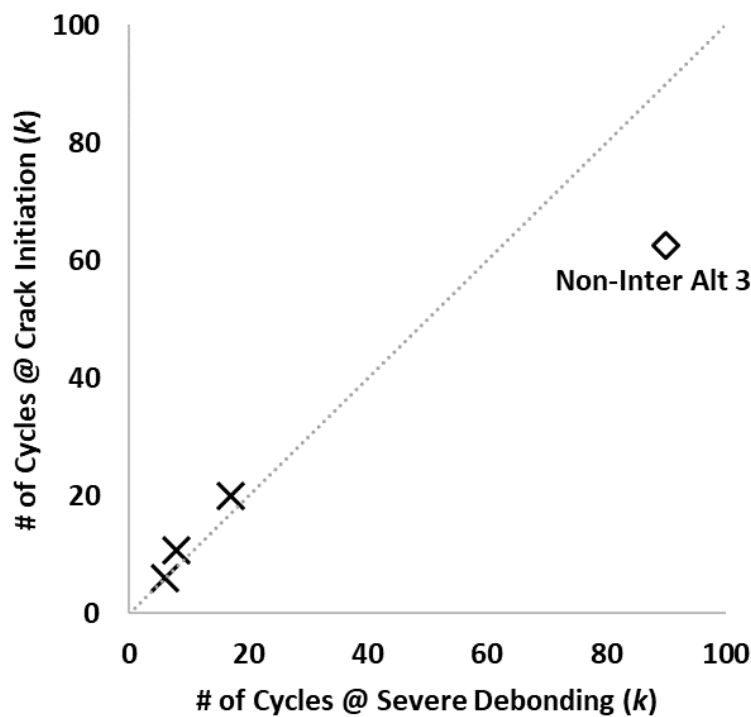


Figure 61. Chart. Relationship between crack initiation and severe debonding in non-interstate scenarios.

Debonding at the Surface–Binder Interface

As presented in Figure 62, debonding at the surface–binder interface was more likely if one of the HMA layers was polymer-modified while the other was not. Because of the debonding, reflective cracks stopped propagating at the interface. However, they would “re-initiate” at the interface. Slight offsets to the previous crack paths were often observed.

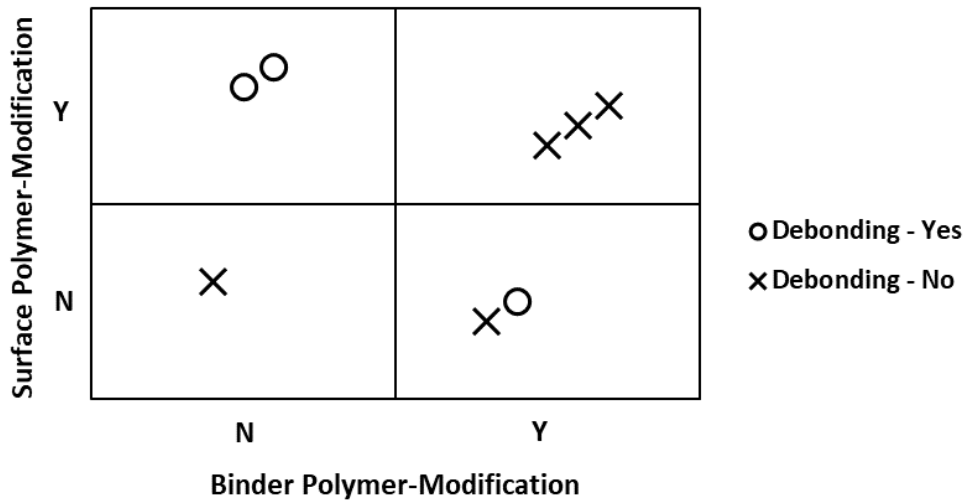


Figure 62. Chart. Relationship between polymer-modification and debonding at the surface–binder interface.

Effect of HMA Modulus and Flexibility Index

Large-scale testing results were correlated with HMA modulus and FI to investigate the effect of material properties on overlay performance. Figure 63 illustrates that FI significantly impacted overlay cracking potential. When both binder and surface courses had acceptable FI (i.e., greater than 8), the overlays were less prone to reflective cracking. In contrast, when both courses failed the FI criterion, the overlays showed poor performance against reflective cracking.

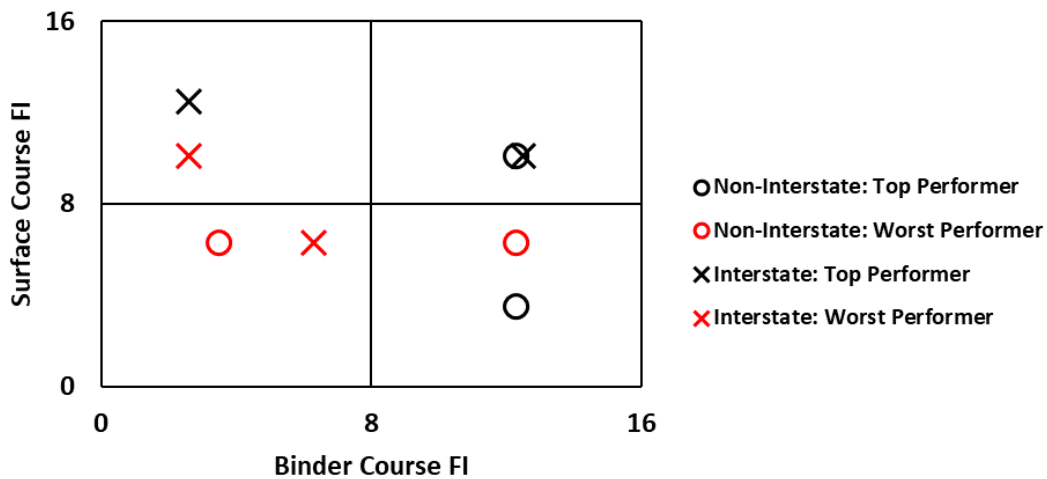


Figure 63. Chart. Effect of FI on overlay performance against reflective cracking.

Figure 64 demonstrates that modulus had a substantial effect on overlay performance. An overlay with a higher modulus surface course and a lower modulus binder course was less prone to reflective cracking. Although interstate alternative 2 had a low modulus surface course and high modulus

binder course, its premium SMA surface and relatively thick design (4.25 in [107.9 mm]) that provided bridging contributed to its superior performance against reflective cracking.

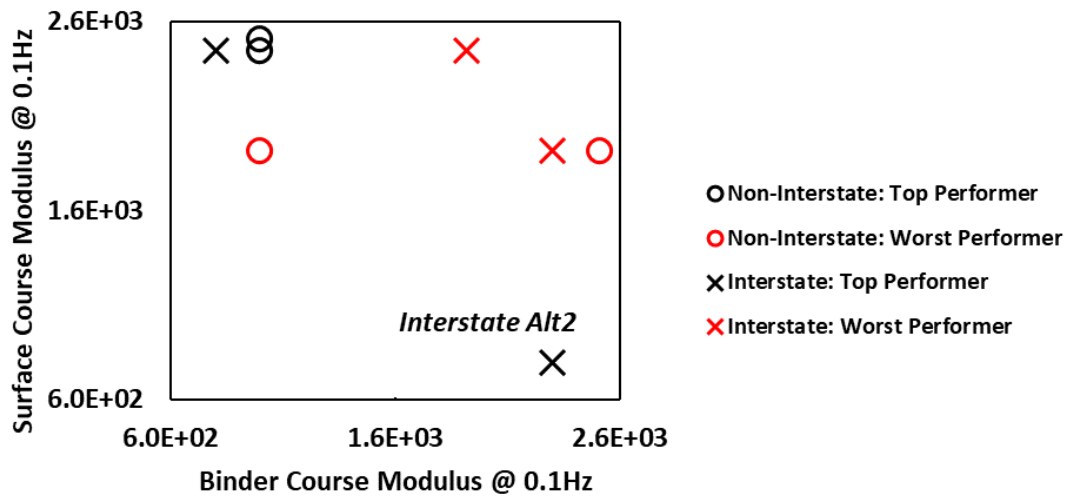


Figure 64. Chart. Effect of HMA modulus on overlay performance against reflective cracking.

Effect of Overlay Thickness

Overlay thickness played a critical role in performance against reflective cracking. As discussed in a previous section, thicker overlays were less likely to experience severe debonding at the binder–PCC interface and slab faulting, resulting in longer service lives because of higher load transfer efficiencies.

Moreover, thickness could enhance an overlay’s reflective cracking resistance. For example, although non-interstate alternative 1 had a brittle binder course, the extra 0.5 in (12.7 mm) thickness led to similar performance compared to the non-interstate control. As expected, the thicker the HMA overlay, the enhanced resistance to reflective cracking, given that other parameters were unchanged.

SUMMARY

The following are the findings from the experiment program:

- Joint opening significantly impacted reflective cracking behavior. Although all scenarios started with the same joint width, interstate scenarios had 54% wider joint openings. Hence, excessive tension-induced cracks appeared within the overlays in the early stages, making interstate scenarios fail relatively quickly despite their thick designs. The significant joint opening was likely due to the binder course’s relatively larger NMAS and coarser gradation. This could result in less effective bonding areas with the PCC slabs.
- Debonding at the binder–PCC interface substantially affected crack initiation. If debonding occurred before tension cracks, caused by excessive joint opening, then debonding would dominate reflective crack initiation. A bottom-up reflective crack often initiated near the

end of the debonding area. In contrast, a top-down crack often initiated on the opposite side of the debonding region with respect to the joint. Moreover, delayed debonding would cause a delayed crack initiation, resulting in delayed failure.

- Debonding at the surface–binder interface impacted crack propagation. If one of the HMA layers was polymer-modified while the other was not, significant debonding would occur at the surface–binder interface. Because of the debonding, reflective cracks stopped propagating at the interface. However, they would “re-initiate” at the interface. Slight offsets to the previous crack paths were often observed.
- Thickness significantly affected HMA overlays’ performance against reflective cracking. A thicker HMA overlay provided better bridging for the PCC slabs across the joint. Hence, higher load transfer efficiency would be expected, even when the overlay was fully cracked. Slab faulting was less likely to occur with relatively thicker HMA overlays. Moreover, less debonding between the binder course and PCC slab was observed for relatively thicker overlay scenarios. In summary, the thicker the HMA overlay, the enhanced resistance to reflective cracking, given other parameters were unchanged.
- An optimum overlay to control reflective cracking is an overlay composed of a high modulus and flexible surface course and a flexible binder course.

Based on the experimental results, the following overlay configurations are recommended to control reflective cracking:

- Non-interstate: An overlay composed of an SMA-9.5 surface course and an IL-4.75 binder course is recommended. SMA-9.5, made with local Illinois gravel, may be considered to reduce cost. An IL-9.5FG surface course and an IL-4.75 binder course are recommended for low-volume and low-speed roads.
- Interstate: An overlay composed of an SMA-12.5 surface course and an IL-19.0 binder course is recommended. An SMA-9.5 surface course and an SMA-12.5 binder course are suggested when a thin structure is being considered.

In addition, the following steps are recommended to mitigate reflective cracking:

- Treat deteriorated PCC joints/cracks prior to overlay application. One method is sawing a PCC to create a new joint at a deteriorated joint location, followed by sealing (Elseifi et al., 2011). However, more research is needed to determine the best approach.
- Ensure HMA mixtures have acceptable FI.
- Apply polymer-modified lifts.
- Ensure interlayer bonding is properly achieved with existing pavement and between lifts. ICT project R27-100 found that the optimum tack coat residual rate was 0.04 gal/yd² (0.18 L/m²) for trafficked and non-trafficked unmilled aged HMA surfaces, while the optimum

residual rate for milled HMA was 0.06 gal/yd² (0.26 L/m²). SS-1vh tack coat showed superior performance, and the optimum curing time was determined to be two hours (Al-Qadi et al., 2012; Salinas et al., 2013). Moreover, ICT project R55 recommended applying SS-1hP at HMA-PCC interface with a residual rate of 0.04 gal/yd² (0.18 L/m²) (Al-Qadi et al., 2009). A higher tack coat application rate may be considered for binder courses with a large NMAS ($\geq 3/8$ in [9.5 mm]).

- Ensure densities of overlay lifts are met.
- Ensure adequate thickness. A surrogate model is presented in Chapter 4 to assist engineers in selecting mixtures and designing lift thicknesses.

CHAPTER 4: MECHANISTIC ANALYSIS

INTRODUCTION

Large-scale testing is time-consuming and expensive. Hence, it is impractical to test all possible scenarios. Therefore, the main goal herein is to develop a generalized 3D finite-element (FE) model that predicts reflective cracking potential for scenarios other than those considered in this study. There are several subtasks involved to achieve this objective, as listed below:

- Model large-scale testing accurately using the FE method.
- Incorporate fracture properties into the model.
- Correlate fracture parameters obtained from the model with experimental results, known as model validation.
- Create a simulation matrix based on critical parameters affecting reflective cracking behavior. Use the database to understand the impact of parameters on cracking potential.
- Develop a surrogate model using the database to aid agencies in predicting cracking potential.

MODEL DEVELOPMENT

Finite-Element Modeling

The test slab has four different layers. The top two layers, namely the wearing surface and binder course, consist of HMA with different material properties assumed to exhibit viscoelasticity. The first two layers are compacted over a cracked PCC slab, an elastic material. Three layers are placed on a compacted fine sand subgrade, modeled as a linear elastic layer. Bonding and slippage between layers are different due to the variation in different friction coefficients. The load emulates a moving tire, so it is time dependent, which increases the complexity as it is a dynamic analysis.

Because of the abovementioned complications, deriving an analytical solution for the given system is strenuous. Therefore, for such systems, the FE method divides the complicated system into small units called “finite elements” (the process known as meshing). Each small element has a set of complicated equations formulated as simple algebraic equations. Then, the system of algebraic equations is solved for the entire system to obtain the solution. Hence, the actual configuration of the test slab and loading were modeled using the FE commercial software ABAQUS.

The test slab configuration was simulated as a 3D FE model. The model’s geometry was the same as the actual dimensions of the slab. Thickness and material properties were changed based on the various considered scenarios. The details of the model are discussed in the following sections.

Material Properties

HMA layers were modeled as linear viscoelastic materials. A dynamic modulus master curve was used to characterize linear viscoelasticity. A Prony series was fit for each HMA mix presented in Figure 19 to obtain Prony coefficients. The master curve may be inputted into the FE model as Prony coefficients along with shift factors for the Williams-Landel-Ferry equation (Williams et al., 1955). PCC and subgrade were modeled as linear elastic materials because of PCC behavior and low stresses at the subgrade.

Layer Interface

Layer interactions were modeled using the Coulomb friction (stick-slip) model. The shear stress above which slipping occurs is known as critical shear stress and is illustrated in Figure 65. The critical shear stress value, a significant parameter found in the experimental program, was chosen such that slipping occurs between layers.

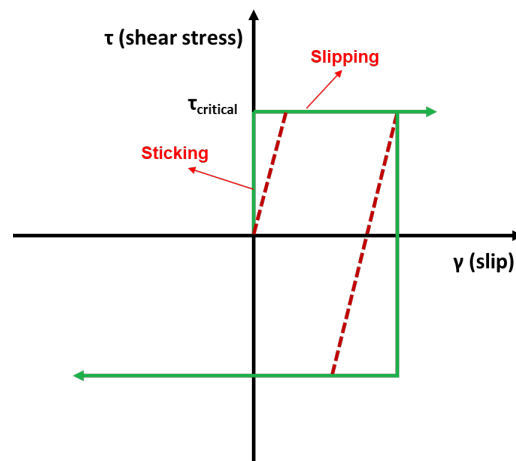


Figure 65. Illustration. Stick-slip model.

Loading and Boundary Conditions

As mentioned in Chapter 3, testing comprises three loading steps to simulate a moving tire. In the first step, the left plate applies a load while the right plate applies almost zero or no loads. Step 1 represents the scenario of a tire approaching the crack. In the second step, both plates apply the load simulating the tire on top of the crack. The third step is the reverse of the first step: only the right plate applies a load, and the left plate does not apply a load. Step 3 models the tire leaving the crack. One repetition is a complete application of loads from steps 1 to 3. Figure 27 illustrates all steps.

Two plates were modeled 1 in (25.4 mm) apart. Two rectangular loading plates were modeled by partitioning the surface of the model. The dimensions of the rectangular loading plates are 15 in (381 mm) long and 7 in (177.8 mm) wide. The motion of the tire causes cracking in different modes. Steps 1 and 3 are Mode II (in-plane shear) loading, while step 2 is Mode I (opening). The three phases of a loading cycle were modeled using the steps module in ABAQUS, and loading was applied with amplitude to simulate the pulse loading by the actuators (Figure 28). Dynamic analysis was carried out, as loading is a function of time.

PCC was modeled with a notch to emulate the saw cut in the testbed. Boundary conditions (BCs) are predefined loads and displacements applied on the system that do not change with time. The lateral sides of the test slabs (until the PCC slab) are entirely unrestrained. The compacted sand, or the bottommost layer, is wholly restrained (i.e., no displacements or rotation is allowed). Therefore, in the FE model, the subgrade was fixed entirely, while lateral surfaces of other layers were free. Figure 66 presents the final 3D FE model. Figure 67 summarizes various considerations of the testbed model.

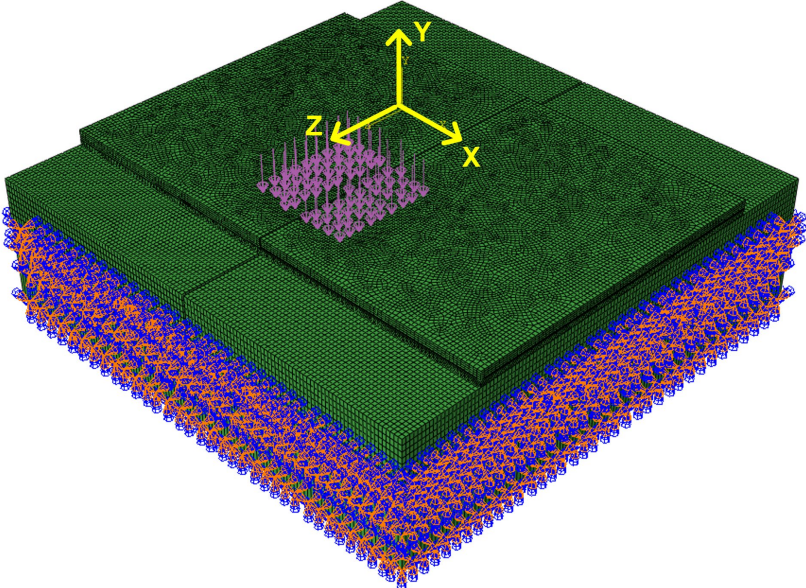


Figure 66. Illustration. 3D FE testbed model.

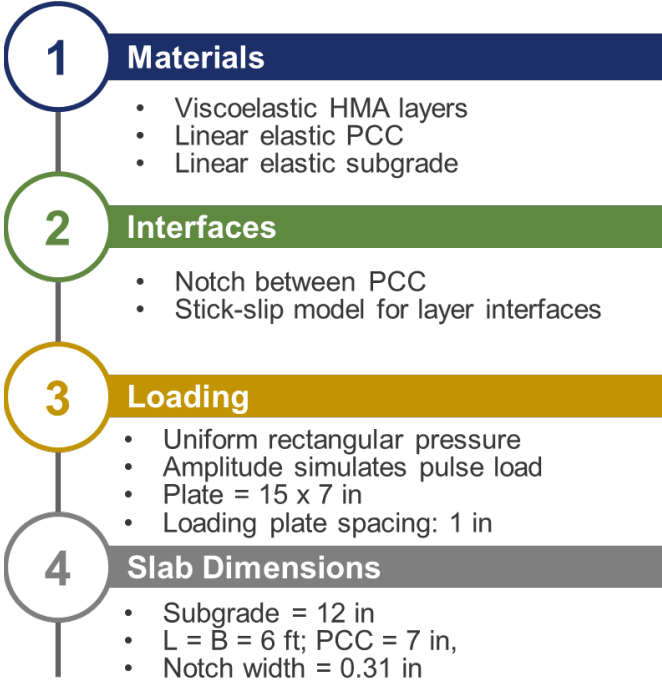


Figure 67. Flowchart. Considerations of testbed model.

Fracture Modeling

Crack initiation and propagation depend on several factors such as loading configuration, initial crack length, system geometry, and fracture toughness of the material. Therefore, the cracking mechanism cannot be fully understood from the tensile strains at the bottom of HMA layers. J-integral and SIF are critical parameters in fracture mechanics. J-integral, also known as the path-independent integral, is defined as strain energy release rate, or energy released per unit fracture surface area (Rice, 1968). It is used to characterize the severity of loading at the crack tip. In general, stresses around the crack tip are significantly higher than the region slightly far from the crack, known as stress concentration. SIF is the measure of stress concentration or stress field near the crack tip or any flaw in the system. Higher SIF values imply a faster crack propagation rate. J-integral and SIF are well accepted parameters in the field of fracture mechanics to understand crack propagation for linear elastic and viscoelastic materials. When HMA is considered as a viscoelastoplastic material, SIF would be an inappropriate measure due to the presence of a larger plastic zone near the crack tip. For complicated geometries, it is easier to compute J-integral around the crack tip than SIF. Hence, FE models compute J-integral and compute SIF using J-integral values. Fracture properties should be explicitly modeled, as the goal is to correlate experimental data with fracture parameters.

Crack in Surface and Binder Course

To calculate the J-integral directly from ABAQUS, a crack front, crack tip, initial crack length, crack propagation direction, and seam (region in the model that can open during a crack) must be assigned. The crack was assumed to initiate from the bottom and propagate toward the surface. In the model, a crack was assigned to both the surface and the binder course. A crack was placed in the center of the model (above the PCC) with an initial crack length of 0.39 in (10 mm) (Figure 68). The red arrow in Figure 68 presents the seam where the crack was placed and expected to crack. The region inside the red square is the crack front region, with blue dots as the crack tip. The radius of the crack front is 0.2 in (5 mm). The crack is placed along the entire model (i.e., it passes between the loading plates—parallel to the inner edges).

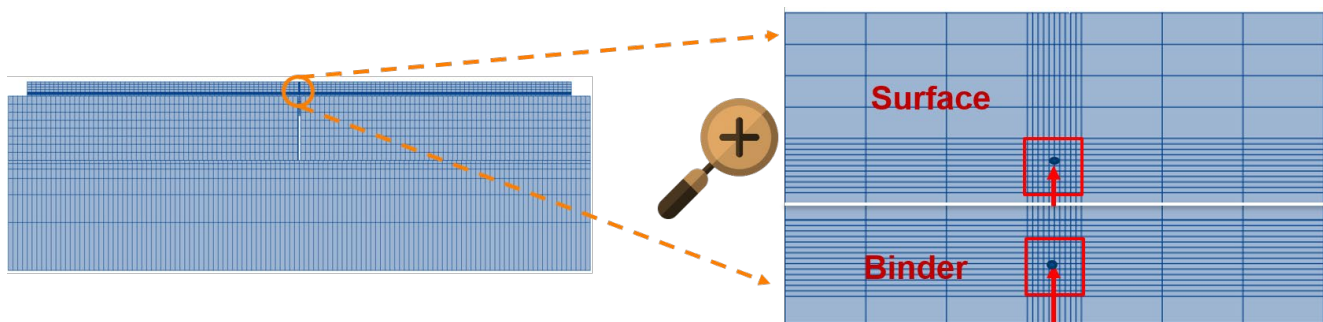


Figure 68. Illustration. Assigned crack front on the FE model (side view).

Meshing

Figure 66 and Figure 68 present the 3D and side views, respectively, of the overall meshed 3D FE model. In general, the accuracy of the solution for a FE model directly correlates with mesh size. As the mesh becomes finer, the complicated behavior of the system can be captured more accurately

but the model becomes more computationally intensive. Hence, the FE model achieves balance when the mesh of the regions of interest is fine while the mesh of the less important parts is coarse. Therefore, the top two layers of the FE model (surface and binder course) were finely meshed along the depth, while PCC and subgrade were coarsely meshed (Figure 68). The average mesh size (along the depth) for the surface and binder course was 0.39 in (10 mm) while the bottom two layers were around 1.4 in (35 mm). The mesh size on the surface in the XZ plane (Figure 66) was kept uniform along the depth of the slab, with an average size of 0.6 in \times 0.6 in (15 mm \times 15 mm). To put it in perspective, even the largest element in the model is less than 2% of the model's actual size.

The fracture parameters' computation requires significantly finer mesh than non-cracked regions because of the stress concentration around the crack. The crack front region is zoomed in, and the mesh could be much finer than the region surrounding the crack front (Figure 68). The average size of the mesh in the crack region is 0.04 in \times 0.04 in (1 mm \times 1 mm), and the mesh is extremely fine. However, verifying if the current structure would give accurate results is critical. A common practice to verify the accuracy is to check the J-integral values for different contours (Abaqus et al., 2014). The J-integral can be obtained directly from ABAQUS for different contours. Contours are imaginary concentric rings surrounding the crack tip in which J-integral values are computed, as presented in Figure 69. The software draws the contours automatically based on the number of contours requested. Theoretically, J-integral values are zero over a closed path and path independent. In other words, the J-integral should be the same for all contours. However, as FE is a numerical method, solutions are approximate in nature. Therefore, a test of good mesh would be the closeness and smoothness of J-integral values for different contours.

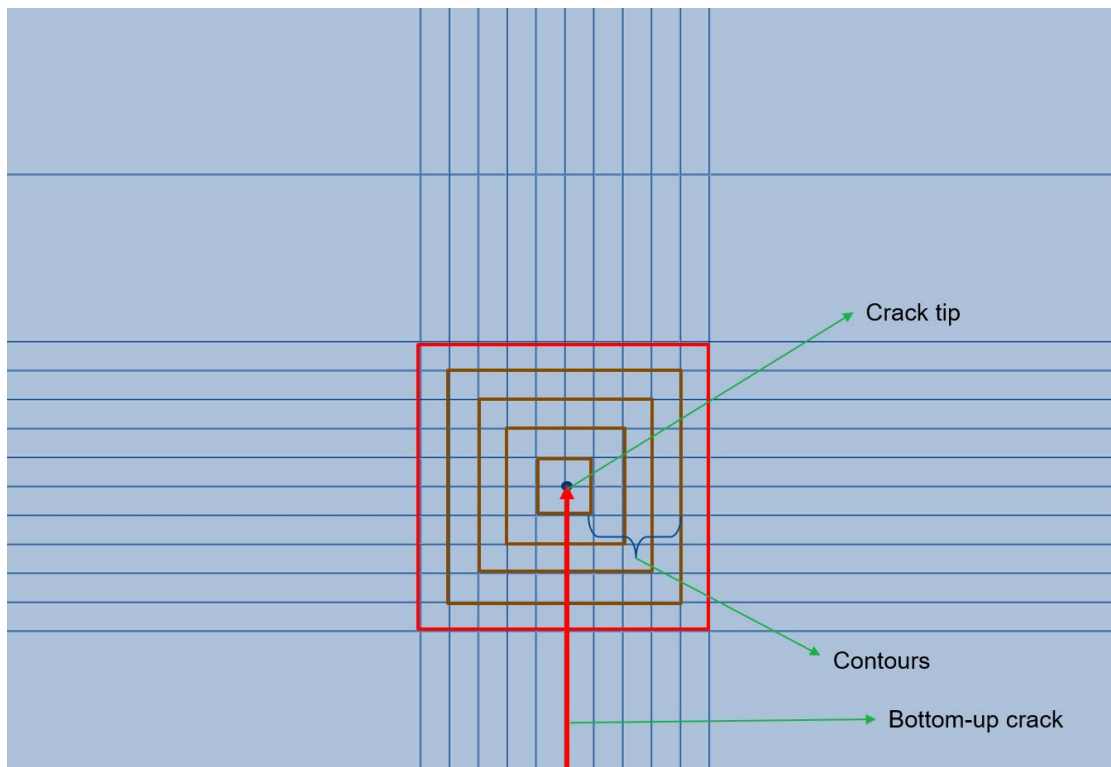


Figure 69. Illustration. Contours around the crack tip.

Figure 70 presents J-integral values for a final 3D FE model incorporating the aforementioned considerations for different contours. Values are plotted along the placed crack (i.e., along the transverse direction of the slab), a line passing between the loading plates. The first contour is different (as FE is an approximate solution), and values begin to converge as the number of contours increases (Figure 70). The minimum number of contours is determined by increasing the number of contours until there is no difference between them. Five contours were sufficient for the developed FE model, as the difference between the first and fifth contour is less than 1%. This finding implies that the current mesh structure is robust. If the mesh structure is poor, J-integral values tend to be noisy. Using quadratic shape functions results in smooth and accurate values, but it is generally used only for 2D models. Using quadratic shape functions for 3D models increases the computational cost exponentially, and it might not be a viable option to evaluate many cases. Several iterations were performed to identify the final optimized mesh structure for the crack region that gave accurate results without significantly increasing computational costs. Initially, a circular crack front was tried with a different mesh structure, resulting in an inaccurate and noisy J-integral.

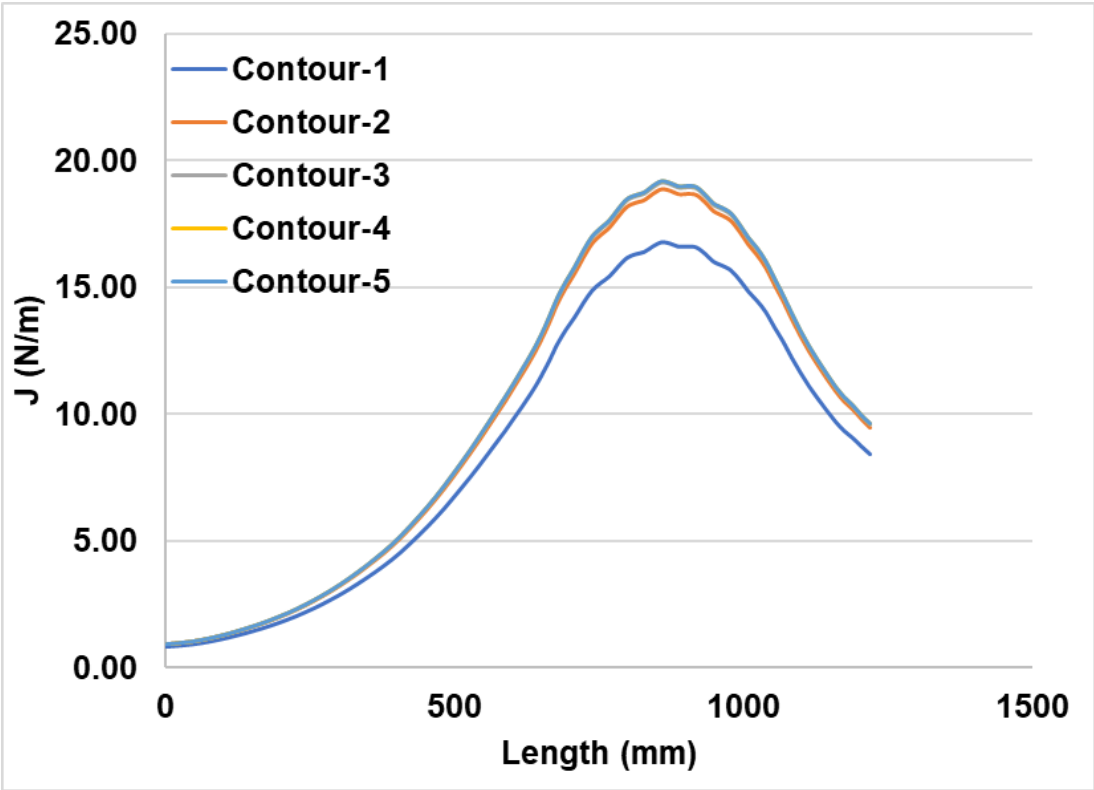


Figure 70. Graph. J-integral values for different contours.

MODEL RESULTS AND DISCUSSION

The main goal is to correlate the testbed results with computed fracture parameters from the FE analysis. Before correlation, fundamental trends of fracture parameters for the given setup need to be discussed and understood. With the above considerations, all test cases were simulated in ABAQUS. The FE model for the non-interstate control scenario is presented in Figure 71. Two cracks can be seen on the surface and binder course and are referred to as CS and CB, respectively.

Similarly, cracks were observed on the model for all other test cases. The model's X, Y, and Z directions are longitudinal, vertical, and transverse, respectively (Figure 66). Fracture parameters and other responses were post-processed for the fifth contour along the Z direction (crack tip line) for three complete load cycles.

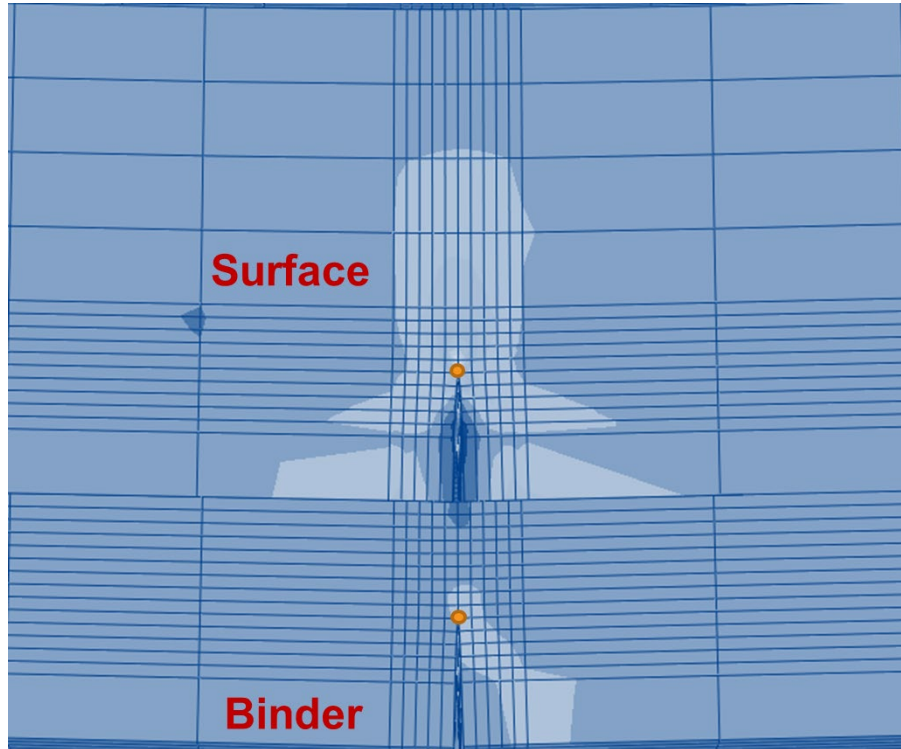
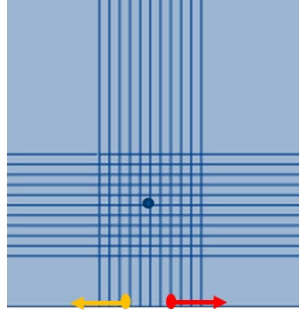


Figure 71. Illustration. Cracked FE model for non-interstate control scenario.

Crack Mouth Opening Displacement

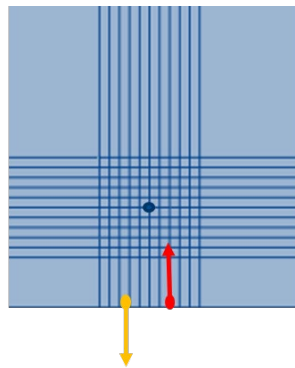
Crack mouth opening displacement (CMOD) is a measure of crack width for any given system that is normal to the crack plane at the crack's farthest points from the tip. CMOD can be measured easily through experiments, and its mathematical relationship with applied force yields a crack tip opening displacement (CTOD). CTOD is a vital fracture mechanics parameter representing the material's ability to resist the crack extension for strains at the crack tip (Newman et al., 2003). CMOD also serves as an insightful means to understand different modes of cracking for any loading system. CMOD for the model can be calculated by subtracting the displacements on either side of the crack. As mentioned earlier, the loading setup induces Mode I opening (during step 2) and Mode II in-plane shear cracking (during steps 1 and 3) (Figure 27).

Figure 72 presents the CMOD calculation for two modes of cracking in a load cycle. R and L in Figure 72 stand for the right and left sides of the crack, respectively. Figure 72-B represents the dominant movements that occur during steps 1 and 3 of the load cycle, while Figure 72-A represents step 2. In the case of Mode II shear cracking, CMOD is the relative displacement of the crack mouth in the vertical (Y) direction. However, for Mode I cracking, it is relative displacement along the longitudinal direction (X) direction.



$$CMOD_I = u_R^x - u_L^x$$

A. CMOD for mode I cracking



$$CMOD_{II} = u_R^y - u_L^y$$

B. CMOD for mode II cracking

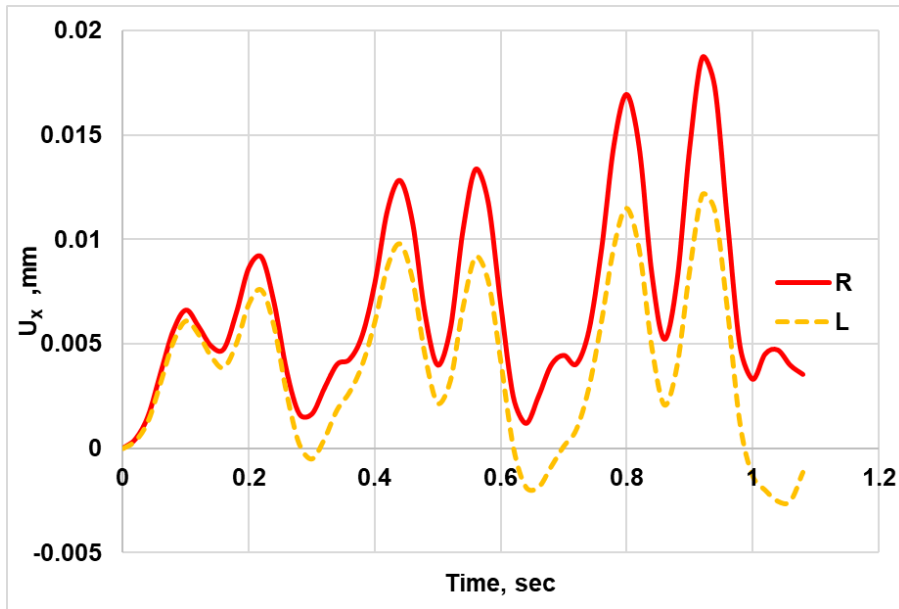
Figure 72. Illustration. CMOD for two modes of cracking.

For Mode I cracking, Figure 73-A presents the longitudinal displacement of elements on either side of the CB. Displacement follows the load amplitude (i.e., it increases as the load increases and vice versa). However, the displacement does not come to its original value after the load application and the amplitude of displacement increases. This behavior is expected as the layers were modeled as a viscoelastic material. HMA layers do not recover fully after load application using the current load/rest period cycle; in fact, there is a significant accumulation effect with the application of the load cycle. Another critical observation is that the displacement of the right-side element is consistently higher than the left side. CMOD increases with the application of load cycles (Figure 73-B). This finding shows that the crack is widening with the application of load as if cracks are subjected to tensile force.

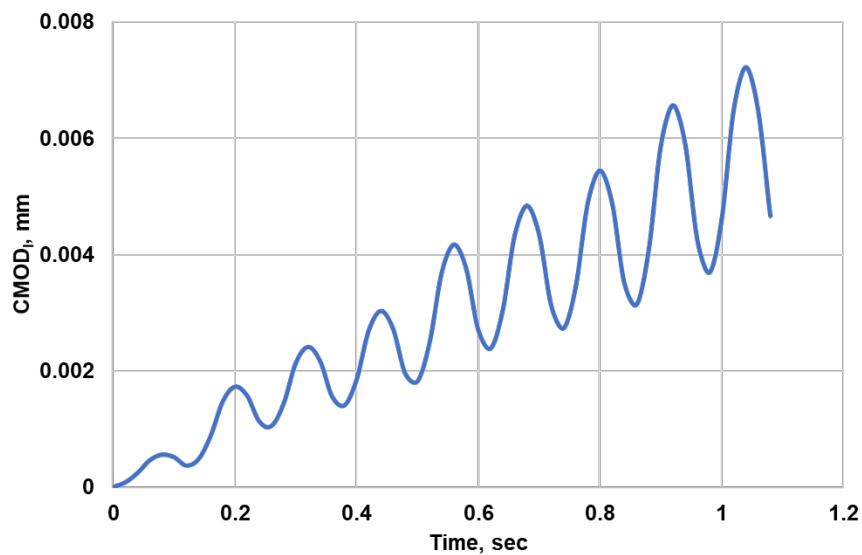
For Mode II cracking, Figure 74-A presents the vertical displacement of elements on either side of the CB. Similar to Figure 73-A, vertical displacement follows the load amplitude and accumulates with load application because of the relaxation behavior of viscoelastic materials. Unlike the previous scenario, the vertical displacement of the right-side element is almost equal to the left side. CMOD is nearly constant with the load application (Figure 74-B). In-plane shear cracking is an insignificant

cracking mechanism for the given problem. The values of vertical displacements were the order of magnitude compared to longitudinal displacement (Figure 73-A and Figure 74-A). However, CMOD for Mode I cracking was almost two orders higher than Mode II.

Mode I cracking is dominant and significant compared to Mode II cracking for the developed FE model. Though the results are presented only for the non-interstate control scenario, the trends were similar for all test cases, including interstate scenarios.

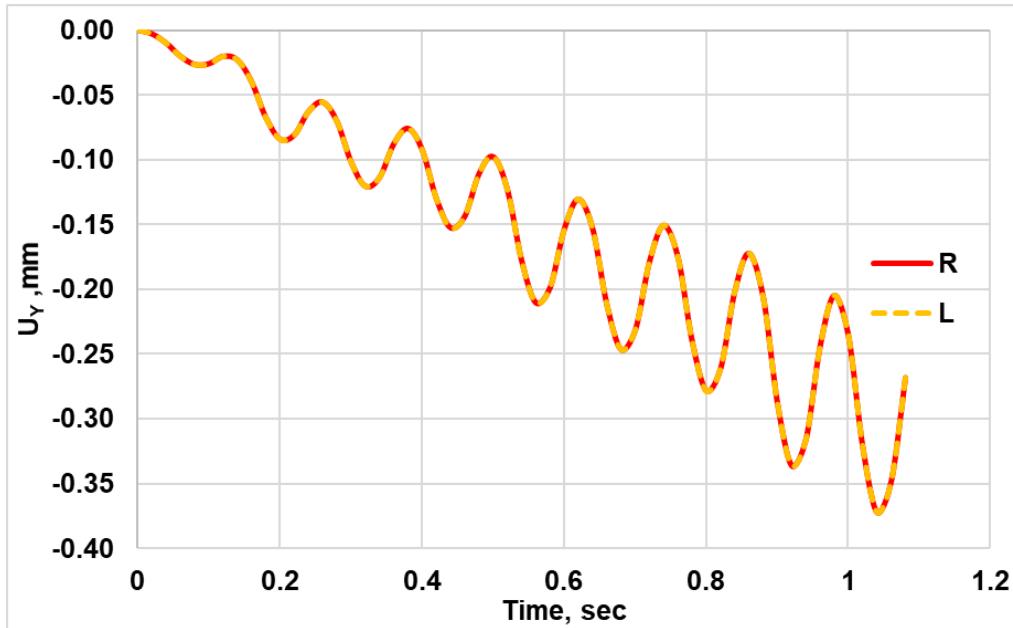


A. Displacement of elements on either side of the crack along the X direction

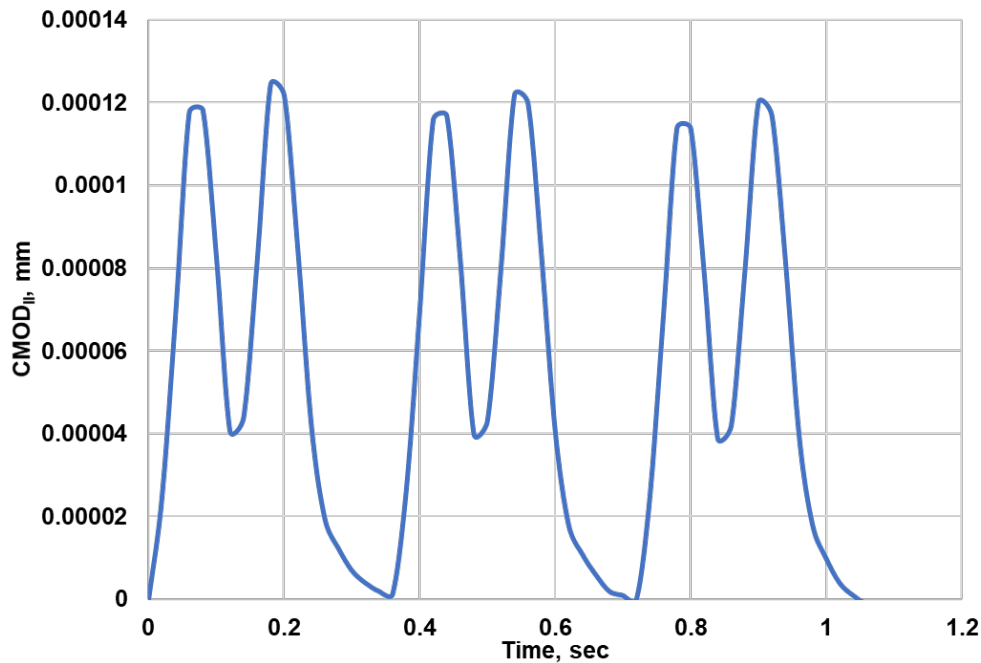


B. $CMOD_I$ for the given model.

Figure 73. Plots. Displacement and CMOD for mode I cracking.



A. Displacement of elements on either side of the crack along the Y direction



B. $CMOD_{II}$ for the given model

Figure 74. Plots. Displacement and $CMOD$ for mode II cracking.

Stress Intensity Factor and J-integral

In fracture mechanics, SIF, denoted as “K,” is computed for different modes of cracking. However, the analysis of $CMOD$ highlighted the importance of Mode I cracking over Mode II. Thus, only the SIF of

Mode I cracking was used as a fracture parameter (Baek et al., 2010). Figure 75 presents the SIF (K_I) for Mode I cracking in the non-interstate control scenario for binder course (CB). Figure 75 is a 3D plot where K_I increases with time and also along the Z direction. K_I is similar to the displacement presented in the earlier plots for mode I cracking. K_I values can be observed to be U-shaped within the edges of loading plates. To understand this observation, tensile strain distribution at the bottom of the binder course was analyzed. In Figure 76, red circles represent the edges of loading where the jump in the values was observed. Along the length of the loading plate, small magnitudes of compression values were observed. Compression values resulted in lower SIF values, as it prevents crack propagation. In addition, compression was observed for step 2, where the loading is pure bending. The main cause of this phenomenon was concrete bending under the loading. As the PCC slab had a complete notch, it behaved like two cantilever beams. Figure 77 illustrates the phenomenon. When loading was applied, the top edges of the PCC slab moved toward each other, inducing compression on the bottom of the binder course. The movement was higher under the loading plates, resulting in compression on the HMA. The variation of J-integral versus time and length of the model was approximately similar to K_I .

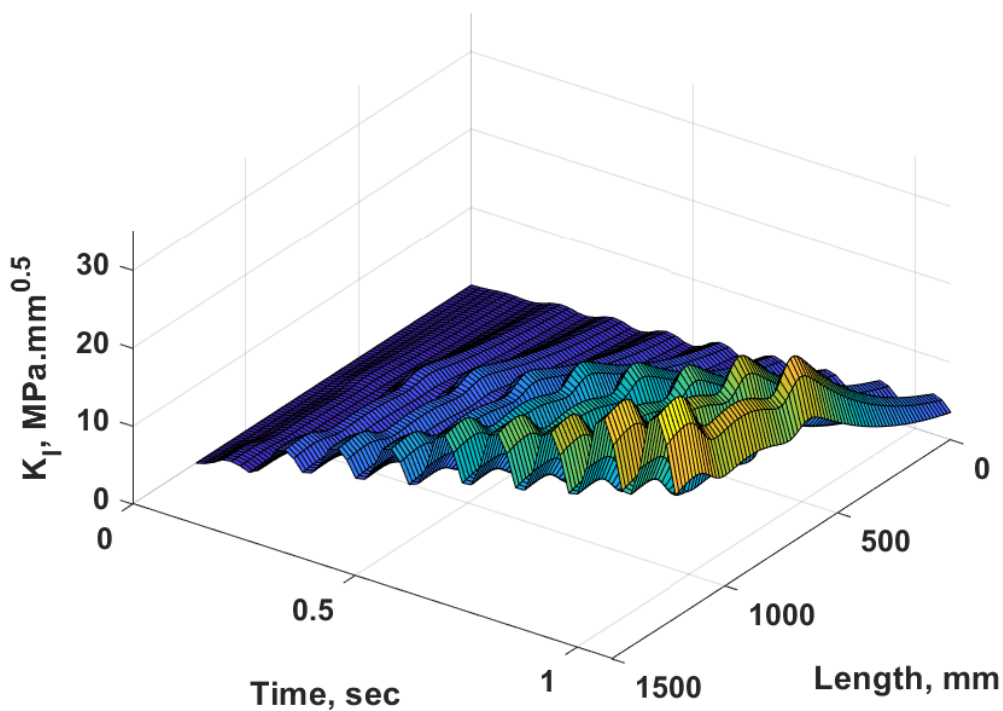


Figure 75. Plot. 3D plot of SIF versus time and length of the model ($1 \text{ MPa}\cdot\text{mm}^{0.5} = 28.8 \text{ psi}\cdot\text{in}^{0.5}$).

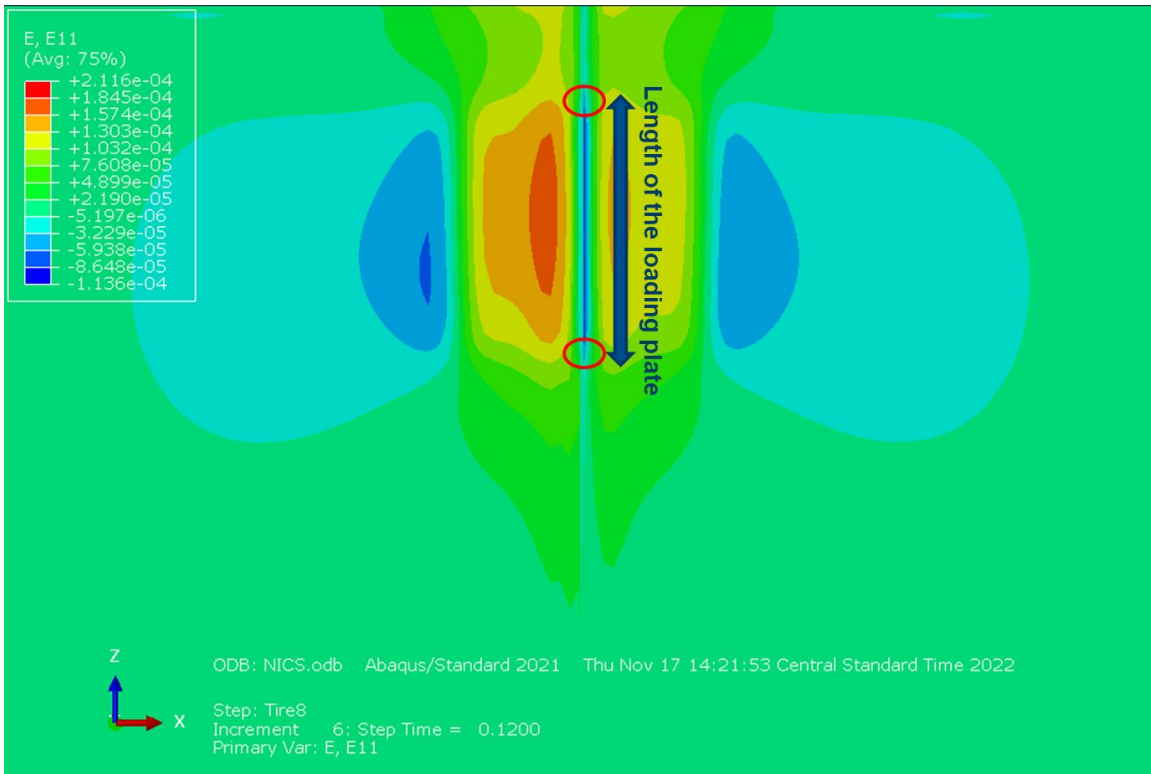


Figure 76. Illustration. Tensile strain distribution at the bottom of the binder course.

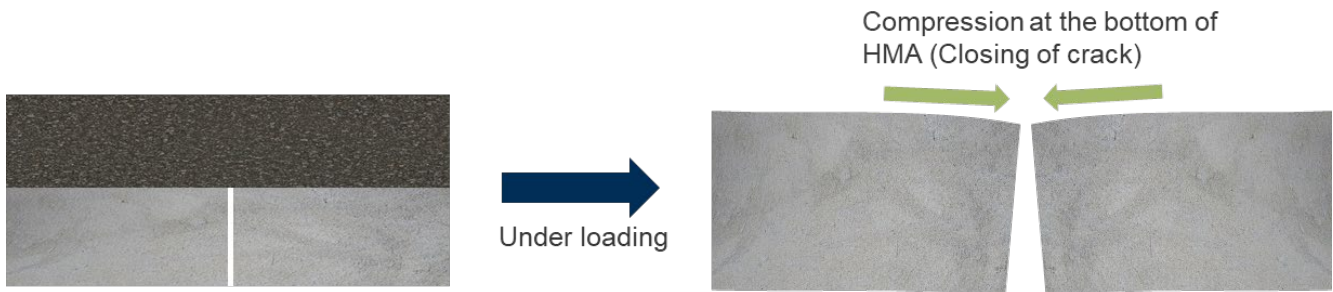


Figure 77. Illustration. PCC under loading (side view).

MODEL VALIDATION

The aforementioned results and discussion are theoretically acceptable. However, the results still lack validation from the actual testbed experimental data. The developed model is limited as it cannot account for any heterogenous or uncertain field/lab conditions. The parameters obtained from the model can predict the reflective cracking potential for any configuration. Experimental data should be compared qualitatively to the fracture parameters obtained from the model. Table 15 presents maximum J-integral and K_I values for all test cases (both interstate [IS] and non-interstate [NIS]) and both cracks (CS and CB).

Table 15. Fracture Parameters for Non-Interstate and Interstate Scenarios

Scenario	CS – J-integral (N/m)	CB – J-integral (N/m)	Average J-integral (N/m)	CS – K _I (MPa.mm ^{0.5})	CB – K _I (MPa.mm ^{0.5})	Average K _I (MPa.mm ^{0.5})
NIS Control	52.75	33.88	43.32	37.82	25.97	31.90
NIS Alt-1	40.10	41.40	40.75	32.98	33.47	33.23
NIS Alt-2	49.80	32.68	41.24	37.01	25.63	31.32
NIS Alt-3	44.52	34.12	39.32	34.91	25.65	30.28
IS Control	24.16	52.39	38.28	25.60	37.03	31.32
IS Alt-1	29.64	52.50	41.07	22.13	37.08	29.61
IS Alt-2	30.52	33.32	31.92	29.98	23.29	26.14
IS Alt-3	34.65	42.61	38.63	30.88	33.73	32.31

* 1 N/m = 0.068 lb/ft; 1 MPa.mm^{0.5} = 28.8 psi.in^{0.5}.

In Table 15, J-integral and K_I values for both cracks were averaged. Averaging the parameters for both cracks allows one value to represent the entire system. Averaged parameters could be compared qualitatively between scenarios regarding potential reflective cracking. Higher J-integral and K_I values imply faster crack propagation or higher crack potential.

Test cases can be ranked based on either averaged J-integral or K_I values and can be compared with the performance of testbed sections. Table 16 presents the ranking, and averaged K_I is a valid parameter to predict the overlay performance (Aliha et al., 2020; Ameri et al., 2011; Schapery, 1984; Wu et al., 2014; Xu et al., 2015). The predictions from the J-integral are off compared with the experimental results. The J-integral encapsulates the strain energy release rate without any classification of the cracking mechanism. However, K_I is a parameter specific to Mode I cracking, and as presented in the previous section, Mode I is the dominant cracking mechanism.

Table 16. Ranking of Non-Interstate and Interstate Scenarios Based on Averaged Fracture Parameters (from Best to Worst)

Average J-integral (N/m)	Rank	Average K _I (MPa.mm ^{0.5})	Rank	Actual Rank (From experiments)
39.32	NIS Alt-3	30.28	NIS Alt-3	NIS Alt-3
40.75	NIS Alt-1	31.32	NIS Alt-2	NIS Alt-2
41.24	NIS Alt-2	31.90	NIS Control	NIS Control
43.32	NIS Control	33.23	NIS Alt-1	NIS Alt-1
31.92	IS Alt-2	26.14	IS Alt-2	IS Alt-2
38.28	IS Control	29.61	IS Alt-1	IS Alt-1
38.63	IS Alt-3	31.32	IS Control	IS Alt-3
41.07	IS Alt-1	32.31	IS Alt-3	IS Control

* 1 N/m = 0.068 lb/ft; 1 MPa.mm^{0.5} = 28.8 psi.in^{0.5}.

Average K_I predicted non-interstate scenarios accurately, but the last two predictions were off for interstate scenarios. Even with the actual data, the difference between the interstate control and

alternative 3 is small. Generally, the average K_I for interstate scenarios is lower than for non-interstate scenarios. This finding implies that interstate scenarios should have lower cracking potential than non-interstate scenarios. On the contrary, non-interstate scenarios were more resilient to cracking than the interstate scenario in the tests. As discussed earlier, the main reason for this finding was the final joint opening for interstate over non-interstate scenarios. In addition, this phenomenon was attributed to lower contact of binder course with PCC due to higher NMAS in interstate scenarios.

As the goal of the task is to develop a generalized FE model, only important inputs and parameters were factored into the model. Thus, the developed FE model has certain limitations. For example, the FE model does not have any inputs to model the faulting mechanism for thinner overlays. Similarly, the model could not predict several other case-specific observations discussed in Chapter 3. However, the results from the FE model could serve as a guide for engineers to understand the relative performance between two similar sets of scenarios.

MODEL FOR PREDICTING REFLECTIVE CRACKING POTENTIAL

The developed model was validated qualitatively in the previous section. Despite the accuracy, running the FE model demands significant computational time and resources. Hence, agencies might find it impractical to use the model. To overcome this challenge, developing a simple surrogate model that could predict the fracture parameters would be beneficial. The model could also be a tool that engineers and agencies may use to design overlays easily.

Simulation Matrix

Given limited computational resources, it is impossible to run cases for all possible inputs to predict fracture parameters. As discussed in Chapter 3, critical inputs that affect reflective cracking potential are thickness, material property, joint opening, and friction between the layers. Hence, a database was developed by identifying and running critical combinations of various inputs (Table 17). A total of 128 models were generated and were used to generate a surrogate model that could predict fracture parameters.

Table 17. Simulation Matrix for Non-Interstate and Interstate Scenarios

Input Parameter	Non-Interstate	Interstate
Surface course thickness (TH-S), in	1.5 and 2.0	1.5 and 2.5
Binder course thickness (TH-B), in	0.75 and 1.25	1.5 and 2.25
Surface course material property (MP-S)	Strong (SMA-9.5) and weak (IL-9.5)	Strong (SMA-9.5) and weak (SMA-12.5)
Binder course material property (MP-B)	Strong (IL-9.5FG) and weak (IL-4.75)	Strong (IL-9.5FG) and weak (IL19.0)
Joint opening (JO), in	0.3 and 0.8	0.3 and 0.8
Friction	Full bonded and full slip	Full bonded and full slip
Total Number of Cases	64	64

As presented in Table 17, extreme thicknesses, material properties, and friction conditions were used to generate the database. The benefits of a simulation matrix that covers extreme scenarios are twofold: the worst-case scenario could be identified, and the surrogate models could approximately predict the fracture parameters for intermediate scenarios. All cases were post-processed in a similar manner as test cases.

Surrogate Model

A surrogate model could predict the fracture parameters for any newer possible combinations in the simulation matrix. In addition, the model may be utilized to predict newer scenarios out of simulation matrix. However, extrapolations could sometimes be erroneous. The data were split randomly such that 70% of the data were used for training while the rest were used for the evaluation of the model (test data). Regression analysis and a neural network model are presented next.

Regression Analysis

Regressions are the simplest and easiest approach to train data, as regression analysis has closed-form solutions. It is also well-known for its interpretability. The major disadvantage is the model's lack of nuanced understanding of the relationships between inputs and outputs. Linear regression analysis was carried out, and the results are presented in Figure 78. Although linear regression performed relatively well, a few glaring issues need to be addressed for practical and confident application.

The responses concerning the K_I values were predicted accurately, as the points are closer to the equality line in Figure 78. The predicted responses for the J-integral were off from the actual values. As the actual J-integral is smaller, the model's predictive capability is lower than the region of higher values for both cracks (CS and CB). Hence, the error in the J-integral is larger than the total accuracy of the model. This finding implies that using the model to predict the J-integral accurately with other data sets is insufficient.

Another major issue with linear regression is that it lacks physical significance in some prediction areas. When the actual values are lower, the predictions are negative values for CS. In the actual physical system, a tensile crack at the bottom of the HMA layer could never be negative. However, compressive cracks are predicted by the model, which is physically meaningless. The prediction of negative values may be due to the linearity of the regression model.

Test Set Performance $R^2 = 0.728$

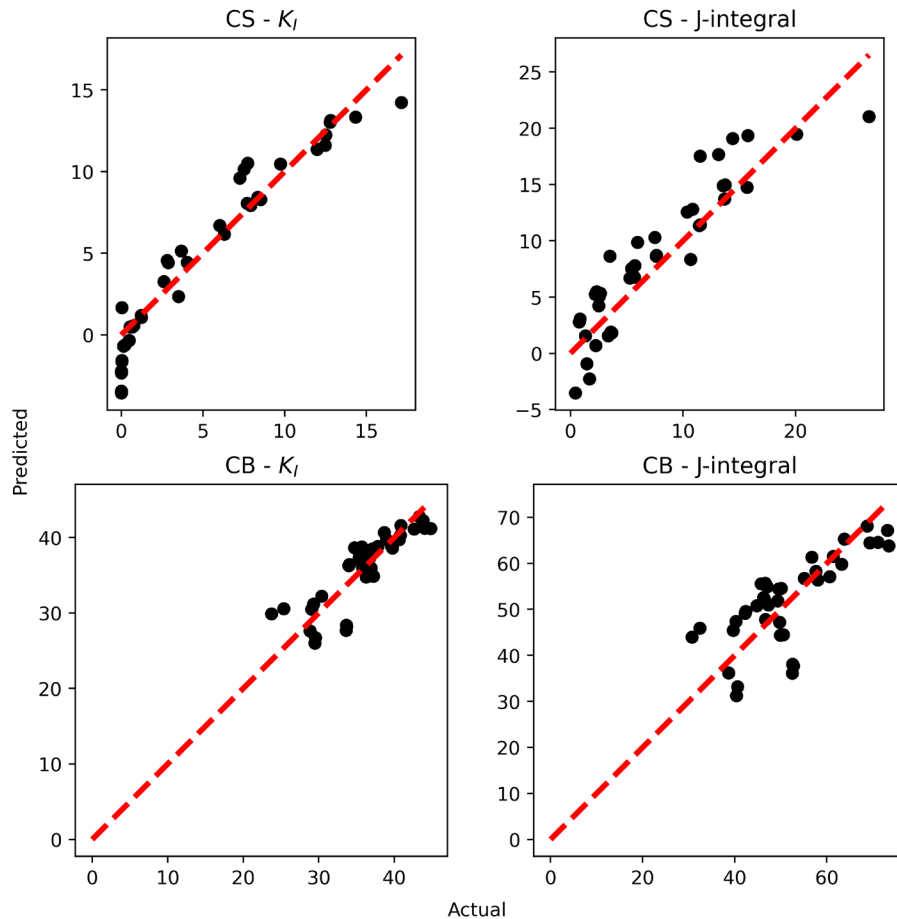


Figure 78. Graphs. Predicted versus actual fracture parameters using regression.

Neural Networks

An artificial neural network (ANN) is an efficient tool to overcome the limitations of a regression model. The main advantage of ANN is understanding complex nonlinear relationships between inputs and outputs. The ANN model requires more data points to work better than the regression models. However, a robust model could be trained such that predictions are well generalized and fairly accurate without any overfitting issues. An ANN model was trained to predict parameters for both cracks in contrast to the different weight matrices for each output in the case of linear regression.

The optimal architecture (number of layers and number of nodes) for the model was identified by trying several different model architectures. The architecture with the least test loss and lowest run time was selected. Two hidden layers, each with 30 nodes, were selected. As the database size is small, the “LBFGS” optimizer was used to train the model. Neural network prediction over the test dataset is presented in Figure 79. Predictions were more accurate than conventional regression analysis. The overall R^2 value for all the predicted values is around 0.92, and for the training data set, the value is 0.97. This finding shows that the model is well generalized and did not overfit.

Test Set Performance $R^2 = 0.92$

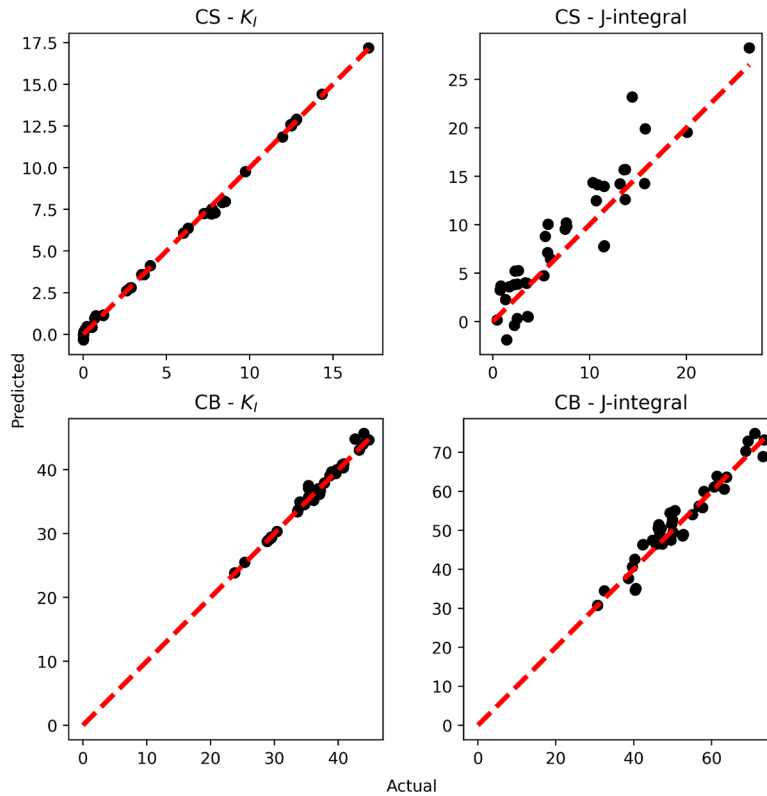


Figure 79. Graphs. Predicted versus actual fracture parameters using neural network.

The trained ANN model was incorporated as a simple and interactive webtool that can be used by agencies to obtain reflective cracking potential. The details of the tool are presented in Appendix B.

SHAP Analysis

Shapley Additive Explanations (SHAP), a game theory approach, is used to identify each player's contribution to a game (Lundberg & Lee, 2017). Each input is considered a player, and its contributions to the model are evaluated. Inputs are assigned a value based on their contribution. Inputs with higher SHAP values are important parameters. SHAP analysis can also provide insight into the relationship between inputs and outputs for a complicated system. Thus, SHAP analysis was carried out for the ANN model to understand the importance of inputs such as material property, joint opening, and thickness on fracture parameters. A bee swarm plot for computed K_I at CB summarizes the impact of inputs in a dataset on the model's output (Figure 80).

Each row corresponds to a feature. The color of the points represents the feature's magnitude, with red representing higher values. The x-axis value of the points represents the SHAP value of a test point (i.e., the relative importance of that feature for that point). K_I values are strongly influenced by the binder course's thickness and material properties, followed by friction, joint opening, and the surface course's thickness and material properties. The inputs' order of influence is logically based on the previous discussion. The model learned a positive relationship for some inputs like joint opening

and binder course. A positive relationship means outputs will increase and decrease with input. For example, the K_I value increases as joint opening increases, making it more prone to cracking failure. An example of a negative relationship is friction. Higher friction values improve cracking potential of the system. Both examples are theoretically expected and experimentally validated. This analysis provides valuable insight regarding the importance and relationship of inputs to output. Also, this analysis implies that the surrogate model developed using ANN is robust. SHAP analysis can also guide engineers to focus on specific design aspects while features of lower importance can be ignored.

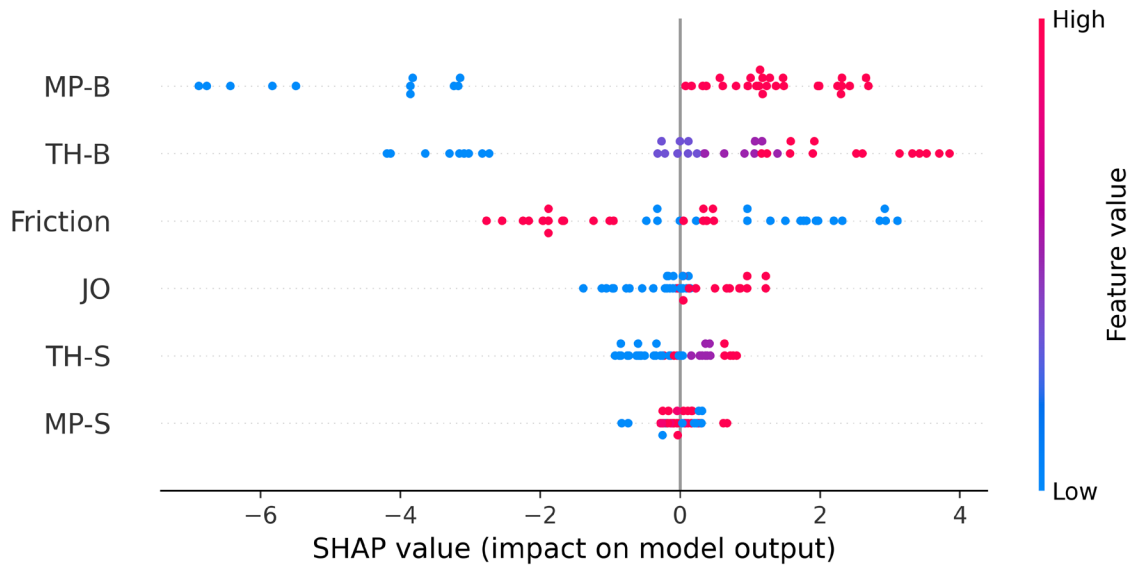


Figure 80. Plot. Summary plot of neural network model for K_I using test dataset.

SUMMARY

Overall, a 3D generalized FE model was developed to emulate large-scale testing accurately. As the goal is to understand cracking potential, fracture properties such as SIF and J-integral were modeled and computed. A crack front region with a crack tip and seam was assigned to both the surface and binder course. Elements in the crack front region were finer than the region surrounding the front to account for stress concentrations around the tip. Mesh sensitivity analysis was performed to ensure reliability with optimal running time. The closeness of J-integral contours was used to measure the reliability and accuracy of the mesh structure of the model. The developed model produced close and smooth J-integral contours.

CMOD was calculated for different modes of cracking by computing the relative displacement of the elements on either side of the crack. CMOD for Mode I cracking (loading step 2) increased with the loading cycles. However, CMOD for in-plane shear cracking (loading steps 1 and 3) remained constant with load application. This finding shows that Mode I, or tensile cracking, is the model's dominant mechanism for crack propagation. Therefore, SIF for in-plane shear cracking was ignored as a fracture parameter to quantify the fracture potential in this study. K_I , SIF for mode I cracking, and J-integral

were computed along the crack tip of the entire model. K_I and J-integral values increased with load application, and maximum values occurred at the edge of a plate load.

Then, the fracture parameter from the model was correlated to the experimental testbed results. Average K_I (CS and CB) was a measure to rank overlay crack potential for the given testbed conditions. K_I values were averaged to have a parameter that can represent the whole system. Rankings based on K_I were the same as the performance of various scenarios in the experimental plan. The model could be used only to compare scenarios qualitatively, as it lacks case-specific mechanisms such as bonding efficiency and slab faulting. A surrogate model that could predict reflective cracking potential was developed to make the model more usable for agencies. To develop a surrogate model, a database of 128 cases was generated to compute fracture parameters for extreme scenarios or a combination of inputs. Engineers could easily use the surrogate model when selecting mixtures and designing thicknesses.

A surrogate model can also be used to predict the fracture parameters for newer scenarios that are not in the database. The ANN was valid and better than the conventional regression model because of its ability to capture the complex relationship between inputs and outputs. A simple web-based tool considering the trained ANN model was developed to predict cracking potential. SHAP analysis was carried out to identify the importance and relationship of each input for predicting a particular output. For K_I at CB, important parameters were the thickness and material property of the binder course, and the values were less affected or almost independent of the surface course. This finding implies that the surrogate model is robust and can be used confidently for real-world problems.

CHAPTER 5: LIFE-CYCLE COST ANALYSIS

INTRODUCTION

Life-cycle cost analysis (LCCA) is a method to compare the overlay alternatives in this project to determine the lowest cost alternative. Life-cycle costs refer to all costs during a complete life cycle. LCCA includes costs associated with initial construction and future maintenance and rehabilitation activities. The life cycle starts when the project is initiated and opened to traffic and ends when the initial pavement structure is no longer serviceable. LCCA was performed to account for the initial and future costs associated with a HMA overlay. This chapter aims to compare studied overlay scenarios using LCCA. The assumed performance and treatments for the overlays are presented herein.

IDOT provided a database with 130 overlay projects. The data were collected from the nine IDOT districts between 2018 and 2019. The information includes contract number, district number, county, route name and length, date of construction, milling thickness, number of lifts, lift thickness, and HMA mix type and property.

HOT-MIX ASPHALT COST ANALYSIS

Summary Statistics for Overlay Activities

The database projects were organized by the district. As presented in Figure 81, statistical analysis was performed to estimate the average overlay thickness and the minimum and maximum overlay thickness in each district. The average total overlay thickness ranged between 2.5 in (63 mm) and 3.5 in (89 mm) across all districts, except District 6. The highest and lowest total overlay thicknesses were 1.5 in (38 mm) and 7.5 in (191 mm) in District 6.

Figure 81 presents the number of projects in each district. (The number of projects is listed in the white squares.). More than 30% of the 130 projects are in District 1. The remaining 70% of the projects are proportionately distributed within the other eight districts, except for District 7, which had limited overlay construction during this period (less than 4% of the shared data).

Cost Breakdown of Projects Per District

The initial cost, the primary contributor, was determined at year 0 of the analysis period. Although numerous activities were performed, only those specific to a pavement alternative were included in the initial costs.

According to the database, project length and number of lanes vary greatly. Therefore, the average initial cost was calculated for one lane mile, assuming HMA standard weight equals 112 lb/yd²in. The standard weight varies depending on several factors including mix type, aggregate lithology, and in-place density. Air void content is used interchangeably with density in this report. The typical target in-place density of a “dense” HMA pavement is 92% to 96% (4% to 8% air voids). An HMA mixture typically weighs 142 to 152 lb/ft³ in-place. Because of data limitations, an average conversion factor of 149 lb/ft³ (almost equal to 112 lb/yd²in) was used.

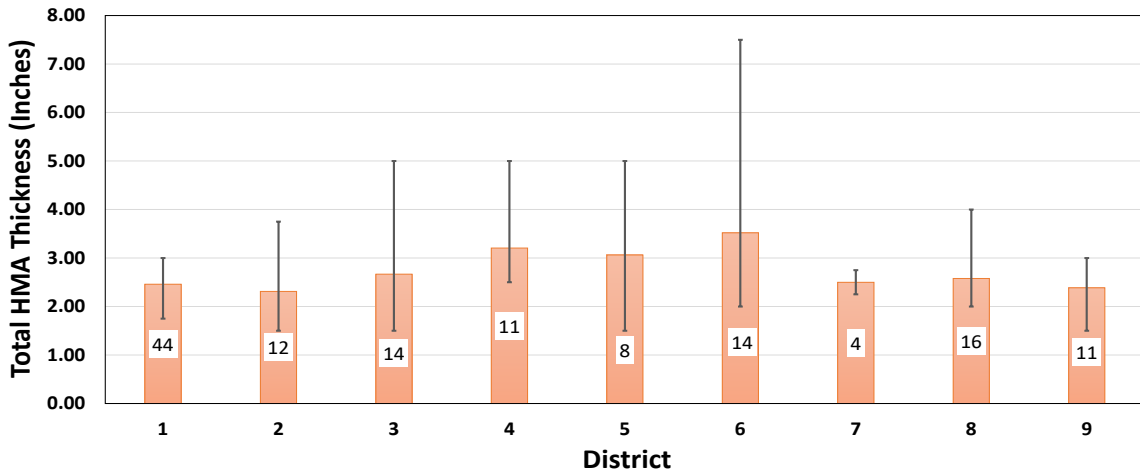


Figure 81. Chart. Total overlay HMA thicknesses (overlay projects 2018–2019).

Figure 82 presents the average initial cost for each district. According to the chart, the average initial cost per lane-mile ranges between \$100,000 and \$130,000. District 6 had the highest initial cost (projects with more than \$400,000 initial cost).

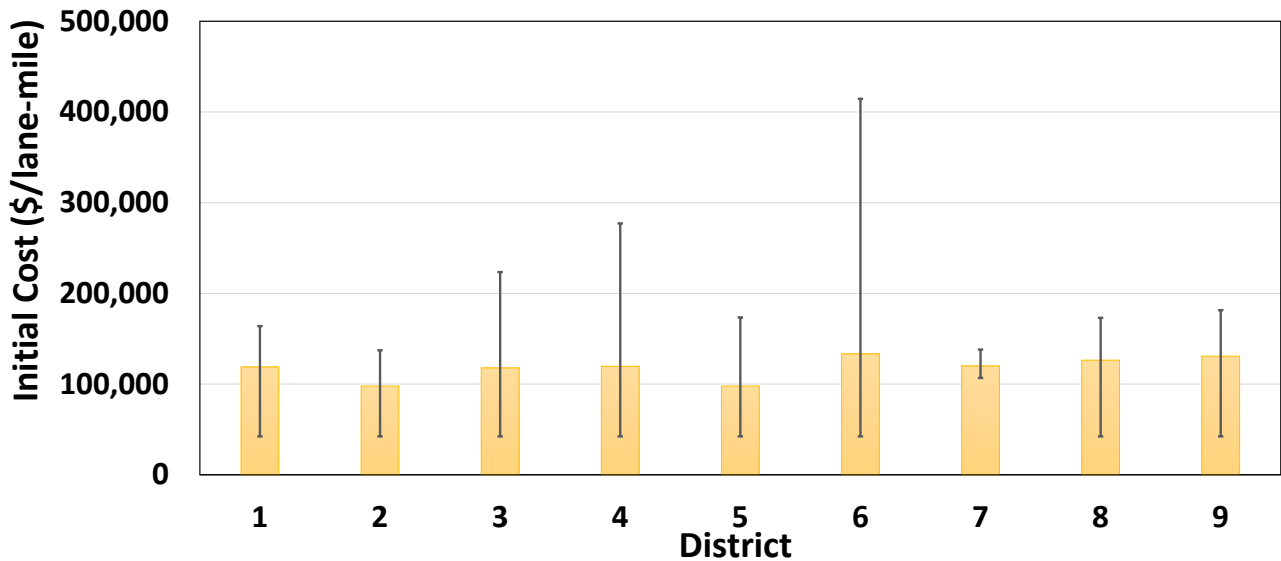


Figure 82. Chart. Initial cost of considered provided projects (overlay projects 2018–2019).

Mix Usage and Range Prices

The following mix IDs were used to group the pay items:

- Surface mixes:
 - HMA SC (primarily IL-9.5 and some IL-9.5FG)

- POLY HMA SC (IL-9.5)
- SMA SC (primarily IL-12.5 and some IL-9.5)
- Binder mixes:
 - HMA BC (IL-19.0)
 - POLY HMA BC (IL-12.5, IL-19.0, and IL-9.5)
 - SMA BC (Not used in the database provided)
- Leveling binder:
 - IL-4.75, IL-9.5, IL-9.5FG (identified as Poly LB, LB, or LEV BIND)

The minimum, maximum, and average prices per ton for each mix type were estimated from the dataset. In addition, the total quantity per ton for each mix was calculated. Table 18 presents these statistics. The HMA SC mix has the highest total quantity usage among all surface mixes. Poly HMA and SMA are used uniformly in the surface mixes. Although the average price of a Poly HMA mix is nearly twice that of an HMA mix, it has the highest total quantity usage for binder mixes. SMA was not a binder mix lift used in Illinois in the contract database provided. IL-4.75 was used the most as a leveling mix. Please note that IDOT no longer uses leveling binder applications.

Table 18. Summary of Cost Analysis 2018 to 2019

Mix Type		Min, \$/ton	Max, \$/ton	Average, \$/ton	Total quantity, tons	Total Cost, \$
Surface Mixes	HMA SC	37	109	79	349,600	27,661,869
	POLY HMA SC	60	151	94	252,010	23,749,278
	SMA SC	78	133	102	253,621	25,803,862
Binder Mixes	HMA BC	50	95	68	47,558	3,223,671
	POLY HMA BC	97	120	111	56,528	6,302,081
	SMA BC	N/A	N/A	N/A	N/A	N/A
Leveling Mixes	IL-4.75	70	128	88	227,826	20,144,138
	IL-9.5	80	90	84	25,937	2,183,377
	IL-9.5 FG	54	169	91	160,199	14,618,197

HMA Unit Price Analysis

For LCCA, multiple variables may affect the final pavement alternative, especially material cost. Hence, the engineer must ensure the unit cost is reasonable. The unit price analysis was performed using the information provided for the 2018 to 2019 projects. Nine files containing a database of unit prices were received from IDOT. Average unit prices were extracted based on overlay project scenarios to compare control and alternative HMA mixes for interstates and non-interstates. Average

unit prices were obtained directly from the contracts. The average unit prices for each overlay type were estimated and presented in Table 19. Weighted unit price averages were used to account for price fluctuations based on HMA tonnage in each project. Cost calculations were performed for each HMA mix category.

In general, the average unit prices range from \$63.5 to \$129.2, except for the high-value IL-9.5 mix in District 6. This value is derived from a single project with a low HMA tonnage and was excluded from the LCCA analysis. Some cells were left blank in Table 19 because only a few mixes were used in all districts.

Table 19. Unit Prices of Mixes in Each Overlay Scenario

DISTRICT		Non-interstate Scenarios				Interstate Scenarios			
		C	1	2	3	C	1	2	3
*	Surface	<i>IL-9.5</i>	<i>IL-9.5</i>	<i>SMA-9.5</i>	<i>IL-9.5FG</i>	<i>IL-9.5</i>	<i>SMA-9.5</i>	<i>SMA-12.5</i>	<i>SMA-9.5</i>
	Binder	<i>IL-4.75</i>	<i>IL-9.5FG</i>	<i>IL-4.75</i>	<i>IL-4.75</i>	<i>IL-19</i>	<i>SMA-12.5</i>	<i>IL-19</i>	<i>IL-9.5</i>
1	Surface	\$91.2	\$91.2	\$100.8			\$100.8	\$108.8	\$100.8
	Binder	\$89.8		\$89.8	\$89.8	\$63.5	\$108.8	\$63.5	
2	Surface	\$72.8	\$72.8		\$71.4				
	Binder	\$110.0	\$71.4	\$110.0	\$110.0				
3	Surface	\$85.1	\$85.1		\$85.4	\$79.4		\$123.0	
	Binder		\$85.4			\$80.7	\$123.0	\$80.7	\$79.4
4	Surface			\$116.8			\$116.8	\$111.0	\$116.8
	Binder	\$117.8		\$117.8	\$117.8	\$113.3	\$111.0	\$113.3	
5	Surface				\$73.0			\$129.2	
	Binder	\$118.5	\$73.0	\$118.5	\$118.5		\$129.2		
6	Surface					\$526.3			
	Binder								\$526.3
7	Surface				\$80.5	\$99.6		\$119.5	
	Binder		\$80.5			\$87.1	\$119.5	\$87.1	\$99.6
8	Surface	\$90.6	\$90.6		\$93.2	\$93.6			
	Binder		\$93.2			\$89.5		\$89.5	\$93.6
9	Surface	\$88.2	\$88.2		\$91.5	\$110.4			
	Binder		\$91.5			\$71.7		\$71.7	\$110.4
Avg.	Surface	\$85.6	\$85.6	\$108.8	\$82.5	\$95.8	\$108.8	\$118.3	\$108.8
	Binder	\$109.0	\$82.5	\$109.0	\$109.0	\$84.3	\$118.3	\$84.3	\$95.8

* Mix type used in the different scenarios for interstates and non-interstates.

LIFE-CYCLE COST ANALYSIS

IDOT has used LCCA to evaluate and select pavement type (PCC or HMA) on new construction and replacement projects for many years. Past LCCAs for pavements considered the actual project length and lane numbers with a 12 ft (3.7 m) average lane width. A 45-year analysis period was used by IDOT to compare jointed concrete and full-depth HMA pavements. The analysis period includes the updated performance of some materials and treatments as well as future maintenance and major rehabilitation projects. Salvage value and user costs were excluded from IDOT's LCCA calculations. A

similar approach was adopted in this project. The methodology and assumptions are introduced below.

LCCA Assumptions and Considerations

Evaluation Methods

Numerous economic analysis methods can be used to evaluate pavement alternatives. The present worth (PW) method and the equivalent uniform annual cost (EUAC) method are the most common. The EUAC method describes the average cost an agency pays per year over the analysis period. All costs, including initial construction and future maintenance, are distributed evenly.

Initial Costs

The initial cost accounts for a significant portion of the EUAC over the analysis period. The initial cost is determined at year 0 of the analysis period. Although numerous activities are performed during construction, reconstruction, or rehabilitation, only those specific to a pavement alternative were included in the initial costs. Actions dependent on pavement type include, but are not limited to, milling, pavement removal, HMA paving, PCC paving, and fracturing PCC slabs.

The only two costs included in the initial cost are pavement patches and HMA overlay. The calculations herein did not include other activities because cost analysis was performed on hypothetical scenarios. Hence, the same activities in overlay alternatives were omitted.

LCCAs for pavements considered a 12 ft (3.7 m) surface width and 1 lane mile. The following assumptions were used to perform LCCA:

- Project length = 1 mile
- Number of lanes = 1
- Average lane width = 12 ft
- No centerline lanes
- No edge lanes
- Surface and binder course standard weights: 112.0 lb/yd²in

Figure 83 presents the average lane-mile cost for various overlay scenarios in Illinois. For pavement patches, \$150 for the average unit cost and 4% patching were assumed. In addition, the initial cost of a lane mile for each of the 130 projects was calculated using the bidding unit cost provided for each project. Except for interstate alternatives 1 and 2, the initial costs for overlay options are around the initial cost average value of the analyzed 130 projects. Both alternatives have a greater thickness than the other overlay options.

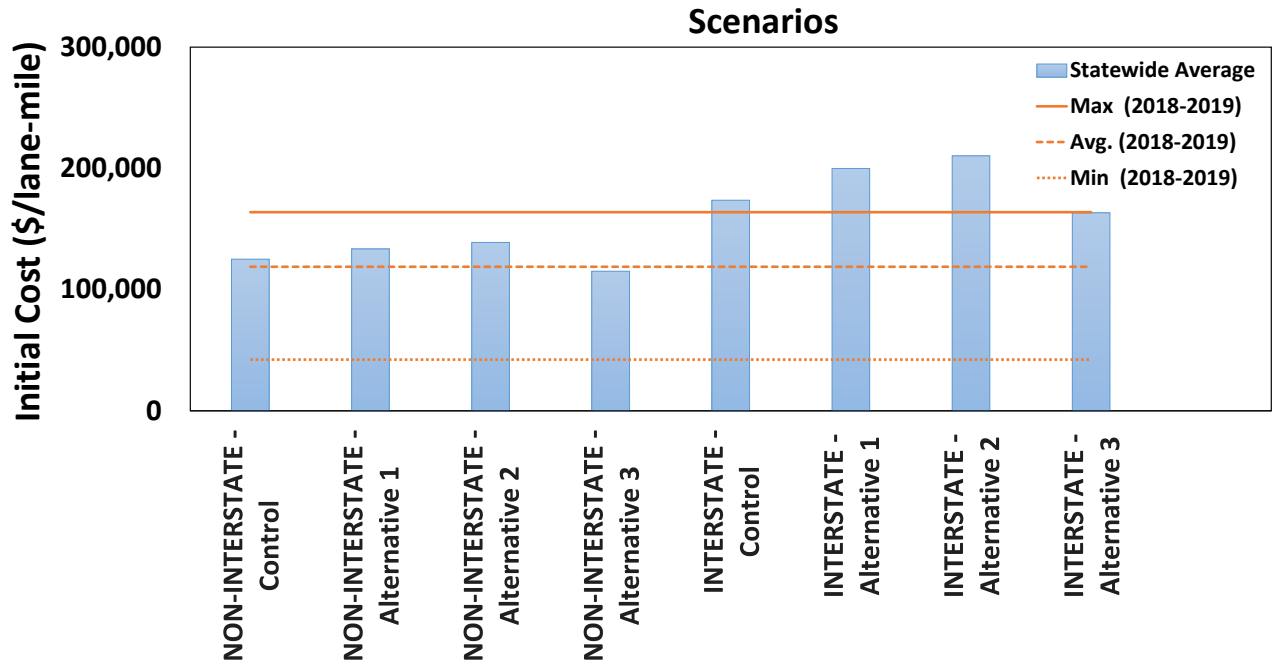


Figure 83. Chart. Initial cost of considered alternatives and statewide average as well as maximum, average, and minimum initial costs for provided projects.

Discount Rate

The time value of money must be considered to account for the cost related to future activities. In LCCA, the discount rate—the difference between interest and inflation rate—was used. Historically, this value has ranged from 2% to 5%. In this study, a value of 3% was used, which is consistent with the value IDOT uses in LCCA. The discount rate accounts not only for the increased cost associated with performing an activity in the future, but also for the economic benefit the agency would receive if those funds were invested in an interest-bearing account.

Analysis Period

LCCA periods should be sufficiently long to reflect long-term differences associated with reasonable maintenance strategies and long enough to incorporate at least one complete cycle of rehabilitation activity. The analysis period should generally be longer than the pavement design period. The three scenarios considered are listed below and demonstrated in Table 20:

- Poor performance: Overlay service life was assumed 10–11 years and was maintained at 3 and 6 years.
- Moderate performance: Overlay service life was assumed 12–13 years and was maintained at 4 and 8 years.
- Good performance: Overlay service life was assumed 14–15 years and was maintained at 5 and 10 years.

Table 20. Three Considered Scenarios for LCCA

Criterion	Poor (Years)	Moderate (Years)	Good (Years)
Overlay Service Life	10–11	12–13	14–15
Year 1st Maintenance is Applied	3	4	5
Year 2nd Maintenance is Applied	6	8	10

Maintenance Costs

Pavement requires routine preventive and corrective maintenance during its service life. The timing and extent of these activities vary. Maintenance costs were estimated from IDOT’s LCCA database for three performance scenarios (poor, moderate, and good). Only general routine maintenance per lane-mile cost data is usually available. The costs for following routine HMA surface maintenance were included in the analysis: (i) rout and sealing random cracks (R&S), (ii) rout and sealing reflective transverse cracks, (iii) partial depth (PD) of pavement patches and (iv) milling and filling (M&F). Table 21 illustrates typical initial and maintenance unit prices and cost calculations.

Life-Cycle Cost Analysis of Overlay Scenarios

Two analysis approaches were followed: direct comparison of annual costs of overlay scenarios based on experimental results presented in Chapter 3 and sensitivity analysis by assigning a service life range to each scenario.

LCCA Based on the Large-Scale Test Performance Ranking

Table 22 presents the ranking of overlay alternatives based on the large-scale testing results. The number of cycles to failure and other performance parameters were considered to estimate the life for each overlay alternative. A service life of 10 years was assigned to the control alternatives, while best-performing alternatives were assumed to last 14 years until the subsequent major rehabilitation. Because service lives were only estimated at this stage, a sensitivity analysis was performed and presented at the end of this chapter. Table 22 and Figure 84 present the estimated annual cost per mile (\$/Yr) using statewide average unit prices and anticipated service lives. Alternatives 2 and 3 had the lowest annual cost per mile among non-interstate cases, while alternative 2 was the most cost-effective among interstate cases.

Table 21. Initial and Maintenance Costs Per IDOT’s Chapter 54 Manual and Templates

	Year	INTERSTATE					
Initial Construction	0	PAVEMENT PATCH CLASS B	4.00%	282	SQ YD	\$150.00	\$42,300
		HMA OVERLAY 3.5" (PVMT)	100.00%	1,380	TON	\$105.37	\$145,396
		PWF _n * = 1.0000		PW** = 1.0000		X	\$187,696
		INTERSTATE					
1 st Maintenance		RANDOM CRACK R&S	50.00%	2,640	LIN FT	\$2.00	\$5,280
		REFLECTIVE TRANSVERSE CRACK R&S	40.00%	1,690	LIN FT	\$2.00	\$3,380
		PD PVMT PATCH M&F HMA SURF 1.50"	0.10%	7	SQ YD	\$78.47	\$549
		3	PWF _n = 0.9151	PW = 0.9151	X	\$9,209	
	4	PWF _n = 0.8885	PW = 0.8885	X	\$9,209		
	5	PWF _n = 0.8626	PW = 0.8626	X	\$9,209		
		INTERSTATE					
2 nd Maintenance		PAVEMENT PATCH CLASS B	0.50%	35	SQ YD	\$150.00	\$5,250
		REFLECTIVE TRANSVERSE CRACK R&S	60.00%	2,534	LIN FT	\$2.00	\$5,068
		RANDOM CRACK R&S	50.00%	2,640	LIN FT	\$2.00	\$5,280
		PD PVMT PATCH M&F HMA SURF 1.50"	0.50%	35	SQ YD	\$78.47	\$2,746
	6	PWF _n = 0.8375	PW = 0.8375	X	\$18,344		
	8	PWF _n = 0.7894	PW = 0.7894	X	\$18,344		
	10	PWF _n = 0.7441	PW = 0.7441	X	\$18,344		

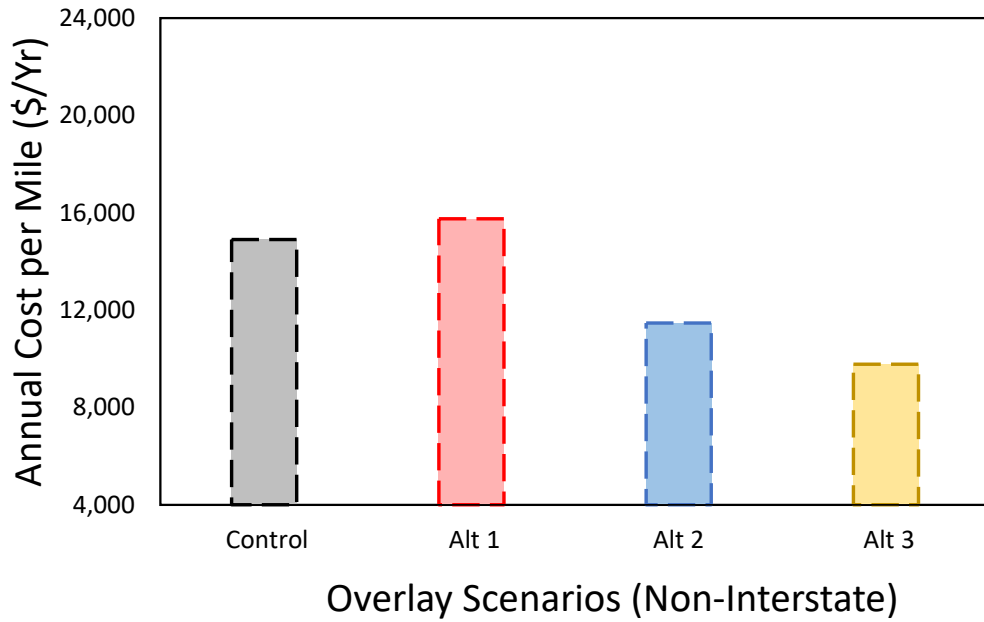
$$* PWF_n = \left(\frac{1}{1 + \frac{\text{Discount Rate}}{100}} \right)^{(\text{Year } y - \text{Base year})}$$

* PWF_n: Present Worth factor. Used in reducing the cost to Net Present Worth for each year.

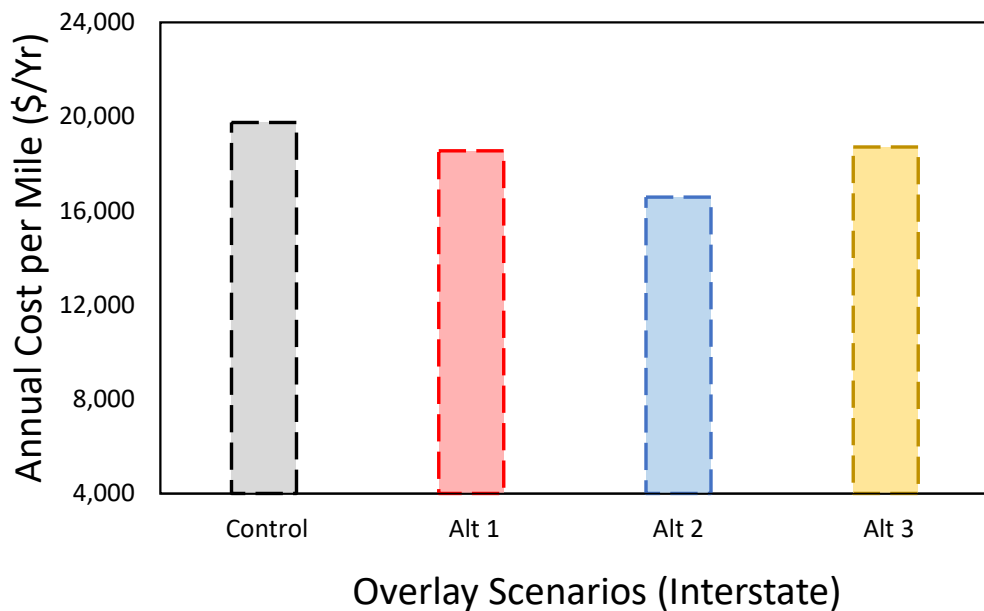
** PWF_n: Present Worth for each year.

Table 22. Annual Cost Per Mile (\$/Yr) for Considered Overlay Alternatives

Classification		Surface Course	Binder Course	Initial Cost Per Mile (\$/Yr)	Number of Cycles to Failure	Assumed Service Life (Years)	Annual Cost Per Mile (\$/Yr)
Non-Interstate	Control	1.5" IL-9.5	0.75" IL-4.75	125,150	14,600	10	14,902
	Alt 1	1.5" IL-9.5	1.25" IL-9.5FG	133,576	14,600	10	15,754
	Alt 2	1.5" SMA-9.5	0.75" IL-4.75	138,869	69,850	14	11,474
	Alt 3	1.25" IL-9.5FG	0.75" IL-4.75	115,185	111,500	14	9,772
Interstate	Control	1.5" IL-9.5	2.25" IL-19.0	173,730	9,700	10	19,751
	Alt 1	1.5" SMA-9.5	2.0" SMA-12.5	199,917	16,200	12	18,550
	Alt 2	2.0" SMA-2.5	2.25" IL-19.0	210,355	23,700	14	16,579
	Alt 3	1.5" SMA-9.5	1.5" IL-9.5	163,292	10,200	10	18,711



A. Non-Interstate



B. Interstate

Figure 84. Chart. Annual cost per mile (\$/Yr) for considered overlay alternatives: (a) non-interstate and (b) interstate.

Sensitivity Analysis

Multiple variables affect the final EUAC for pavement alternatives. Significant factors influencing the LCCA results are unit cost, analysis period, and timing of activities. Therefore, cost sensitivity to each

variable should be assessed. Cost sensitivity is accomplished by performing a limited sensitivity analysis whereby various combinations of inputs are selected to qualify their effect on the analysis results. For a hypothetical overlay service life between 10 to 15 years, the life-cycle cost and annual cost per mile were estimated.

Table 23 and Figure 85 present the life-cycle cost results for interstate and non-interstate control alternatives. The estimation reflects the highest annual cost per mile for a 10-year performance period. Then, the annual cost estimates are reduced by about 17% and 30% for an improvement of service life by two and four years, respectively.

Table 23. Life-Cycle Cost for Control of Interstate and Non-interstate (Statewide Average)

Service Life Estimate	Life-Cycle Cost (per lane-mile)		Annual Life-Cycle Cost (per lane-mile)	
	Interstate (control)	Non-Interstate (control)	Interstate (control)	Non-Interstate (control)
10	\$223,732	\$149,023	\$19,751	\$14,902
11	\$223,732	\$149,023	\$17,955	\$13,548
12	\$222,604	\$147,891	\$16,365	\$12,324
13	\$222,604	\$147,891	\$15,106	\$11,376
14	\$221,533	\$146,818	\$13,951	\$10,487
15	\$221,533	\$146,818	\$13,021	\$9,788

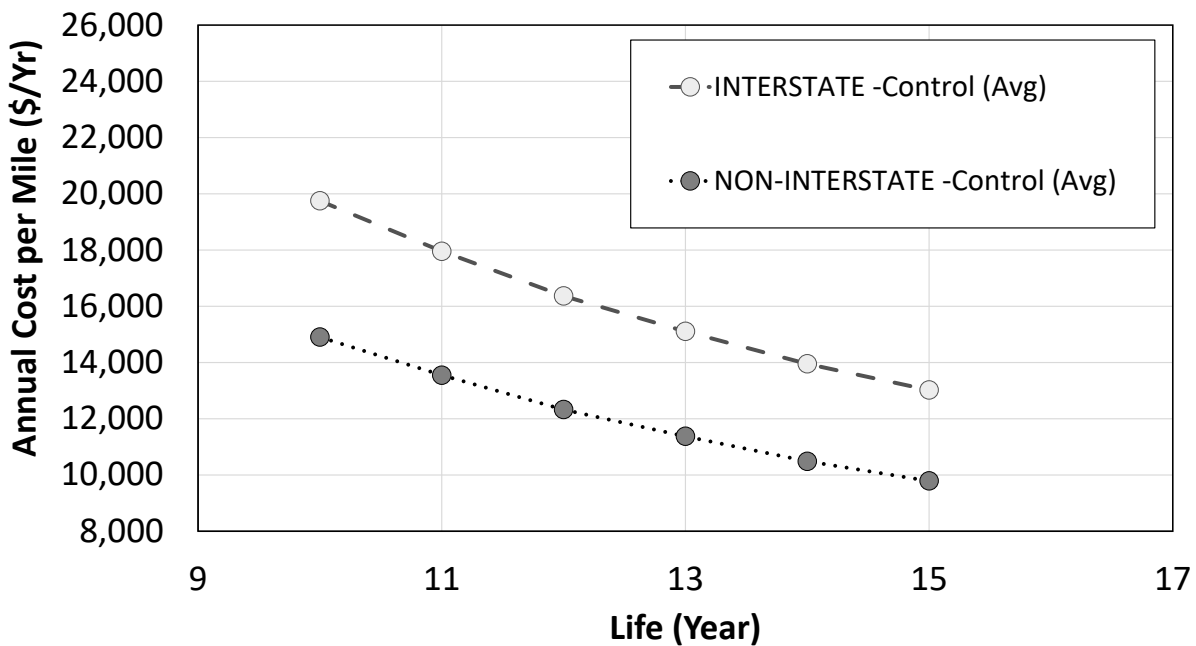


Figure 85. Chart. Annual cost per mile for control of interstate and non-interstate (statewide average).

The same approach was followed for the other alternatives. LCCA and the annual cost per mile of all overlay alternatives included in this project’s experimental program were estimated. Statewide average unit prices were used in the analysis. Figure 86 illustrates the life-cycle cost results of non-interstate alternatives, and Figure 87 illustrates the hypothetical comparison of interstate overlay alternatives. A cut-off lifetime is identified where the annual cost of the alternative is equal to the cost of the control. Compared to the control, an alternative lasts longer than the cut-off lifetime (green-shaded region), and additional investment due to an increase in the initial costs is compensated. Otherwise, a service lifetime increase is insufficient to justify the additional investment (orange-shaded region). The following interpretations may be offered based on the comparisons.

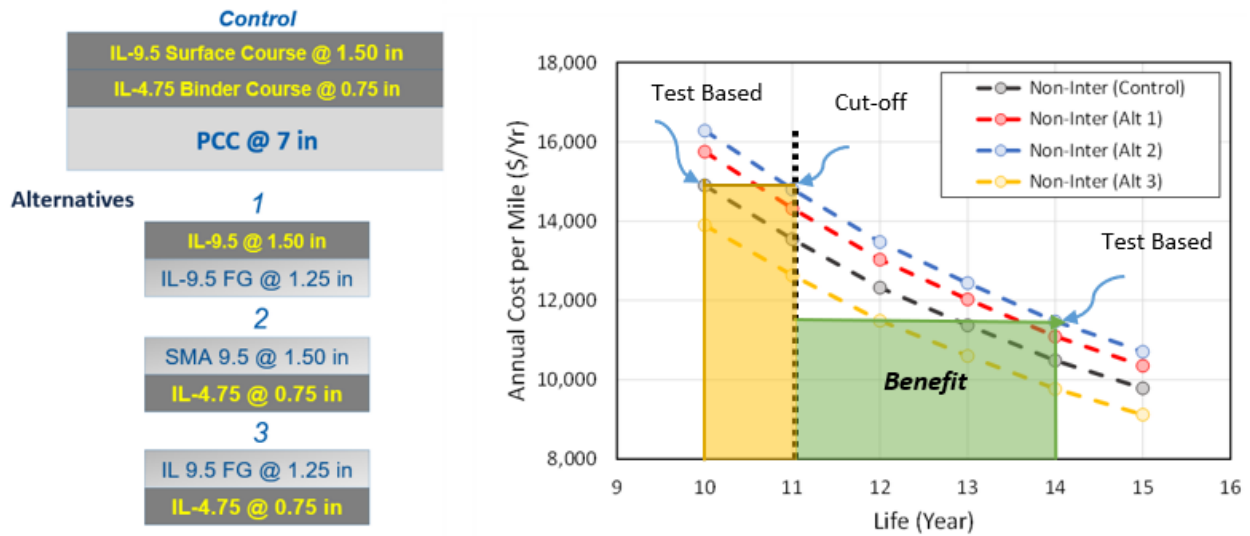


Figure 86. Chart. Hypothetical comparison of overlay alternatives (non-interstate).

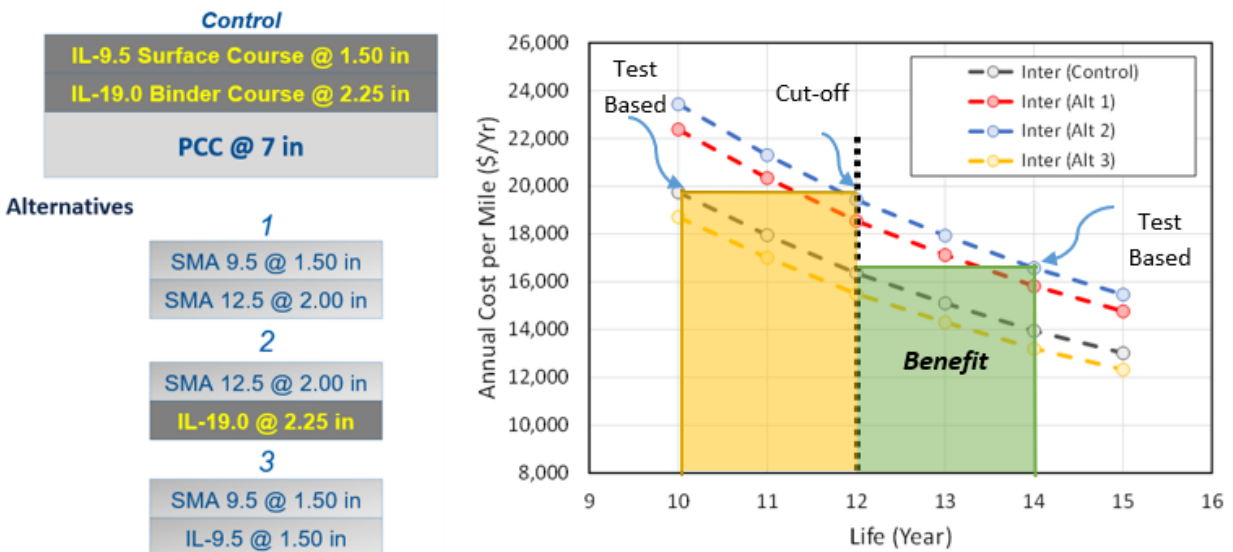


Figure 87. Chart. Hypothetical comparison of overlay alternatives (interstate).

For non-interstate alternatives, assuming the control overlay service life expectancy is 10 years:

- The higher-cost alternative 2 (due to extra thickness) could be cost-effective if its service life is increased by one year.
- A less costly option, alternative 3 (due to lower thickness), could be cost-effective if its service life is not shortened by one year or more.
- Alternatives 2 and 3 could be the most cost-effective if their service lives increased by more than 4 years. The annual cost estimates would be reduced by 23% and 34%, respectively.

For interstate alternatives:

- Assuming the control service life is 10 years, alternative 2 (due to greater thickness and use of SMA) would be 20% more expensive than the control option. However, it must enhance pavement service life by more than two years to be cost-effective. Using alternative 2 to improve service life by four years would reduce annual cost estimates by about 16%.
- Although a higher quality material, alternative 3 costs 7% less (due to lower thickness).

SUMMARY

Life-cycle cost analyses of overlay alternatives were performed using IDOT's unit prices from contracts between 2018 and 2019. Service lives of 10, 12, and 14 years were assigned to poor-, moderate-, and good-performance scenarios, respectively. Overlay alternative 2 (1.5 in SMA-9.5 surface and 0.75 in IL-4.75 binder) and alternative 3 (1.25 in IL-9.5FG surface and 0.75 in IL-4.75 binder) had the lowest annual cost per mile among non-interstates, while overlay alternative 2 (2 in SMA-12.5 surface and 2.25 in IL-19.0) was the most cost-effective among interstate cases. In addition, a hypothetical scenario-based sensitivity analysis was performed. The cost-effectiveness of each alternative was compared to the control overlay strategy based on a range of expected service lives. Cut-off lifetimes were identified where the annual cost of the alternative was equal to that of the control.

CHAPTER 6: SUMMARY, FINDINGS, AND RECOMMENDATIONS

SUMMARY

For moderately deteriorated PCC pavement, resurfacing with HMA overlays is an efficient and common rehabilitation practice. The service life of HMA overlays plays a vital role in the pavement network's overall structural and functional health. Reflective cracking is the most common distress observed in HMA overlays. Because of discontinuities (e.g., joints and cracks) in existing PCC pavement, reflective cracks may develop shortly after resurfacing. This project focused on optimizing HMA mix and thickness selection to mitigate reflective cracking of HMA overlays. The outcomes would support IDOT in reviewing specifications and policies to implement a performance-based approach for HMA overlays and corresponding lift configurations.

Large-scale laboratory tests were conducted to assess the combined impact of HMA overlay mix and thickness on its performance to control reflective cracking. A testing device using two actuators was designed and built in-house to simulate a real-world truckload. Eight tests were conducted to evaluate a wide range of mix and thickness combinations. The Illinois Flexibility Index Test, Hamburg wheel-tracking test, and dynamic modulus test were performed to characterize each HMA mix for cracking potential, rutting potential, and dynamic modulus, respectively. By analyzing instrumentation data and correlating large-scale tests, given that minimum HMA densities were met, the layer interface bonding efficiency, flexibility, stiffness of HMA mixes, and layer thickness were found to affect overlays' performance significantly against reflective cracking. To delay failure, interlayer bonding should be properly achieved with existing pavement and between lifts to reduce joint opening and delays in debonding. An overlay comprised of a high modulus and flexible surface course, and a flexible binder course has superior performance to control reflective cracking. Besides, the thicker the HMA overlay, the enhanced resistance to reflective cracking, given that other parameters are unchanged. Moreover, optimal overlay configurations to control reflective cracking were identified. For non-interstate scenarios, it is recommended to use an overlay with an SMA-9.5 surface course and an IL-4.75 binder course. An IL-9.5FG surface course and an IL-4.75 binder course are suggested for low-volume and low-speed roads. For interstate scenarios, it is recommended to use an overlay comprised of an SMA-12.5 surface course and an IL-19.0 binder course. An SMA-9.5 surface course and an SMA-12.5 binder course are suggested when a thin structure is required.

Large-scale testing is time-consuming and expensive. Hence, it is impractical to test all possible scenarios. Therefore, a generalized 3D FE model was developed to predict reflective cracking potential for new configurations. Fracture properties such as SIF and J-integral were modeled and computed. A crack front region with a crack tip and seam was assigned to both the surface and binder course. Mesh sensitivity analysis was performed to ensure reliability with optimal running time. Average Mode I SIF was found to be a valid measure to assess overlays' reflective cracking potential. Moreover, a data-driven surrogate model that predicts reflective cracking potential was developed to allow easy application of the model by agencies. A database of 128 cases was generated to compute fracture parameters for extreme scenarios or a combination of inputs. SHAP analysis confirmed the model's robustness. Engineers can easily use the surrogate model when selecting HMA mixtures and design thicknesses.

Life-cycle cost analyses of the overlay alternatives were performed using IDOT's unit prices from contracts between 2018 and 2019. The experimental results were considered to estimate a lifetime for each overlay scenario. Services lives of 10, 12, and 14 years were assigned to poor-, moderate-, and good-performance scenarios, respectively. An overlay comprised of a 1.5 in (38.1 mm) SMA-9.5 or 1.25 in (31.8 mm) IL-9.5FG surface course and a 0.75 in (19.1 mm) IL-4.75 binder course had the lowest annual cost per mile among non-interstates scenarios. For interstate scenarios, an overlay comprised of a 2.0 in (50.8 mm) SMA-12.5 surface course and a 2.25 in (57.2 mm) IL-19.0 binder course was the most cost-effective. In addition, a sensitivity analysis was performed where the cost-effectiveness of each scenario was compared to the control overlay strategy based on a range of expected service lives. Cut-off lifetimes were identified where the annual cost of the alternative scenario was equal to the cost of the control.

MAJOR FINDINGS

The major findings of this project are summarized below:

- Significant joint opening, caused by low bonding efficiency at the binder–PCC interface, induced rapid failure of HMA overlays.
- Debonding at the binder–PCC interface substantially affected crack initiation. Delayed debonding would cause slowed crack initiation, resulting in delayed failure. In addition, if one of the HMA layers was polymer-modified while the other was not, significant debonding would occur at the surface–binder interface, impacting crack propagation.
- An optimum overlay to control reflective cracking is generally comprised of a high modulus and flexible surface course as well as a flexible binder course. Moreover, the thicker the HMA overlay, the enhanced resistance to reflective cracking.
- Mode I cracking (i.e., tensile cracking) is the 3D FE model's dominant mechanism for crack propagation. Average KI is a valid measure to rank the overlay's reflective cracking potential. The developed data-driven surrogate model is robust and can be used to select mixtures and design thicknesses.
- Overlays with premium mixes or extra thickness could be cost-effective if service life can be improved by two or more years, such as alternatives 2 and 3 for the non-interstate scenario and alternative 2 for the interstate scenario.

RECOMMENDATIONS

To control reflective cracking and reduce life-cycle cost, an overlay comprised of an SMA-9.5 surface course and an IL-4.75 binder course is recommended for non-interstate projects. An IL-9.5FG surface course and an IL-4.75 binder course are suggested for low-volume and low-speed roads. For interstate projects, an overlay comprised of an SMA-12.5 surface course and an IL-19.0 binder course is recommended. Please note that the recommendations assume that these mixtures are available and can be produced in all geographical regions of Illinois. A data-driven surrogate model was developed to assist engineers in designing thicknesses. Moreover, to mitigate reflective cracking, it is

crucial to ensure HMA mixtures have an acceptable flexibility index, to apply polymer modification to all layers, to increase HMA–PCC bonding efficiency, to ensure densities are met, and to treat deteriorated PCC joints/cracks.

REFERENCES

- AASHTO T 324. (2019). *Standard method of test for Hamburg wheel-track testing of compacted asphalt mixtures*. American Association of State Highways and Transportation Officials.
- AASHTO T 342. (2011). *Standard method of test for determining dynamic modulus of hot mix asphalt (HMA)*. American Association of State Highways and Transportation Officials.
- AASHTO T 393. (2022). *Standard method of test for determining the fracture potential of asphalt mixtures using the Illinois flexibility index test (I-FIT)*. American Association of State Highways and Transportation Officials.
- Abaqus, S., Fallis, A. D. S., & Techniques, D. (2014). ABAQUS analysis user's guide (6.14). *Dassault Systemes Simulia Corp., Providence*.
- Aliha, M. R. M., Ziari, H., Mojaradi, B., & Sarbijan, M. J. (2020). Modes I and II stress intensity factors of semi-circular bend specimen computed for two-phase aggregate/mastic asphalt mixtures. *Theoretical and Applied Fracture Mechanics*, 106, 102437.
- Al-Qadi, I. L., Carpenter, S. H., Leng, Z., Ozer, H., & Trepanier, J. (2009). *Tack coat optimization for HMA overlays: Accelerated pavement test report*. FHWA-ICT-09-035.
- Al-Qadi, I. L., Hasiba, K. I., Salinas Cortina, A., Ozer, H., Leng, Z., Parish, D. C., & Worsfold, S. J. (2012). *Best practices for implementation of tack coat: PART I-Laboratory study* (Report No. FHWA-ICT-12-004). Illinois Center for Transportation.
- Al-Qadi, I. L., Ozer, H., Lambros, J., El Khatib, A., Singhvi, P., Khan, T., ... & Doll, B. (2015). *Testing protocols to ensure performance of high asphalt binder replacement mixes using RAP and RAS* (Report No. FHWA-ICT-15-017). Illinois Center for Transportation.
- Al-Qadi, I. L., Ozer, H., Zhu, Z., Singhvi, P., Mohamed Ali, U., Sawalha, M., ... & Zehr, T. G. (2019). *Development of long-term aging protocol for implementation of the Illinois flexibility index test (I-FIT)* (Report No. FHWA-ICT-19-009). Illinois Center for Transportation.
<https://doi.org/10.36501/0197-9191/19-012>
- Ameri, M., Mansourian, A., Khavas, M. H., Aliha, M., & Ayatollahi, M. R. (2011). Cracked asphalt pavement under traffic loading—A 3D finite element analysis. *Engineering Fracture Mechanics*, 78(8), 1817-1826.
- Baek, J. (2010). *Modeling reflective cracking development in hot-mix asphalt overlays and quantification of control techniques*. University of Illinois at Urbana-Champaign.
- Baek, J., & Al-Qadi, I. L. (2006). Finite element method modeling of reflective cracking initiation and propagation: Investigation of the effect of steel reinforcement interlayer on retarding reflective cracking in hot-mix asphalt overlay. *Transportation Research Record*, 1949(1), 32–42.
- Baek, J., & Al-Qadi, I. (2009). Reflective cracking: Modeling fracture behavior of hot-mix asphalt overlays with interlayer systems. *Asphalt Paving Technology-Proceedings*, 28, 789.
- Baek, J., & Al-Qadi, I. L. (2011). Sand mix interlayer to control reflective cracking in hot-mix asphalt overlay. *Transportation Research Record*, 2227(1), 53–60.

- Baek, J., Ozer, H., Wang, H., & Al-Qadi, I. L. (2010). Effects of interface conditions on reflective cracking development in hot-mix asphalt overlays. *Road Materials and Pavement Design*, 11(2), 307–334.
- Bennert, T., & Maher, A. (2008). Field and laboratory evaluation of a reflective crack interlayer in New Jersey. *Transportation Research Record*, 2084(1), 114–123.
- Bennert, T., Worden, M., & Turo, M. (2009). Field and laboratory forensic analysis of reflective cracking on Massachusetts Interstate 495. *Transportation Research Record*, 2126(1), 27–38.
- Bonaquist, R. F. (2011). *Precision of the dynamic modulus and flow number tests conducted with the asphalt mixture performance tester* (Vol. 702). National Academies of Sciences, Engineering, and Medicine.
- Dave, E. V., & Buttlar, W. G. (2010). Thermal reflective cracking of asphalt concrete overlays. *International Journal of Pavement Engineering*, 11(6), 477–488.
- Dave, E. V., Ahmed, S., Buttlar, W. G., Bausano, J., & Lynn, T. (2010). Investigation of strain tolerant mixture reflective crack relief systems: An integrated approach. *Asphalt Paving Technology- Proceedings Association of Asphalt Technologists*, 79, 119.
- De Bondt, A. H. (2000). *Anti-reflective cracking design of (reinforced) asphaltic overlays*. Delft University of Technology.
- Elseifi, M. A., & Al-Qadi, I. L. (2004). A simplified overlay design model against reflective cracking utilizing service life prediction. *Road Materials and Pavement Design*, 5(2), 169–191.
- Elseifi, M. A., Bandaru, R., Zhang, Z., & Ismail, S. (2011). Field evaluation and cost-effectiveness of saw and seal method to control reflection cracking in composite pavements. *Transportation Research Record*, 2227(1), 33–42.
- Dave, E. (2009). *Asphalt pavement aging and temperature dependent properties using functionally graded viscoelastic model*. PhD Dissertation, University of Illinois at Urbana-Champaign.
- Francken, L., & Vanelstraete, A. (1992). Interface systems to prevent reflective cracking: Modelling and experimental testing methods. In *International Conference on Asphalt Pavements, 7th, 1992, Nottingham, United Kingdom* (Vol. 1).
- Geoffroy, D. N. (1998). *Thin-surfaced pavements*. Transportation Research Board.
- Hu, S., Zhou, F., & Scullion, T. (2010). Reflection cracking–based asphalt overlay thickness design and analysis tool. *Transportation Research Record*, 2155(1), 12–23.
- Huang, Y. H. (2004). *Pavement analysis and design*. Pearson.
- Jayawickrama, P. W., Smith, R. E., Lytton, R. L., & Tirado, M. R. (1987). *Development of asphalt concrete overlay design equations, Vol. I—Development of design procedures* (Report No. FHWA/RD-86). Federal Highway Administration.
- Keenan, C., Sprung, M. J., Strocko, E., Schmitt, R. R., Rick, C., & Sedor, J. (2012). *Freight facts and figures 2012* (Report No. FHWA-HOP-13-001). Federal Highway Administration.
- Kuo, C. M., & Hsu, T. R. (2003). Traffic induced reflective cracking on pavements with geogrid-reinforced asphalt concrete overlay. In *Proceedings of the 82th Annual Meeting at the*

Transportation Research Board (CD-ROM).

- Ling, J., Tao, Z., Qian, J., & Fu, W. (2018). Investigation the influences of geotextile on reducing the thermal reflective cracking using XFEM. *International Journal of Pavement Engineering*, 19(5), 391–398.
- Lundberg, S. M., & Lee, S. I. (2017). A unified approach to interpreting model predictions. *Advances in Neural Information Processing Systems*, 30.
- Lytton, R. L. (1989). Use of geotextiles for reinforcement and strain relief in asphalt concrete. *Geotextiles and Geomembranes*, 8(3), 217–237.
- Lytton, R. L., Tsai, F. L., Lee, S. I., Luo, R., Hu, S., & Zhou, F. (2010). *Models for predicting reflection cracking of hot-mix asphalt overlays* (No. Project 01-41).
- Maurer, D. A., & Malasheskie, G. J. (1989). Field performance of fabrics and fibers to retard reflective cracking. *Geotextiles and Geomembranes*, 8(3), 239–267.
- Minhoto, M. J., Pais, J. C., & Pereira, P. A. (2008). The temperature effect on the reflective cracking of asphalt overlays. *Road Materials and Pavement Design*, 9(4), 615–632.
- NCHRP 1-37A. (2004). Mechanistic-empirical design of new and rehabilitated pavement structures. <https://store.transportation.org/Item/CollectionDetail?ID=196>
- Newcomb, D. E. (2009). *Thin asphalt overlays for pavement preservation* (No. Information Series 135).
- Newman Jr, J. C., James, M. A., & Zerbst, U. (2003). A review of the CTOA/CTOD fracture criterion. *Engineering Fracture Mechanics*, 70(3-4), 371-385.
- Ozer, H., Al-Qadi, I. L., Lambros, J., El-Khatib, A., Singhvi, P., & Doll, B. (2016a). Development of the fracture-based flexibility index for asphalt concrete cracking potential using modified semi-circle bending test parameters. *Construction and Building Materials*, 115, 390–401.
- Ozer, H., Al-Qadi, I. L., Singhvi, P., Khan, T., Rivera-Perez, J., & El-Khatib, A. (2016b). Fracture characterization of asphalt mixtures with high recycled content using Illinois semicircular bending test method and flexibility index. *Transportation Research Record*, 2575(1), 130–137.
- Perez, S. A., Balay, J. M., Tamagny, P., & Petit, C. (2007). Accelerated pavement testing and modeling of reflective cracking in pavements. *Engineering Failure Analysis*, 14(8), 1526–1537.
- Rahman, F., Hossain, M., Romanoschi, S. A., & Hobson, C. (2011). Experience with thin Superpave mixture overlay of small aggregate top size in Kansas. *Transportation Research Record*, 2205(1), 3–10.
- Rice, J. R. (1968). A Path Independent Integral and the Approximate Analysis of Strain Concentration by Notches and Cracks. *ASME. J. Appl. Mech. June 1968*; 35(2): 379 - 386.
- Rith, M., & Lee, S. W. (2022). Development of cohesive-zone-based prediction model for reflective cracking in asphalt overlay. *International Journal of Pavement Engineering*, 23(4), 1050–1059.
- Salinas, A., Al-Qadi, I. L., Hasiba, K. I., Ozer, H., Leng, Z., & Parish, D. C. (2013). Interface layer tack coat optimization. *Transportation research record*, 2372(1), 53-60.
- Schaperly, R. A. (1984). Correspondence principles and a generalized J integral for large deformation and fracture analysis of viscoelastic media. *International journal of fracture*, 25, 195-223.

- Sha, Q. L. (1993). Two kinds of mechanism of reflective cracking. In *RILEM PROCEEDINGS* (pp. 441–441). Chapman & Hall.
- Son, S., & Al-Qadi, I. L. (2014). Engineering cost–benefit analysis of thin, durable asphalt overlays. *Transportation Research Record, 2456*(1), 135–145.
- Son, S., Al-Qadi, I. L., & Zehr, T. (2016). 4.75 mm SMA performance and cost-effectiveness for asphalt thin overlays. *International Journal of Pavement Engineering, 17*(9), 799–809.
- Sousa, J., Pais, J., Saim, R., Way, G., & Stubstad, R. (2001). Development of a mechanistic overlay design method based on reflective cracking concepts. *Final report for Rubber Pavements Association, Consulpav International*.
- US Department of Transportation. (2021). 24th Edition *Status of the nation’s highways, bridges, and transit: Conditions and performance: report to the congress*. <https://www.fhwa.dot.gov/policy/24cpr/>
- Wang, X., & Zhong, Y. (2019). Influence of tack coat on reflective cracking propagation in semi-rigid base asphalt pavement. *Engineering Fracture Mechanics, 213*, 172–181.
- Wang, X., Li, K., Zhong, Y., Xu, Q., & Li, C. (2018). XFEM simulation of reflective crack in asphalt pavement structure under cyclic temperature. *Construction and Building Materials, 189*, 1035–1044.
- Watson, D. E., & Heitzman, M. (2014). *Thin asphalt concrete overlays: A synthesis of highway practice*. National Cooperative Highway Research Program (NCHRP) Synthesis, 464.
- West, R., Rausch, R., & Takahashi, O. (2006). Refinement of mix design criteria for 4.75 mm superpave mixes. In *10th International Conference on Asphalt Pavements*, August 12–17, 2006, Quebec City, Canada.
- Williams, M. L., Landel, R. F. & Ferry, J. D. (1955). The temperature dependence of relaxation mechanisms in amorphous polymers and other glass-forming liquids. *Journal of the American Chemical Society, 77*(14), 3701–3707.
- Wu, Z., Hu, S., & Zhou, F. (2014). Prediction of stress intensity factors in pavement cracking with neural networks based on semi-analytical FEA. *Expert Systems with Applications, 41*(4), 1021–1030.
- Xie, P., & Wang, H. (2022). Finite element analysis of thermal-induced reflective cracking in composite pavement with mitigation strategies. *Engineering Fracture Mechanics, 266*, 108396.
- Xu, X., Cheng, X., Zhou, Z., & Xu, C. (2015). An analytical approach for the mixed-mode crack in linear viscoelastic media. *European Journal of Mechanics-A/Solids, 52*, 12–25.
- Yin, H. (2015). Full-scale test of thermally induced reflective cracking in airport pavements. *Road Materials and Pavement Design, 16*(1), 119–132.
- Yin, H., & Barbagallo, D. (2014). *Full-scale test of thermally-induced reflective cracking: Lessons learned from 5-year research at FAA NAPTF* (No. P10007).
- Zhou, F., Hu, S., Hu, X., Scullion, T., Mikhail, M., & Walubita, L. F. (2010). Development, calibration, and verification of a new mechanistic-empirical reflective cracking model for HMA overlay thickness design and analysis. *Journal of Transportation Engineering, 136*(4), 353–369.

APPENDIX A: SLAB PREPARATION

SUBGRADE PREPARATION

Fine sand material was sampled in Mahomet, Illinois. Figure 88 presents its gradation. It is classified as poorly graded sand (SP) based on the Unified Soil Classification System (ASTM D2487). A 12 in (305 mm) sand layer was placed in the testbed and was compacted by a vibratory compactor, as presented in Figure 89. To evaluate the uniformity of density, lightweight deflectometer (LWD) tests were performed at three sites according to ASTM E2835. Table 24 summarizes the results. An acceptable subgrade uniformity was achieved.

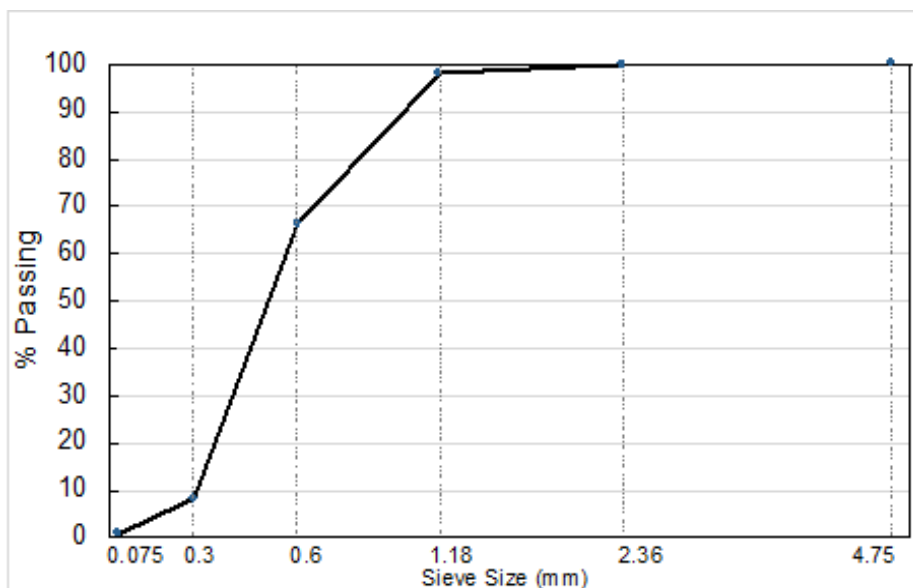


Figure 88. Chart. Gradation of the subgrade material.

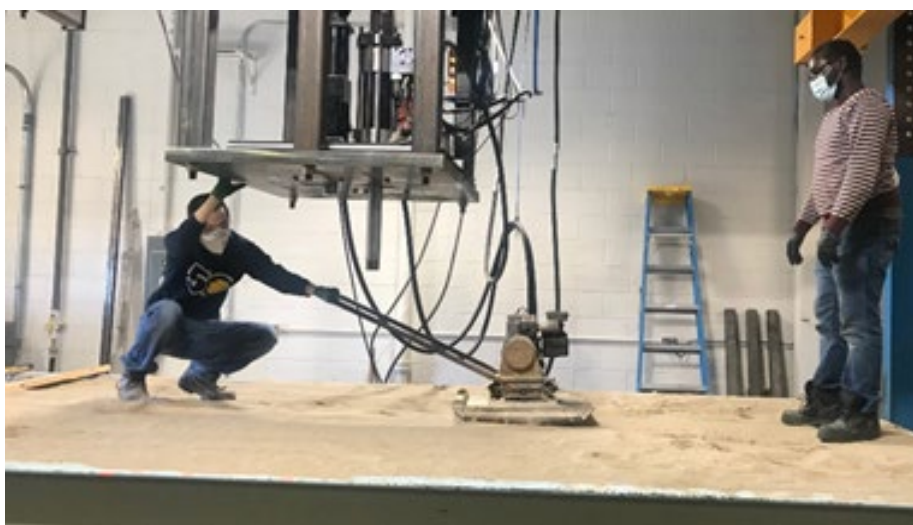


Figure 89. Photo. A vibratory compactor compacts the sand layer.

Table 24. Results of LWD Tests

Site No.	Mean Maximum Settlement (mm)	Impact Duration (ms)	Dynamic Modulus of Deformation (MPa)
1	0.893	3.655	25.20
2	0.766	3.493	29.37
3	0.991	4.035	22.70
Mean	0.883	3.728	25.76
Standard Deviation	0.113	0.278	3.370

CONCRETE SLAB PREPARATION

Slab Casting

A total of 13 wood forms were built to cast the slabs—each form measured 6 × 6 ft (1.8 × 1.8 m) square and 7 in (177.8 mm) thick. As presented in Figure 90, ferrule loops were installed to allow lifting and moving after casting.



Figure 90. Photo. Wood forms with ferrule loops.

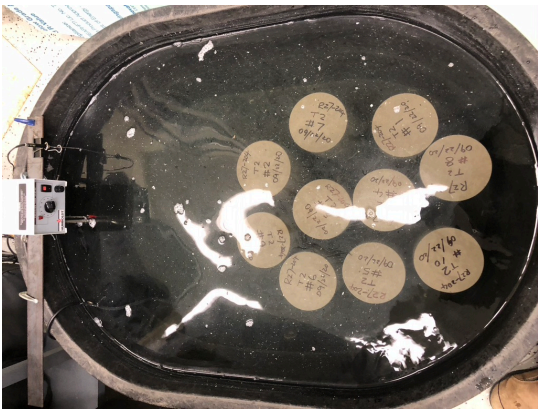
The slabs were constructed on Sep 22, 2020, in the early afternoon at the University of Illinois' Illinois Center for Transportation facility in Rantoul, Illinois. The National Weather Service reported a minimum temperature of 73°F (22.8°C) and a maximum of 75°F (23.9°C) during the construction period, with an average wind speed of 9 mph (14.5 km/h) and humidity of 49%. The day was predominantly sunny, with few clouds and no precipitation.

Two concrete trucks containing 7 yd of IDOT-approved PV-class concrete arrived in the order and at times specified in Table 25. The new properties presented in Table 25 were measured before placing the concrete in the forms. The temperature, slump, and air content were tested following ASTM C1064, AASHTO T119, and T152, respectively.

Table 25. Truck Arrival Time and Fresh Concrete Properties

Truck Number	Approximate Arrival Time	Temperature (°F)	Slump (in)	Air Content (%)
1	1:00 p.m.	75	4.50	4.5
2	2:00 p.m.	78	4.75	4.0

Ten cylinders with dimensions of 6 in (150 mm) diameter and 12 in (305 mm) height were made for each truck. After 24 hours, five cylinders from each truck were demolded and stored in lime-saturated water at 75°F (23.9°C) until testing (Figure 91-A), while the rest were stored in the field (Figure 91-B).



(a) Lab-cure in lime-saturated water



(b) Field-cure

Figure 91. Photo. Curing condition of concrete cylinders.

All slabs, excluding the last one, were filled with concrete in one pour (Figure 92-A), consolidated (Figure 92-B), screeded (Figure 92-C), and finished (Figure 92-D). It should be noted that the second truck ran out of concrete while constructing the last slab. The remnants of what was struck off from previous slabs were collected to complete the final slab. As a result, the last slab was only used as a trial. Once the concrete had been set, slabs were covered with wet burlap and plastic to provide additional moisture and prevent moisture loss (Figure 92-E).



(a) Pouring

(b) Consolidating

(c) Screeding



(d) Finishing



(e) Covering

Figure 92. Photo. Concrete casting.

Concrete Characterization

The cylindrical specimens were tested for compressive strength and modulus of elasticity. The specimen ages and curing conditions are summarized in Table 26.

Table 26. Specimen Ages and Curing Conditions of Concrete Characterization Tests

Test	Curing Condition	Specimen Age (days)	Specification
Compressive Strength	Lab, Field	7, 14, 28	AASHTO T22
Modulus of Elasticity	Field	30	ASTM C469

Compressive Strength

A cylindrical specimen was placed between two rubber cap ends and tested following AASHTO T22. The peak load was recorded, and the compressive strength (σ_c) was calculated below (Figure 93):

$$\sigma_c = \frac{P}{\pi r^2}$$

Figure 93. Equation. Compressive strength.

Where, σ_c is the compressive strength (psi), P is peak load (lb), and r is the radius of the cylinder (in).

Figure 94 presents the compressive strength versus age for lab- and field-cured specimens. IDOT requires a minimum compressive strength of 3,500 psi (24.1 MPa) at 14-day for paving concrete. Both lab- and field-cured specimens met the specification.

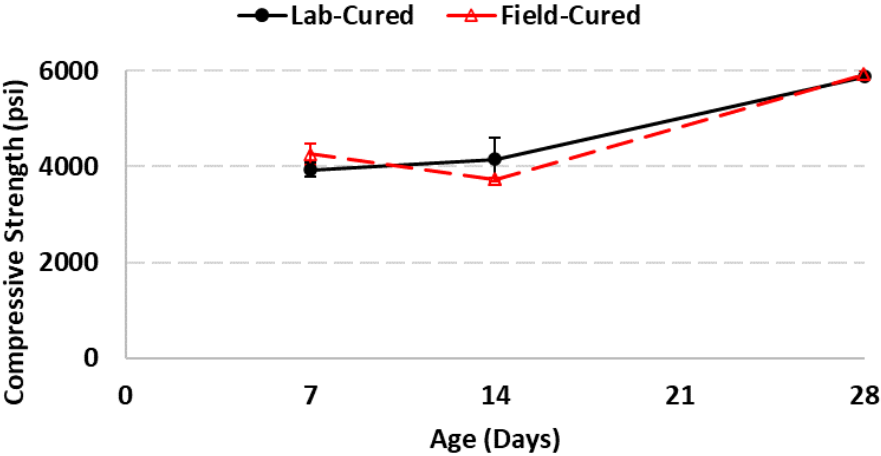


Figure 94. Chart. Compressive strength versus age for lab- and field-cured specimens.

Modulus of Elasticity

The modulus of elasticity was measured using a 6 × 12 in (150 × 305 mm) cylinder, which was placed between two rubber end caps. A longitudinal strain gauge was then instrumented, as presented in Figure 95.

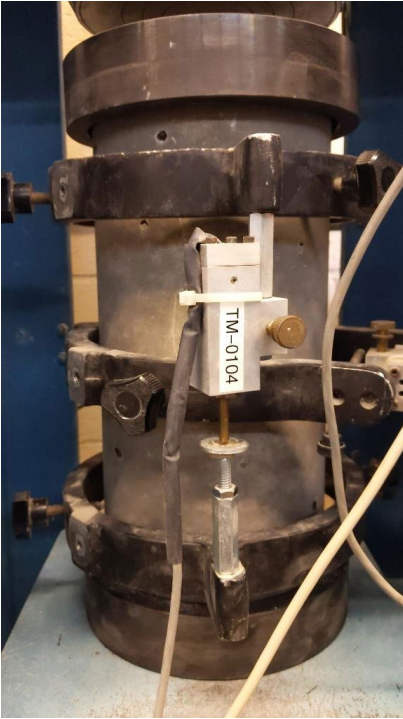


Figure 95. Photo. Test setup for the modulus of elasticity measurement.

From the longitudinal strain data, the modulus of elasticity (E) was calculated as below:

$$E = \frac{S_2 - S_1}{\varepsilon_2 - \varepsilon_1} = \frac{S_2 - S_1}{\varepsilon_2 - 0.000050}$$

Figure 96. Equation. Modulus of elasticity.

Where, E is the modulus of elasticity (psi); S_2 is the stress at approximately 40% of the compressive strength (psi); S_1 is the stress at longitudinal strain ε_1 (psi); ε_1 was selected as 0.00050 according to ASTM C46; and ε_2 is the longitudinal strain at stress S_2 .

The cylinder was pre-loaded once, followed by three loadings. The modulus of elasticity was obtained from the average results from the three loadings. The modulus of elasticity at 30 days was determined as 4.35E+06 psi (3.0E+04 MPa).

TACK-COAT APPLICATION

A tack coat is a light layer of diluted asphalt applied to HMA or PCC pavement surfaces to ensure good interface bonding between layers (Al-Qadi et al., 2012). A survey was conducted to determine the type to be used. According to responses collected by IDOT, SS-1h, SS-1hp, and NTEA are equally popular in Illinois. SS-1h was chosen for this project because it was locally available. The sampled tack coat had an asphalt binder residue percentage of 60.4%.

To ensure tack coat uniformity, a region-based application procedure was adopted. As presented in Figure 97, a 6 × 6 ft (1.8 × 1.8 m) slab surface was divided into 11 regions. No tack coat was applied in regions A and B, as the asphalt overlay will be cut and removed after compaction. The application rates presented in Figure 98 were determined following Article 406.05(c) of the 2016 IDOT Standard Specifications. To accelerate debonding between PCC and binder course in the potential crack zone, a reduced application rate of 0.025 lb/ft² (0.122 kg/m²) was used. In addition, the tack coat was heated to 100°F (38°C) before application to increase the workability.

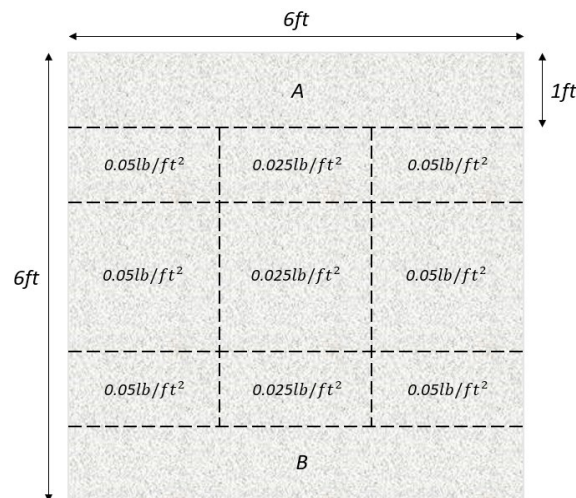
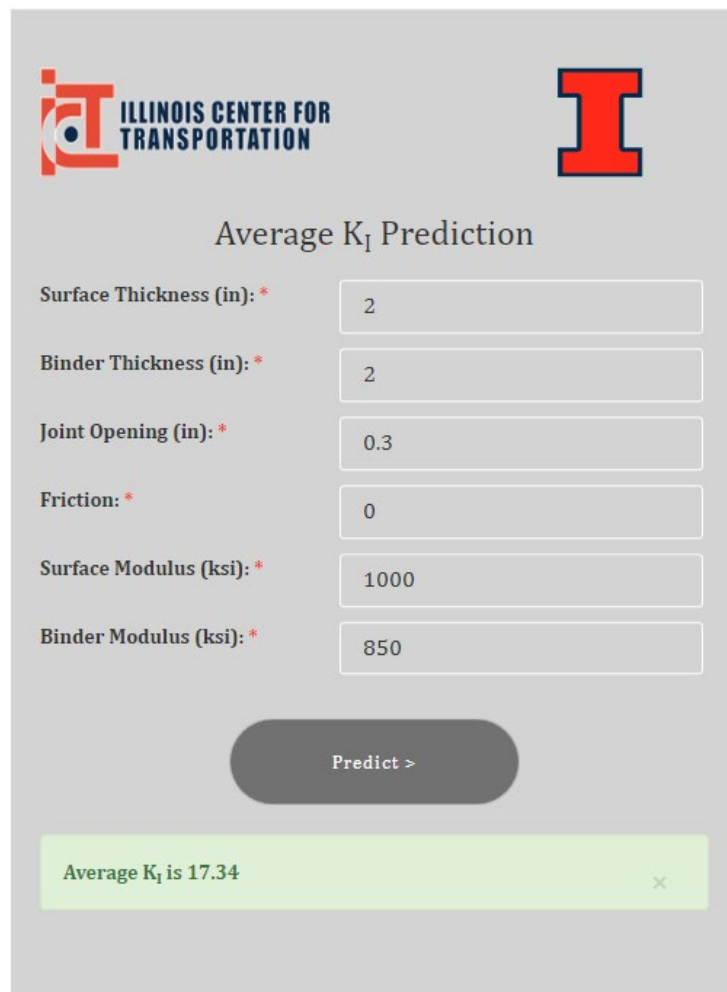


Figure 97. Diagram. Tack coat application rate.

APPENDIX B: PREDICTION TOOL FOR OVERLAY CRACKING POTENTIAL

The link to the tool that predicts overlay cracking potential can be found at <https://sif-prediction-api.herokuapp.com/>. Figure 98 presents the tool’s user interface. In Chapter 4, average K_I was identified as an appropriate fracture parameter for predicting reflective cracking potential of a system. Surface and binder course thickness and material property along with joint opening and friction is required as an input to predict average K_I of the system. The tool comes with default values, and the “Predict” button can be clicked to obtain the result (average K_I).



The screenshot shows the user interface for the Average K_I Prediction tool. At the top left is the logo for the Illinois Center for Transportation, and at the top right is a large red letter 'I'. The title 'Average K_I Prediction' is centered. Below the title are six input fields, each with a label and a value: Surface Thickness (in): * 2, Binder Thickness (in): * 2, Joint Opening (in): * 0.3, Friction: * 0, Surface Modulus (ksi): * 1000, and Binder Modulus (ksi): * 850. A 'Predict >' button is located below the input fields. At the bottom, a green box displays the result: 'Average K_I is 17.34' with a close button (x).

Figure 98. Image. User interface of the tool.

Table 27 presents the suggested range for each input. When the cursor hovers over the input boxes, the tool will show the corresponding suggested range for those inputs. Users should exercise caution when using values outside the suggested range. Extrapolation of the surrogate model can cause erroneous results.

Table 27. Suggested Range for Inputs in the Tool

Input	Default range
Surface Thickness (in)	1.5–2.5
Binder Thickness (in)	0.75–2.25
Joint opening (in)	0.3–0.8
Friction	0 for full slip or 100 for fully bonded (No intermediate values are allowed)
Surface modulus (ksi)	500–1100 (Modulus value at 70°F and 8Hz loading frequency)
Binder modulus (ksi)	500–1100 (Modulus value at 70°F and 8Hz loading frequency)



I ILLINOIS